Title
Tracking Fluorescent Liposomes and Fluorescent siRNA Contents During Internalization and Trafficking in Cultured Cells

Author
Tiffany, Matthew

Publication Date
2013

Peer reviewed|Thesis/dissertation

Tracking Fluorescent Liposomes and Fluorescent siRNA Contents During Internalization and Trafficking in Cultured Cells

by

Matthew R. Tiffany

DISSERTATION

Submitted in partial satisfaction of the requirements for the degree of

DOCTOR OF PHILOSOPHY

in

Pharmaceutical Science and Pharmacogenomics

in the

GRADUATE DIVISION

of the

UNIVERSITY OF CALIFORNIA, SAN FRANCISCO

Acknowledgments

I would like to first thank my mentor, Dr. Frank Szoka, for his guidance and support during my graduate education. He has always let me follow my own scientific path and rarely ever interfered in a non-constructive way. His relentless optimism, often bordering on insanity, is inspirational, and I hope that through all the difficulties I have professionally I can emulate this aspect of his.

I would like to thank my funding sources: The Cystic Fibrosis Foundation and NIH. It is extremely important to recognize that I was a lucky graduate student to get funded for the entirety of my graduate career.

I would like to thank all the other mentors I have come across during graduate school. Especially Dr. Alan Verkman, and Dr. Mark Von Zastrow for serving on my dissertation committee. I would also like to thank Dr. Michael McManus, Dr. Raul Andino, Dr. Andrej Sali, and Dr. Robert Stroud for serving on my qualifying exam committee.

I would also like to thank all Szoka lab members that I have overlapped with for their help and camaraderie. Especially, Dr. Rich Cohen, Dr. Saul Kivimae, Aditya Kohli, Jonathan Sockolosky, Dr. Derek van der Poll, Dr. Vince Venditto, Dr. Colin Walsh, and Dr. Doug Watson, who have all been integral in shaping the way I do science.

I also need to thank all the people who aren't in the Szoka lab who have helped me during graduate school. Dr. Pete Haggie was extremely helpful with ratiometric pH measurements and I wouldn't have been able to do it without his instruction. Dr. Nico Sturrman wrote the code I used for Gaussian fitting, and I am extremely thankful for giving me his source code. Lastly, I would also like to thank all the people at the Nikon Imaging Center: Dr. Kurt Thorn, Dr. DeLaine Larsen, and Alice Thwin, who have all been extremely helpful with maintaining the microscopes and fixing hardware issues. Without the Nikon Imaging Center Chapters 2 and 3 would not exist.

A huge thank you has to be said to my family, especially my mother, Grace, for always encouraging me to follow my own path, and my cousin, Elizabeth, for giving me my first opportunity to work in a lab. I would also like to thank all my aunts and uncles who have been supportive of my long graduate education. Lastly, I would like to thank the other half of my family, especially my wife, Vidita, for being the best human being I know, and supporting me unconditionally in everything I do. I would also like to thank my mother and father-in-law, Neeta and Nitin Chopra, for their support during graduate school.

Abstract

The large molecular weight, poly-anionic, and labile nature of small interfering RNA (siRNA) necessitate that these macromolecules are associated with carriers for cellular delivery. Lipid-based particles (LNPs) are very efficient at both cellular internalization and contents delivery; however, the cell has evolved mechanisms to efficiently degrade exogenous macromolecules and prevent the alteration of cellular function by foreign nucleic acids. An important aspect to understand is how cells differentially traffic LNPs so that more efficacious formulations can be designed for therapeutic purposes.

The majority of this dissertations presents a series of investigations into how cells endocytosis and sort LNPs encapsulating siRNA. First, I developed a set of fluorescently tagged endosomal marker proteins for clathrin-, caveolin-, and flotillin-dependent internalization pathways. In addition, I prepared markers for early and late endosomes (Rab5a and Rab7a), recycling endosomes (Rab11a), multivesicular bodies (CD82), and lysosomes (LAMP1). Second, I utilized the technique of ratiometric fluorescence microscopy to measure endosomal pH. Third, I developed an image-processing program built into ImageJ/Fiji to accurately colocalize the lipid, siRNA, and endosomal marker or pH probe signals. I then used these techniques to determine the pathway cells employ to internalize three different LNP formulations comprised of cholesteryl hemisuccinate (CHEMS), 1,2-dioleoyl-3-trimethylammonium-propane (DOTAP), and 1,2-dilinoleyloxy-3-dimethylaminopropane (DLinDMA).

I present evidence that DOTAP LNPs are more potent at delivering siRNA compared to CHEMS or DLinDMA LNPs. I also demonstrate that cells endocytose the LNPs in measurably different

ways, specifically, DOTAP exhibits at 0.62 pH unit increase in endosomal pH, pH dependent delivery, 30% colocalization with Rab11a and CD82 during the first 30 minutes of transfection, and a slow accumulation into LAMP1 positive lysosomes over a 4 hour transfection ending at 25% colocalization. In contrast, CHEMS is the least efficient LNP at delivering siRNA and colocalizes with LAMP1 at 25% during a 4 hour transfection. DLinDMA shows a 0.4 pH unit increase in endosomal pH and low colocalization (10 – 15%) with the Rab11a, CD82, and LAMP1 markers tested, despite being present at similar levels as the other formulations, and is presumably trafficked into compartments I did not label. Correlations between cellular trafficking and siRNA delivery efficiency are discussed that may aid in the design of potent LNP formulations.

Finally, I also investigated the human dsRNA transporter SIDT-1, and present evidence that high expression levels are required for cellular siRNA uptake, and the that extracellular domain does not bind directly to dsRNA. In the appendix, I present efforts to use site directed mutagenesis to convert human cytidine deaminase into an enzyme with cytosine deaminase activity.

Table of Contents

List of Tables

List of Figures

Abbreviations

Nucleic acids:
dsRNA - double stranded ribonucleic acid
siRNA - short interfering ribonucleic acid
DNA - deoxyribonucleic acid
ssDNA - single stranded deoxyribonucleic acid
cDNA - complementary deoxyribonucleic acid
pA - poly-adenosine
MCS - multiple cloning site

Proteins/Protein complexes:
CDS - coding sequence
RISC - RNA-induced silencing complex
EF1α - Human Elongation Factor 1α
UbC - Ubiquitin C
rtTA - reverse tetracycline transactivator
HDL - high density lipoprotein
LDL -low density lipoprotein
LDLR -low density lipoprotein receptor
IDOL - Inducible degrader of LDLR
EGF - epidermal growth factor
EGFR - epidermal growth factor receptor
HARE - hyaluronic acid receptor of endocytosis
CFTR - Cystic fibrosis transmembrane conductance regulator
ARF - ADP-ribosylation factor
Rab - Ras-related proteins in brain
MHC - major histocompatibility complex
NTD - N-terminal domain
His6 - hexahistidine
mKate - monomeric Katushka
GFP - green fluorescent protein
YFP - yellow fluorescent protein
CFP - cyan fluorescent protein
CltA - Clathrin light chain
Cav1 - caveolin-1
AP-2 - adaptor 2
Flot1 - flotillin-1
LAMP-1 - lysosome associated membrane protein 1
TAP - transporter associated with antigen processing
CD - cytosine deaminase
yCD - yeast cytosine deaminase
bCD - bacterial cytosine deaminase
CDA - cytidine deaminase
hCDA - human cytidine deaminase
hCD - human cytosine deaminase

Lipids/Polymers:
GPI - Glycosylphosphatidylinositol
PE - Phosphatidylethanolamine
PC - Phosphatidylcholine
DiD - 1,1′-dioctadecyl-3,3,3′,3′-tetramethylindodicarbocyanine perchlorate
DiO - 3,3'-dilinoleyloxacarbocyanine perchlorate
DOPE - 1,2-dioleoyl-sn-glycero-3-phosphoethanolamine
DOPC - 1,2-dioleoyl-sn-glycero-3-phosphocholine
DPPC - 1,2-dipalmitoyl-sn-glycero-3-phosphocholine
DOTAP - 1,2-dioleoyl-3-trimethylammonium-propane
TMAG - didodecyl N-(R-(trimethylammonio)acetyl)-D-glutamate chloride
DLPC - 1,2-dilauroyl-sn-glycero-3-phosphocholine
DOTMA - N-[1-(2,3- dioleyloxy)propyl]-N,N,N-trimethylammonium chloride
DC-Chol - 3ß-[N-(N',N'-dimethylaminoethane)-carbamoyl]cholesterol
SAINT-2 - N-methyl-4-(dioleyl)methylpyridinium
DMRIE-C - 1,2- dimyristyloxy-propyl-3-dimethyl-hydroxy ethyl ammonium bromide and cholesterol
DLinDAP - 1,2-Dilinoleoyl-3- dimethylaminopropane
DLinDMA - 1,2-dilinoleyloxy-3- dimethylaminopropane
DLinKDMA - 2,2-Dilinoleyl-4- dimethylaminomethyl- [1,3]-dioxolane
DLinK-C2-DMA - 1,2-dilinoleyl-4-(2- dimethylaminoethyl)-[1,3]-dioxolane
PEG-DMG - 1,2-dimyristoyl-sn-glycerol-[methoxy(polyethylene glycol)-2000
PEG-DSPE - 1,2-distearoyl-sn-glycero-3-phosphoethanolamine-N-[amino(polyethylene glycol)-2000]
HyC-Chol - 3β[N-(2-hydroxyethylaminoethane)- carbamoyl]-cholestene
Chol - choesterol
CHEMS - cholesteryl hemisuccinate
PEG - polyethyleneglycol
PAMAM - Poly(amidoamine)
PEI - Polyethylenimine
R8 - octa-arginine
GAG - glycosaminoglycan
CS - chondroitin sulfate
HA - hyaluronic acid
HS - heparan sulfate

Cellular processes/compartments:
RNAi - ribonucleic acid interference
GEEC/CLIC - GPI-Enriched Endocytic Compartments and Clathrin-Independent Carriers
RES - reticuloendotheial system
ECM - extracellular matrix
ER - endoplasmic reticulum
MVB - multivesicular body
ERC - endosomal-recycling compartment

Units:
nts - nucleotides
bp - base pair
×g - times (×) gravity
g - gram
pmoles - picomoles
mg - miligram
µg - microgram
M - molar
mM - milimolar
µM - micromolar
nM - nanomolar
mm - milimeter
µm - micrometer
nm - nanometer
L - liter
mL - mililiter
µL - microliter
ms - milisecond
kDa - kiloDalton
rpm - revolutions per minute
MOI - multiplicity of infection
S.E.M. - standard error of the mean
PDI - polydispersity index
pfu - plaque forming units
K_d - dissociation constant
IC_{50} - inhibitory concentration for 50% inhibition
ED_{50} - effective dose for 50% effect
MWCO - molecular weight cutoff

Chemicals:
5-FC - 5-fluorocytosine
5-FU - 5-fluorouracil
DHP - 4-[R]- hydroxyl-3,4-dihydropyrimidine
EDTA - Ethylenediaminetetraacetic acid
HEPES - 4-(2-hydroxyethyl)-1-piperazineethanesulfonic acid
G418 - Geneticin
Tris - tris(hydroxymethyl)aminomethane
CCCP - carbonyl cyanide m-chlorophenyl hydrazone
IPTG - isopropylthio-β-galactoside
PES - polyethylene sulfate
FITC - fluorescein isothiocyanate
TEX615
cm - chloramphenicol
kan - kanamycin
MβCD - methyl-β-cyclodextran

ADP - adenosine diphosphate
GTP - guanine triphosphate
CTP - cytidine triphosphate
TTP - thymidine triphosphate
UMP - Uridine monophosphate
UDP - Uridine diphosphate

Viruses/Cells:
HTLV - Human T-Cell Leukemia Virus
VSV - vesicular stomatitis virus
RSV - respiratory syncytial virus
SV40 - Simian virus 40
TEV - tobacco etch virus
HIV - Human immunodeficiency virus
HCV - Hepatitis C virus
SFV - Semliki Forest virus
CHO - Chinese hamster ovary cells

Media:
D-PBS - phosphate buffered saline without calcium and magnesium
PBS - phosphate buffered saline
PBSgp - phosphate buffered saline with glucose and pyruvate
FBS - fetal bovine serum
TB - terrific broth
LB - Lauria broth
SOC - Super Optimal broth with catabolite repression
RPMI - Roswell Park Memorial Institute

Techniques:
FACS - Fluorescence-activated cell sorting
SAXS - Small-angle X-ray scattering
SDS-PAGE - sodium dodecyl sulfate polyacrylamide gel electrophoresis
PCR - polymerase chain reaction
SPT - single particle tracking

Other:
CGSC - Coli Genetic Stock Center
EMCCD - electron multiplying charge coupled device

Chapter 1 : Endocytosis of Macromolecule Drugs

1.1 General Endocytosis

1.1.1 Importance of Endocytosis for Macromolecule Drug Delivery

The majority of drugs have intracellular targets that must be accessed to yield a therapeutic effect. For small molecule drugs that exhibit favorable pharmacokinetics, access to an intracellular target is mediated by either diffusion or active transport through the plasma membrane.

However, macromolecules are excluded from cellular entry in a manner that cannot be overcome by concentration. For example, double stranded RNA (dsRNA) is a macromolecule that is not transported into human cells. While a dsRNA transporter exists (Feinberg and Hunter, 2003), there is no convincing evidence that it is present and used throughout the animal kingdom. Since dsRNA is highly negatively charged, it is unable to diffuse through the plasma membrane as well. The only path for dsRNA to enter the cell is via endocytosis. This route presents a whole new host of problems. The first problem is that endocytosis is the mechanism by which cells eat, and as such macromolecules are digested and broken down during endocytosis. In addition, this process cannot be overcome by increasing concentration with the hope of escaping degradation, because the cell has a direct link between internalization and degradation and will not internalize more that it can process. Secondly, because foreign material enters the cell via endocytosis, there are mechanisms to detect the presence of certain substances. Again, dsRNA is a good example as the cell has evolved receptors to recognize dsRNA and respond as if it were a viral infection.

An understanding of endocytosis is critical to designing vectors that both circumvent the barriers described above and allow the intracellular access of macromolecule drugs. There are several

different classes of vectors used for macromolecule drug delivery, but the focus of this thesis is on the use of liposomes to deliver siRNA. Liposomes are characterized by an aqueous core partitioned by a lipid bilayer; however, when cationic lipids are used to condense nucleic acids the formation of multi-lamellar lipoplex occurs (Figure 1.1).

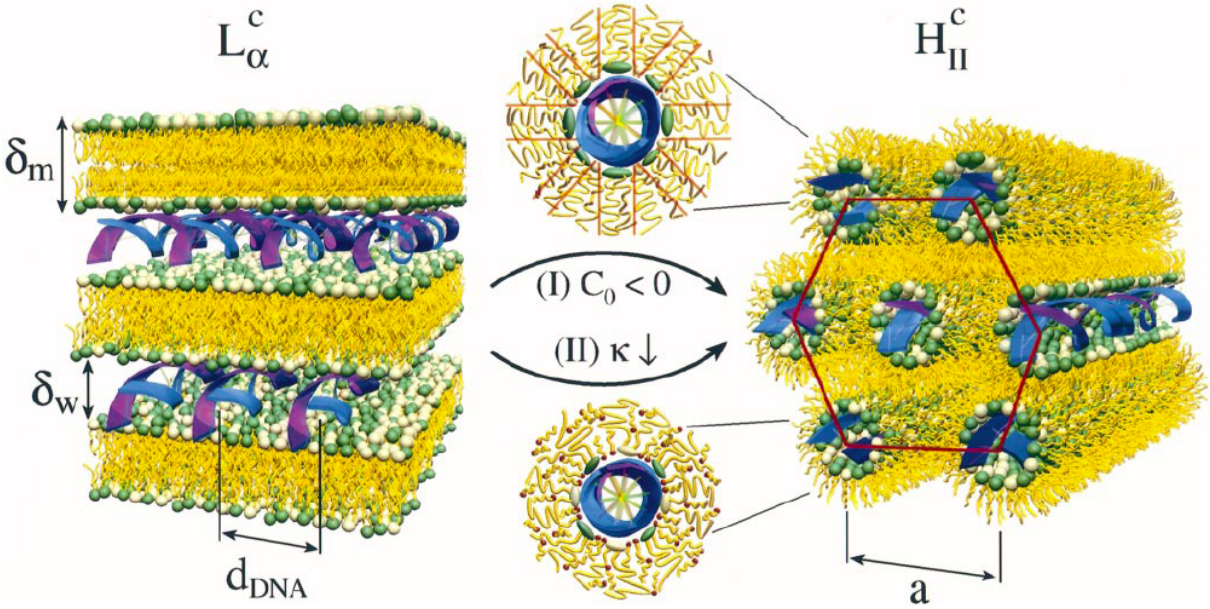

Figure 1.1 Schematic of lipoplex.
Lipoplex is comprised of lamellar sheets of lipid bilayers sandwiching nucleic acid (L_α). During delivery the presence of helper lipids such as DOPE causes a phase inversion to inverted hexagonal (H_{II}), which is a fusion competent phase that promotes cellular delivery of nucleic acids. Image copied from Koltover, 1998.

1.1.2 Historical Perspective of Endocytosis

Endocytosis is a complex cellular process (Doherty and McMahon, 2009; Kumari et al., 2010; Roth, 2006; Sandvig et al., 2011), which has been delineated because of three technological advances: the centrifuge, pharmacological inhibitors, and the microscope. The centrifuge allowed for cellular fractionation and separation of vesicles that could then be broken down into components and characterized further. Pharmacological inhibitors provided a method to perturb different aspects of membrane structure and endocytosis. Finally, the microscope (light, electron, and fluorescent) provided a window into the cell to observe the dynamic process of endocytosis.

Combined they have allowed investigators to identify components involved in endocytosis and how they interact to move macromolecules into and out of cells. Figure 1.2 shows the complex internalization pathways that have been identified to date that will be expounded upon in the following sections.

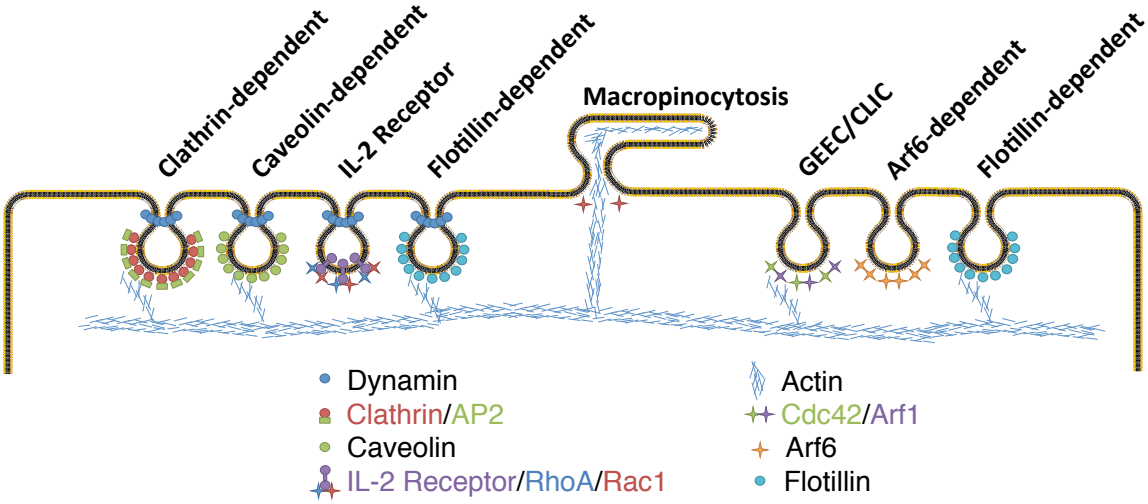

Figure 1.2 Cellular endocytosis pathways

The endocytosis pathways are separated by those that require dynamin-2 (left) and those that do not (right). Note that the Flotillin pathway has been shown to be both dynamin-2 dependent and independent. The pathways that are dependent upon actin are shown: Clathrin-, Caveolin-, Flotillin-, Macropinocytosis, and GPI-Enriched Endocytic Compartments/Clathrin-Independent Carriers (GEEC/CLIC). These pathways are the dominant cellular entry pathways in non-phagocytic cells.

1.1.2.1 Clathrin-mediated endocytosis

The first mechanistic characterization of cellular endocytosis was performed in the 1890s by Elie Metchnikoff who demonstrated that not only do cells internalize particles, but that during this process cells acidify the compartment. This pioneering study used litmus particles to observe a colormetric pH dependent change that is fundamentally still a corner stone of studying endocytosis today (Roth, 2006). The next major advance in cellular endocytosis came in 1964 with a set of time course experiments performed on oocytes in mosquitos by Roth and Porter (Roth and Porter, 1964). Mosquitos were fed to begin the process of yolk formation and fixed at

various time points for electron microscopy. They observed uniform 140 nm pit-like invaginations of the plasma membrane with 20 nm bristle coats on the cytoplasmic side. These were the first observations of what later became known as clathrin-coated pits in 1975 with the purification of clathrin from pig brain vesicles by Pearse (Pearse, 1975). Subsequently, clathrin-mediated endocytosis became the first well-studied and characterized mechanism of endocytosis. Low density lipoprotein (LDL) and epidermal growth factor (EGF) were the first proteins demonstrated to be internalized into clathrin-coated pits (Anderson et al., 1977; Gorden et al., 1978). Two years later vesicular stomatitis virus (VSV) was the first virus demonstrated to be taken up into clathrin-coated pits (Rothman et al., 1980). Finally, the cloning and sequencing of clathrin was done in 1987 (Kirchhausen et al., 1987).

However, it had long been recognized that clathrin was not a membrane bound protein and could readily be dissociated from membrane with high salt for example and reconstituted (Woodward and Roth, 1978). Moreover, other proteins were associated with the vesicle purifications and later shown to be involved in anchoring clathrin to the membrane (Unanue et al., 1981). The existence of accessory proteins for clathrin coats was demonstrated (Vigers et al., 1986), which began the process of coupling the coated pit to the concept of receptor mediated endocytosis that had been proposed years earlier (Goldstein et al., 1979). While the components of the coated pit were being identified, the exact mechanism by which the plasma membrane physically pinched off into a self-contained vesicle was not well understood. It was not until 1991 when dynamin was demonstrated to be involved in the maturation of membrane vesicles, coupling vesicle formation and force generation by the microtubule cytoskeleton (van der Bliek and Meyerowitz, 1991). These studies, among many others, were the keys to understanding the molecular biology of the initial step in endocytosis. However, concurrent with the identification of clathrin, other

clathrin-independent mechanisms of endocytosis were being studied, most notably caveolae.

1.1.2.2 Caveolin-mediated endocytosis

The first description of caveolae actually predates that of the coated pit by almost a decade (Palade, 1953; Yamada, 1955), however, the identification of caveolin-1 came almost 20 years after that of clathrin. The first characterization of the distinctively "flask-shaped" membrane invaginations are attributed to the separate works of Palade and Yamada in 1953 and 1955, respectively. Palade was among the first to describe the vesicles while studying capillaries and later proposed, correctly, their role in endocytosis (Palade, 1960). However, the name was introduced by Yamada, who at least began to distinguish a population of membrane invaginations to study that were separate and distinct from the coated-pit. Caveolae were first thought to be a coat free vesicle with many hypothesized functions. Because they were coat-free and only loosely being compartmentalized in nomenclature, the purification and ultimate characterization of caveolae developed slowly. The first important step was to recognize that caveolae indeed had a striated coat that was different from the lattice like clathrin coat (Izumi et al., 1988; 1989; Peters et al., 1985). The identification of what ultimately became named caveolin-1 and demonstration of a striated coat associated with caveolae arose from the use of an anti-phosphotyrosine antibody from an RSV transformed cell lysate (Glenney and Zokas, 1989). A mixture of proteins were isolated and used to make monoclonal antibodies, one of which was a 22-kDa protein that localized to puncta at the cellular membrane. However, Glenney really didn't know what he had and in a closer inspection of the protein, suggested that it was a regulatory subunit of a protein complex that mediated the effects of tyrosine phosphorylation during RSV infection (Glenney, 1989). By 1992, Glenney had teamed up with Anderson, who had been studying clathrin coated pits, and used the antibody against the 22-kDa protein to

demonstrate by electron microscopy that it localized to caveolae, and named it caveolin (Rothberg et al., 1992). Later that year caveolin was cloned and sequenced (Glenney and Soppet, 1992).

As with clathrin-coated pits, caveolae were demonstrated to be involved in the endocytosis of several molecules, including: GPI-anchored protein receptors for folate (Rothberg et al., 1990) and albumin (Yokota, 1982), glycolipid bound toxins (Montesano et al., 1982), cholesterol (Simionescu et al., 1983), and SV40 (Kartenbeck et al., 1989) are localized to caveolae/non-coated pits. After caveolin was identified, many of these molecules were reinvestigated and their association with caveolin-mediated endocytosis in now known to be more complex. For example, after SV40 enters the cell via caveolae, it localizes to a distinct non-acidic vesicle termed the caveosome before entering the endoplasmic reticulum bypassing the lysosome (Pelkmans et al., 2001).

The observation that caveolin-dependent endocytosis led to a non-acidic endocytosis route bypassing the lysosome, gained a significant amount of attention during the decade after its identification especially as a route for macromolecule drug delivery (Bareford and Swaan, 2007). However, the same group that proposed the caveosome has shown it to be an artifact of overexpression (Hayer et al., 2010). Adding further to the complexity of caveolae and endocytosis in general is the caveolin-1 null mouse model that was independently constructed in two labs (Drab et al., 2001; Razani et al., 2001; Schubert et al., 2001). The main defects found in these animals were in the vascular endothelia and albumin transport, but the mice were surprisingly normal otherwise. This led to the conclusion that other endocytosis mechanisms are able to compensate for the caveolar route. Indeed, GPI-anchored proteins, which were among the

first to be associated with caveolae/caveolin-1, are also taken up by a non-clathrin, non-caveolin, cdc42-regulated endocytosis pathway that was subsequently found to be flotillin dependent (Sabharanjak et al., 2002). It is now apparent that "non-coated" vesicles, of which caveolae were the first, represent one in a large array of distinct and specific endocytosis mechanisms available to the cell.

1.1.2.3 Clathrin- and caveolin-independent endocytosis

The first hint that other non-clathrin and non-caveolin endocytosis occurred came in studying cells lacking caveolin-1. In the absence of caveolin-1 many non-coated veiscular structures budding from the plasma membrane were observed (Drab et al., 2001). In addition, it was demonstrated that in the absence of caveolin-1, caveolae-like structures are internalized much more rapidly than in the presence of caveolin-1, suggesting that caveolin is actually involved in the stable maintenance of caveolar structures at the plasma membrane rather than their formation and internalization (Le et al., 2002). The identification of curved membrane domains made it apparent that other mechanisms, likely dependent upon other proteins, were present in the cell.

One of the first pathways was originally identified as colocalizing with the caveolin-rich, detergent resistant membrane fractions. Because the protein floated "like a flotilla of ships in the Triton-insoluble, buoyant fraction," it was named flotillin (Bickel et al., 1997). As a newcomer to a field that often demonstrates equivocal results, flotillin endocytosis has been shown to be both dynamin dependent (Aït-Slimane et al., 2009; Payne et al., 2007) and independent (Glebov et al., 2006). Along with the identification of flotillin-1, ADP-ribosylation factor (ARF) 6 was demonstrated to regulate a distinct recycling pathway for MHC class I proteins (Radhakrishna and Donaldson, 1997) and beta-integrins (Powelka et al., 2004). While currently a specialized

and limited method of endocytosis mainly characterized as a recycling pathway, Arf6 dependent internalization, and for that matter other GTPase regulated pathways will no doubt grow into their own distinct pathways. Two other endocytosis pathways that are the latest to arrive have been demonstrated to be dependent on the small GTPases RhoA (Lamaze et al., 2001) and Cdc42 (Sabharanjak et al., 2002). RhoA was originally demonstrated to be involved in the endocytosis of inerleukin-2 receptors (Lamaze et al., 2001) and has since been shown to be, at least in part, responsible for the endocytosis of botulism toxin C2 (Gibert et al., 2011). In addition, RhoA dependent uptake has been demonstrated to be constitutive and dynamin dependent (Khandelwal et al., 2010). As stated earlier Cdc42 was first demonstrated to be involved in the endocytosis of GPI-anchored proteins (Sabharanjak et al., 2002), but it has recently been demonstrated to be responsible for the largest fraction of cellular pinocytosis (Howes et al., 2010).

It is clear that as endocytosis continues to be investigated the distinct routes and their inevitable overlap will become more apparent. With the observation that the plasma membrane turns over approximately every hour by clathrin-mediated endocytosis alone, it is clear that ligands bound to their receptors will be taken up aberrantly by multiple pathways especially as receptor densities increase (Bretscher, 1982). Thus it is of no surprise that ligands that were originally defined as entering the cell via a specific route (e.g. GPI-anchored proteins) apparently are internalized via multiple pathways. Identifying a specific route for a given ligand is made more complex by the use of pharmacologic inhibitors of endocytosis that are nonspecific for a given pathway (Ivanov, 2007). For example, chlorpromazine is used as an inhibitor of clathrin, but it is also an inhibitor of phospholipase C, which regulates actin dynamics and macropinocytosis

(Amyere et al., 2000; Walenga et al., 1981). Another common method to demonstrate clathrin-dependent endocytosis is acidification of the cytoplasm, which has been shown to also induce global actin depolymerization and inhibit macropinocytosis (Cosson et al., 1989; Suzuki and Namiki, 2007). Methyl-β-cyclodextran is used to demonstrate cholesterol-dependent endocytosis, which is often associated with caveolae. However, MβCD also blocks endocytosis of transferrin via clathrin (Rodal et al., 1999). Amiloride is used as an inhibitor of macropinocytosis, but it also inhibits clathrin-dependent endocytosis (Ivanov et al., 2004; Meier et al., 2002). Although none of these commonly used inhibitors are specific, they are often used and accepted as proof of internalization via a specific pathway, which may be misleading.

1.1.3 Endocytosis Post-Internalization

Following the separation of an endosome from the plasma membrane via one of the pathways described above, there is a complex network of intracellular compartments with distinct protein and lipid compositions. This network is maintained by a diverse array of sorting proteins that act upon the nascent endosome to route it to its final destination (Olkkonen and Stenmark, 1997; Stenmark and Olkkonen, 2001; Stenmark, 2009). These events are outlined in a highly simplified manner in Figure 1.3. The intracellular trafficking pathways are regulated by a superfamily of Rab GTPases ('Ras-related in brain'), which control cargo selection, vesicle budding, motility and fusion (Gorvel et al., 1991; Salminen and Novick, 1987). This family of proteins differs most in their carboxyl termini, which is also the region that confers their reversible membrane association and subcellular targeting (Chavrier et al., 1991; 1990). During the progression of an early endosome to a lysosome, Rab proteins undergo a well-characterized conversion process and consequently are frequently used as markers for specific subcellular compartments (Rink et al., 2005). In addition to this family of proteins, there are an increasing number of Rab regulators

and effectors involved in intracellular trafficking that are beyond the scope of this thesis.

In addition to the Rab proteins that are integral in defining specific endocytosis compartments, there is a reduction in pH that occurs from the external pH ~ 7.4 to the lowest pH ~ 4.5 in the lysosome (Figure 1.3) (Maxfield and Yamashiro, 1987). The drop in pH provides a mechanism for recycling and sorting based upon pH dependent binding. The low pH of the lysosome is also well suited for the hydrolysis reactions that take place within that compartment and provides a mechanism for controlling such reactions from aberrantly hydrolyzing necessary cellular components. Many of the degradative enzymes inside the lysosome are acid-activated, and will not work at cytosolic pH. The lumenal pH is maintained and lowered by the vacuolar H^+-ATPase (V-ATPase) pumps (Forgac, 2007). In addition, several other proteins are responsible for lumenal pH such as the Na^+-K^+-ATPases that act primarily in the early endosome to limit the pH to ~ 6.5 by increasing the net positive charge inside the endosome (Huynh and Grinstein, 2007). The CLC family of Cl^- channels and Cl^-/H^+ exchangers are also involved in the regulation of pH inside endosomes (Jentsch, 2008). Working in concert, these proteins maintain the pH of distinct endosomal compartments that provides a cellular cue for endogenous functions as well as for non-viral and viral vectors, which will be discussed in more detail in the coming sections.

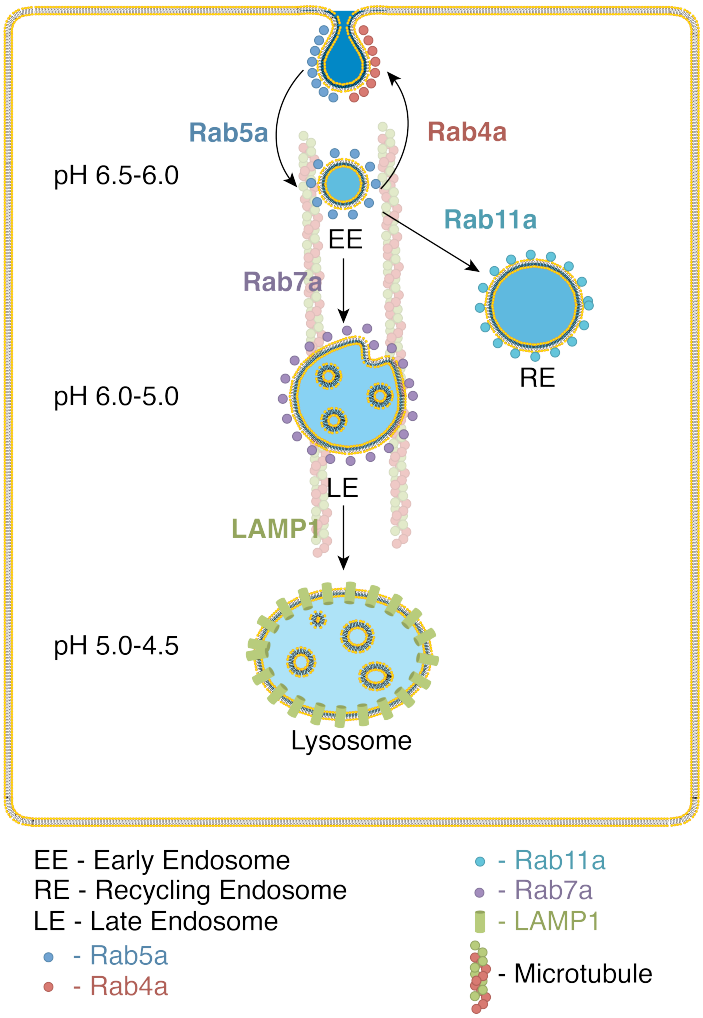

Figure 1.3 Endosome Maturation
Post-internalization, endosomes progress from an early endosome characterized by a pH between 6.5 and 6.0 with several protein markers such as Rab5a. Gradually, the protein markers are exchanged, defining different compartments and acidification continues until a final pH of 5.0 to 4.5 at the lysosome.

1.2 Viral endocytosis

While many protein and small molecules have been demonstrated to be endocytosed into the cell by specific mechanisms, the entry of viruses into cells is most informative for the understanding of macromolecular drug delivery. Viruses have co-evolved with their hosts and are able to not only gain entry into the cell, but also to cross the membrane barriers necessary for transmission of genetic material into the host cell. Viruses take advantage of a multitude of cellular cues and dynamics to allow for the most advantageous route of delivery. The sophisticated mechanism

used during viral entry only underscores the poor renditions humans have attempted to make for non-viral drug delivery systems.

Viral endocytosis, as with all other cargo, has had multiple revisions. With each new advance in methodology, new facets and complications to viral endocytosis have emerged. One of the most hotly debated topics is whether some viruses are able to gain cellular entry through the plasma membrane directly or if endocytosis is required (Marsh and Helenius, 2006). HIV is one such virus that was believed to infect the cell directly at the plasma membrane as the gp41 fusion peptide is pH-independent. However, single particle tracking was used to show that clathrin-mediated endocytosis is required for productive infection and the interaction of the virus with the plasma membrane did not proceed further than mixing of lipids (Miyauchi et al., 2009). It is likely that many other viruses that are believed to fuse directly with the plasma membrane will be demonstrate to require endocytosis.

There are clear benefits for viruses to enter cells by endocytosis. Acidification is one signal that many viruses take advantage of to exit endosomal compartments. However, the ability of viruses to fuse in response to low pH is often a multistep process. In many viruses, such as poliovirus, fusion proteins undergo conformational changes in response to acidic pH that expose hydrophobic regions allowing the virus to enter into the membrane and fuse (Madshus et al., 1984a; 1984b). In addition to conformational changes of fusion peptides/domains, acid-dependent proteolytic cleavage of viral proteins is often required prior to fusion as in the case of Ebola virus (Chandran et al., 2005). Not only do proteins mediate viral fusion, but lipids are also important for viral fusion. Dengue virus has been shown to undergo fusion only when exposed to

both low pH and anionic lipids (Zaitseva et al., 2010). Moreover the fusion-competent transition state achieved by exposure to low pH is maintained for ~30 minutes, awaiting interaction with anionic lipids, which is in contrast to influenza which is rapidly inactivated after exposure to low pH (Stegmann et al., 1986).

Another important aspect of viral endocytosis that is beginning to be appreciated is that viruses are sorted into distinct endosomal populations. As the complex interplay between the cell and virus is studied with finer resolution, new classes of endocytic vesicles are constantly being identified. One of the first indications of this came from the study of a Semliki Forest virus (SFV) mutant with a lower fusion pH threshold (Kielian et al., 1986). In this study wildtype SFV fused within 5 minutes of endocytosis, however, the mutant virus exhibited asynchronous fusion kinetics lasting from a few minutes to a few hours. The differences in fusion rates were proposed to arise from two different models. The first model proposed that differential sorting occurred from early endosomes into more mature vesicles that were either immediately competent for fusion or would themselves mature over time. The second model proposed that early endosomes were heterogenous in their acidification rates but that an individual endosome would eventually fuse or mature into a lysosome. It is likely that both models occur, however, the first model has since received support with the study of influenza virus. Influenza virus is sorted into a distinct early endosome compartment that does not undergo the classical maturation process, but rather rapidly transports to the perinuclear region where fusion occurs (Lakadamyali et al., 2006; 2003). The complexity of individual endosomal populations is further compounded by the observation that there are distinct domains within a single endosome (Sönnichsen et al., 2000). Rab4, Rab5, and Rab11 were shown by three color confocal and electron microscopy to localize to discrete

domains within the same recycling endosome. In addition, discrete lipid domains have been found in early endosomes (Sharma et al., 2003).

The study of viral biology has educated the field that endocytosis is a complex process that can provide guidance to the design of non-viral vectors for macromolecule drug delivery. Viruses are far more efficient at delivering genetic material precisely because they have evolved to fuse at precise environments and specific compartments. Unlike viruses, non-viral vectors are not as precise. While viral fusion and biological responses as a whole, are finely tuned to exhibit sharp transition states, many non-viral pH dependent liposomal vectors typically exhibit a broad pKa with small slope factors. Thus their transition between fusion incompetent and competent states is prolonged. However, newer classes of lipids are being developed that exhibit sharp transitions in pKa with large slope factors and at precisely defined optimal pKas of pH ~ 6.5 (Heyes et al., 2005; Jayaraman et al., 2012). These new lipids are beginning to mimic the monodispersity of viruses not only in shape and size but in response to cellular cues.

1.3 Liposomal endocytosis

1.3.1 The role of endocytosis

As with viral endocytosis, initial studies of liposomal uptake in cells indicated that direct fusion occurred at the plasma membrane (Weinstein et al., 1977). However, subsequent studies demonstrated that endocytosis was the predominant route of entry and that direct fusion occurred only under rare circumstances when the plasma membrane was compromised (Szoka et al., 1979; 1980; 1981). Moreover, endocytosis by clathrin-coated pits was implicated and contents release of certain molecules was mediated by acidification of vesicles as blockage of acidification

prevented release of carboxyfluorescein into the cytoplasm of cells (Straubinger et al., 1983). Subsequently it was directly demonstrated that liposomes encapsulating a pH responsive fluorophore experienced a pH drop inside cells (Chu et al., 1990; Straubinger et al., 1990). Moreover kinetic studies demonstrated that liposomes transited through endocytosis to the lysosome in approximately 30 minutes and that delivery and acidification were coupled (Yoshimura et al., 1995). These early studies were conducted on anionic liposome formulations, but it became apparent that cationic and pH responsive formulations were much more efficient at delivery of macromolecules especially plasmid DNA and antisense oligonucleotides (Felgner et al., 1987; Straubinger et al., 1985). Similar to how neutral and anionic formulations were studied, cationic and pH-responsive formulations that included PE were also demonstrated to be taken up via endocytosis (cationic: (Friend et al., 1996; Legendre and Szoka, 1992; Wrobel and Collins, 1995; Zhou and Huang, 1994); pH-responsive: (Chu et al., 1990; Legendre and Szoka, 1992)). These studies culminated in the proposal of a mechanism for liposome delivery whereby cell associated complexes are internalized via endocytosis (Zelphati and Szoka, 1996a). Subsequent electrostatic interactions between cationic vector lipids and anionic endosome lipids induce lipid mixing and fusion resulting in delivery of contents. Numerous studies have since supported this mechanism.

1.3.2 Cellular interactions

While it was quite clear by the mid-1990s that virtually all classes of liposomes entered the cell via endocytosis, limited research had been done to determine what the liposomes were binding to at the cell surface. There were conflicting reports of neutral phosphatidylcholine (PC) liposomes interacting with different cultured cells in trypsin-sensitive and -insensitive manners (Blumenthal et al., 1977; Pagano and Takeichi, 1977). For the case of trypsin-sensitive interactions with CHO

cells, a specific protein of ~60 kDa was implicated in the cellular binding (Pagano and Takeichi, 1977). Another early study investigating neutral PC liposomes found that opsonization of the liposomes by ApoE resulted in increased cellular uptake by hepatocytes (Bisgaier et al., 1989). Anionic formulations were demonstrated to interact with several scavenger receptors in macrophages as liposome binding was inhibited by acetly-LDL, oxidized LDL, dextran sulfate and fucoidan (Nishikawa et al., 1990). However, this result was rapidly called into question by another study that found the opposite (Lee et al., 1992a; 1992b). A later study that modeled and experimentally tested the diffusion kinetics of liposomes on cell surfaces suggested that anionic liposomes interacted non-specifically with cells, in contrast to the specific receptor-mediated interactions of adenovirus (Zhu et al., 2006). The binding of liposomes to cells was complicated by the fact that serum could alter the binding and uptake of certain formualtions. For example, anionic liposomes opsonized with antibody bound to a greater extent to macrophages than liposomes that were not opsonized, indicating that the Fc receptor could play a role in cellular binding either in the presence of serum or *in vivo* (Daleke et al., 1990). In contrast, it was demonstrated that neutral liposomes were opsonized by complement, implicating complement receptors in cellular binding, and that incorporation of anionic lipids inhibited complement opsonization of liposomes (Roerdink et al., 1983). Consistent with these data, it was found that ApoE was involved in clearance of neutral liposomes from circulation *in vivo*, as apoE deficient mice displayed a 4-fold slower clearance rate than wildtype mice (Yan et al., 2005). The same effect was not seen with anionic liposomes. The involvement of ApoE in the heptaocellular uptake of novel ionizable lipids has also been demonstrated and taken advantage of for siRNA delivery (Akinc et al., 2010). While in this study ApoE has been advantageous, for a long time such opsonins were viewed as detrimental and the basis for liposome clearance *in vivo* by the

reticuloendotheial system (RES). Consequently, development of polyethyleneglycol-lipid (PEG-lipid) conjugates to increase circulation time of liposomes were developed (Klibanov et al., 1990; Papahadjopoulos et al., 1991).

Once cationic lipids and lipoplex gained importance, the study of how they interacted with cells followed (Felgner et al., 1987). The proteoglycan syndecan-1, and glycosaminoglycans (GAGs), especially heparan sulfate, were demonstrated to be involved in cationic liposome-DNA (lipoplex) interactions with cells and protection against cytotoxic effects of lipoplex (Belting and Petersson, 1999a; Mislick and Baldeschwieler, 1996; Mounkes et al., 1998). Moreover, exogenous addition of GAGs to lipoplex disrupted the cationic lipid-DNA interaction reducing transfection (Belting and Petersson, 1999b; Xu and Szoka, 1996; Zelphati and Szoka, 1996a). As GAGs have a high anionic charge density, the interaction of lipoplex at the cell surface is largely a result of non-specific electrostatic interactions. However, another study found that lipoplex composed of TMAG:DLPC:DOPE did not interact with a macrophage cell line via GAGs, rather, through an unidentified protein component sensitive to trypsin treatment (Arima et al., 1997). A study on the kinetics of cationic liposomes composed of Soybean lecithin, Lauropal and DOTAP, uncovered a two-step binding process both of which were mediated by electrostatics. The first binding event was reversible and occurred within the glycocalyx and ECM, while the second was irreversible and occurred at the cellular membrane (Chenevier et al., 2000).

A comprehensive study on the transfection of several lipoplex formulations in the presence of exogenous GAGs, found that heparan sulfate (HS) and chondroitin sulfates (CS) were potent inhibitors of lipoplex internalization (Ruponen et al., 1999). Moreover, the different types of

lipoplex studied could be categorized by their susceptibility to the different GAGs tested: hyaluronic acid (HA), chondroitin sulfate B, chondroitin sulfate C, and heparan sulfate (HS). The polycation buffering lipid DOGS was sensitive to all GAGs, followed by DOTAP and DOTAP:Chol lipoplex that were not inhibited by hyaluronic acid, and lastly DOTAP:DOPE and DOTMA:DOPE lipoplex that were largely resistant to all GAGs tested. The same group later added a layer of complexity to the GAG mediated cellular association model of lipoplex using CHO cells lines deficient in HA, CS, and/or HS (Ruponen et al., 2004). They found that in mutants lacking all GAGs, transfection was increased compared to wildtype, however, a mutant lacking only HS had decreased transfection for both DOTAP and DOTAP:DOPE lipoplexes. The results could not be explained by reduced uptake, but rather that in the absence of GAGs, especially HS, other receptors substitute for GAG-mediated uptake and lead to a more efficient route of endocytosis. These data were consistent with their previous results demonstrating that addition of exogenous GAGs altered the intracellular distribution of lipoplexes (Ruponen et al., 2001). While nonspecific, electrostatic-driven liposome-GAG interactions were demonstrated to be important, it was clear that an underlying specific endocytosis mechanism was present. Lipoplex bound to the surface of cells clustered prior to internalization suggesting a specific receptor clustering mechanism of internalization (Rejman et al., 2004b).

1.3.3 Specific pathways of endocytosis

Since the early studies of liposome endocytosis, the number of synthetic lipids and targeting agents has increased dramatically. However, unlike viral and non-viral polymer systems, the study of liposome endocytosis stagnated. The initial studies only investigated whether liposomes were internalized or not, the involvement of metabolic activity, and the function of the microtubule work or actin cytoskeleton. By the late 1990s, when various route of endocytosis

had been accepted and methods to study them were established, the use of endocytosis inhibitors to study liposome endocytosis started being reported (Table 1.1). One of the first studies investigated the delivery of oligonucleotides with the cationic lipid DOTAP (Zelphati and Szoka, 1996b). In this study two broad inhibitors of endocytosis, cytochalasin B (actin polymerization inhibitor), and N-ethylmaleimide (vesicular fusion inhibitor), demonstrated conclusively for the first time that endocytosis and subsequent vesicular transport were required for delivery of oligonucleotides and suggested that macropinocytosis was an important pathway for cellular uptake. With the use of selective inhibitors of clathrin (chlorpromazine) and caveolae (filipin III), it was demonstrated that clathrin-mediated endocytosis and not caveolae were required for internalization and transfection of SAINT-2:DOPE lipoplex (Zuhorn et al., 2002a). A confirming study found that a lipoplex formulated with DOTAP was endocytosed by clathrin-mediated endocytosis exclusively and that transfection required this pathway of endocytosis, as transfection was blocked with chlorpromazine and potassium depletion, but not filipin or genistein treatment (Rejman et al., 2005).

However, clathrin was not always found to be essential. One study found that inhibition of all endocytosis and inhibition of macropinocytosis did not inhibit transfection by DOTAP:DOPE lipoplex to the same amount, suggesting that while clathrin-mediated endocytosis was a major contributor, other pathways were competent for mediating transfection (Simões et al., 2000). It is important to note that the lipoplex in this study had been opsonized specifically with purified human serum albumin, which could contribute to differences in uptake pathways.

As novel cationic lipids were synthesized and studied, the broad generalization that lipoplex was

endocytosed and delivered exclusively via clathrin-mediated endocytosis began to break down. For example, one study investigated two different cationic lipids, Lipofectamine and DMRIE-C, and found that clathrin was important for uptake and transfection with Lipofectamine, but caveolae were important for uptake and transfection with DMRIE-C (Wong et al., 2007). This was also one of the first studies to confirm and extend the results using inhibitors with microscopic colocalization with endosomal markers. In the case of DMRIE-C, internalization to the "caveosome" was visualized, followed by trafficking to the late endosome or lysosome. The observed differences in cellular endocytosis pathways was hypothesized to be either the result of the difference in size (Lipofectamine complexes being larger) or composition (DMRIE-C contains cholesterol, which might target it to cholesterol rich caveolae). A recent study on uptake of DOTAP:DOPC and DC-Chol:DOPE lipoplex found relatively little dependence on clathrin and caveolae pathways, but that macropinocytosis (inhibited with wortmannin) was most important for DOTAP:DOPC transfection (Cardarelli et al., 2011). DC-Chol:DOPE mediated transfection was not dependent upon clathrin, caveolae, or macropinocytosis, however, cholesterol dependence was found using methyl-β-cyclodextran. It is important to note that methyl-β-cyclodextran is a strong disruptor of cellular function in general as it forms soluble complexes with cholesterol, sequestering it out of membranes, making this one of the least useful endocytosis inhibitors. Moreover, in this study methyl-β-cyclodextran treatment continued after addition of the DC-Chol:DOPE complexes likely disrupting the complexes themselves. However, in this study microscopic colocalization was used to demonstrate that the two types of complexes highly colocalized with a macropinocytosis marker (dextran) and not caveolin-1 or transferrin. Moreover, after 3 hours of transfection, DOTAP:DOPC highly colocalized with lysosensor where as DC-Chol:DOPE colocalized to a lesser degree.

Another study focusing on the intracellular sorting of the cationic cholesterol derivative HyC-Chol:DOPE lipoplex (HyC-Chol: 3β[N-(2-hydroxyethylaminoethane)- carbamoyl]-cholestene), found that when microtubule polymerization is altered with nocodazole or taxol, transfection is increased (Hasegawa et al., 2001). In the presence of the microtubule inhibitors, lipoplex did not colocalize with lysosomes after 4 hours of transfection, suggesting a mechanism for the increased transfection observed. The enhancement of transfection with other lipoplex formulations after microtubule disruption was confirmed by others as well (Lindberg et al., 2001; Wang and MacDonald, 2004). It is important to note that while the interactions of lipoplex with the cell are mediated by GAGs and proteoglycans, the two different types of molecules are endocytosed by different pathways. Proteoglycans are endocytosed via flotillin-dependent pathways, but GAGs are endocytosed by the HARE receptor that follows clathrin-mediated endocytosis (Hansen et al., 2005; Harris and Weigel, 2008; Payne et al., 2007). Thus it appears that multiple pathways of endocytosis are utilized for lipoplex internalization.

In contrast to the well-studied cationic lipoplex internalization, other formulations have received little attention. One study utilized a battery of inhibitors to dissect the uptake and internalization of the classic pH-sensitive formulation composed of CHEMS:DOPE (Huth et al., 2006). The group identified that clathrin and caveolae were both important in the two cell types studied, and that macropinocytosis was only important for one of the cell lines tested. These results were confirmed in another study, which demonstrated that CHEMS:DOPE liposomes were endocytosed by both clathrin-dependent and clathrin-independent mechanisms, and after vesicular acidification and fusion the vesicles were sorted to the ER in a microtubule driven pathway (Mustata et al., 2009). This is one of the few studies to not only investigate cellular uptake by specific pathways, but also subsequent intracellular sorting. Another recent study

investigating non-lipoplex formulations analyzed DOPC and DOPC:Chol liposome internalization and found that clathrin-mediated endocytosis was largely required (Un et al., 2012). Another group investigated endocytosis of DOXIL and demonstrated that caveolin was important for uptake, as a caveolin-1 knockout cell line internalized 40% of wildtype (Sahay et al., 2010).

Most recently, ionizable cationic lipids of the DLinDMA series were shown to be endocytosed via clathrin-dependent and macropinocytosis pathways (Lin et al., 2013). This is supported by another study using the latest generation DLin-MC3-DMA formulation that demonstrated an initial uptake dependent upon clathrin, which subsequently signaled thorough Rabankyrin-5 to induce macropinocytosis (Gilleron et al., 2013). In addition, the group also demonstrated that ~1 – 2 % of siRNA escaped from the endosome into the cytosol and from a specific compartment that is suggested by the sigmoidal rather than linear release kinetics observed (Gilleron et al., 2013). Lastly, investigations on internalization of a formulation based upon the lipidoid C12-200 demonstrated that endocytic recycling of this formulation resulted in ~70% recycling of lipid nanoparticles that signaled through Niemann-Pick type C1 protein (NPC1) (Sahay et al., 2013). These data suggested that inhibition of recycling would lead to increased uptake and delivery. However, not all regulators of endocytic recycling increased the IC_{50} of siRNA delivered using the C12-200 based formulation tested. Specifically, inhibition of Rab11a, Rab8a, and Rab27a by siRNA knockdown increased the IC_{50} ~ 2-fold, while inhibition of only Rab27b decreased the IC_{50} by ~ 3-fold (Sahay et al., 2013). Thus, the broad statement that siRNA delivery by lipid nanoparticles is decreased by endocytic recycling, suggested by the authors, is not entirely correct. The data suggest that inhibiton of recycling from the perinuclear region to the cell

periphery mediated by Rab27b is the recycling step that is most advantageous to increased siRNA delivery efficiency (Ostrowski et al., 2013).

Formulation	Pathway	Reference
DOTAP	Macropinocytosis Clathrin-dependent	(Zelphati and Szoka, 1996b) (Rejman et al., 2005)
SAINT-2:DOPE	Clathrin-dependent	(Zuhorn et al., 2002a)
DOTAP:DOPE	Clathrin-dependent, other	(Simões et al., 2000)
Lipofectamine	Clathrin-dependent	(Wong et al., 2007)
DMRIE-C	Caveolin-dependent	(Wong et al., 2007)
DOTAP:DOPC	Macropinocytosis	(Cardarelli et al., 2011)
DC-Chol:DOPE	Macropinocytosis	(Cardarelli et al., 2011)
DLinDAP:PEG-DMG:Chol:DSPC	Clathrin-dependent, Macropinocytosis	(Lin et al., 2013)
DLinDMA:PEG-DMG:Chol:DSPC	Clathrin-dependent, Macropinocytosis	(Lin et al., 2013)
DLinKDMA:PEG-DMG:Chol:DSPC	Clathrin-dependent, Macropinocytosis	(Lin et al., 2013)
DLinK-C2-DMA:PEG-DMG:Chol:DSPC	Clathrin-dependent, Macropinocytosis	(Lin et al., 2013)
DLin-MC3-DMA: PEG-DMG:Chol:DSPC	Clathrin-dependent, Macropinocytosis	(Gilleron et al. 2013)
CHEMS:DOPE	Clathrin-, Caveolin-dependent, and Macropinocytosis	(Huth et al., 2006) (Mustata et al., 2009)
DOPC	Clathrin-dependent	(Un et al., 2012)
DOPC:Chol	Clathrin-dependent	(Un et al., 2012)
DOXIL	Caveolin-dependent	(Sahay et al., 2010)
C12-200:PEG-DMG:Chol:DSPC	Macropinocytosis	(Sahay et al., 2013)

Table 1.1 Published studies of pathways used for endocytosis of liposomal formulations

1.3.4 Size as a factor for endocytosis

As briefly suggested earlier, liposome/lipoplex size is also an important factor that was demonstrated to alter cellular uptake, association, and transfection *in vitro* (Ross and Hui, 1999). However, it was also known that particle size altered intracellular distribution and processing (Granot et al., 1994; Tabas et al., 1991; Zuhorn et al., 2002b). The aspect of size was a difficult

parameter to investigate due to the heterogeneity of liposome and lipoplex preparations at the time, however, smaller cationic lipoplex accumulated in lysosomes faster than larger complexes and, by extension, escape from early endosomes yielded better transfection. It is important to note that complexation in the presence of serum was used to make the smaller lipoplex and therefore there were likely compositional differences in the formulation that could explain the differences in delivery efficiency. To circumvent some of the limitations of investigating liposome size and endocytosis pathways at the time, the same group used precisely sized latex beads to investigate the relationship (Rejman et al., 2004a). This study found that particles less than 200 nm were taken up by clathrin-coated pits with the aid of chlorpromazine, and in agreement with their earlier study, they found that smaller particles were endocytosed faster that larger particles. In contrast, cellular uptake of particles that were 500 nm was inhibited by caveolae inhibitors and colocalized with the caveolar marker lactosylceramide. These studies demonstrate that size is a determining factor for endocytosis and subsequent cellular sorting.

1.4 Conclusion

It is quite clear that endocytosis is a complex network of tightly controlled cellular compartments, and that many of the pathways are still being unraveled and revealed. With regard to LNP endocytosis, the published studies with lipoplex and liposomes demonstrate that cellular uptake is dependent upon virtually every parameter tested: size, formulation, and cell type. However, it also demonstrates the need to investigate the process more thoroughly. The studies done to date provide a patchwork of results with the only clear indication being that clathrin-dependent endocytosis is most important and utilized followed by macropinocytosis. However, the studies are not complete as there have been no investigations of newly identified pathways such as flotillin-dependent endocytosis. Moreover subsequent intracellular trafficking of liposomes is virtually unknown. Much of the work done to design LNPs comes from *in vitro* assessment of novel lipid biophysics, most importantly, analysis of pH dependent fusogenicity and either *in vitro* cell transfections or *in vivo* studies. These studies skip close examination of the endosomal compartments through which LNPs traffic, while providing extremely important end point results that demonstrate therapeutic efficacy. Techniques to study LNP endocytosis using either more specific inhibition (RNAi) or unbiased methods (microscopic colocalization) have been poorly utilized, while being extensively utilized to study polymer, and viral endocytosis.

1.5 References

Aït-Slimane, T., Galmes, R., Trugnan, G., and Maurice, M. (2009). Basolateral internalization of GPI-anchored proteins occurs via a clathrin-independent flotillin-dependent pathway in polarized hepatic cells. Mol Biol Cell *20*, 3792–3800.

Akinc, A., Querbes, W., De, S., Qin, J., Frank-Kamenetsky, M., Jayaprakash, K.N., Jayaraman, M., Rajeev, K.G., Cantley, W.L., Dorkin, J.R., et al. (2010). Targeted delivery of RNAi therapeutics with endogenous and exogenous ligand-based mechanisms. Mol Ther *18*, 1357–1364.

Amyere, M., Payrastre, B., Krause, U., Van Der Smissen, P., Veithen, A., and Courtoy, P.J. (2000). Constitutive macropinocytosis in oncogene-transformed fibroblasts depends on sequential permanent activation of phosphoinositide 3-kinase and phospholipase C. Mol Biol Cell *11*, 3453–3467.

Anderson, R.G., Brown, M.S., and Goldstein, J.L. (1977). Role of the coated endocytic vesicle in the uptake of receptor-bound low density lipoprotein in human fibroblasts. Cell *10*, 351–364.

Arima, H., Aramaki, Y., and Tsuchiya, S. (1997). Contribution of trypsin-sensitive proteins to binding of cationic liposomes to the mouse macrophage-like cell line RAW264.7. J Pharm Sci *86*, 786–790.

Bareford, L.M., and Swaan, P.W. (2007). Endocytic mechanisms for targeted drug delivery. Adv Drug Deliv Rev *59*, 748–758.

Belting, M., and Petersson, P. (1999a). Protective role for proteoglycans against cationic lipid cytotoxicity allowing optimal transfection efficiency in vitro. Biochem J *342 (Pt 2)*, 281–286.

Belting, M., and Petersson, P. (1999b). Intracellular accumulation of secreted proteoglycans inhibits cationic lipid-mediated gene transfer. Co-transfer of glycosaminoglycans to the nucleus. J Biol Chem *274*, 19375–19382.

Bickel, P.E., Scherer, P.E., Schnitzer, J.E., Oh, P., Lisanti, M.P., and Lodish, H.F. (1997). Flotillin and epidermal surface antigen define a new family of caveolae-associated integral membrane proteins. J Biol Chem *272*, 13793–13802.

Bisgaier, C.L., Siebenkas, M.V., and Williams, K.J. (1989). Effects of apolipoproteins A-IV and A-I on the uptake of phospholipid liposomes by hepatocytes. J Biol Chem *264*, 862–866.

Blumenthal, R., Weinstein, J.N., Sharrow, S.O., and Henkart, P. (1977). Liposome--lymphocyte interaction: saturable sites for transfer and intracellular release of liposome contents. Proc Natl Acad Sci U S A *74*, 5603–5607.

Bretscher, M.S. (1982). Surface uptake by fibroblasts and its consequences. Cold Spring Harb Symp Quant Biol *46 Pt 2*, 707–712.

Cardarelli, F., Pozzi, D., Bifone, A., Marchini, C., and Caracciolo, G. (2011). Cholesterol-

dependent macropinocytosis and endosomal escape control the transfection efficiency of lipoplexes in CHO Living Cells. Mol Pharm.

Chandran, K., Sullivan, N.J., Felbor, U., Whelan, S.P., and Cunningham, J.M. (2005). Endosomal proteolysis of the Ebola virus glycoprotein is necessary for infection. Science *308*, 1643–1645.

Chavrier, P., Gorvel, J.P., Stelzer, E., Simons, K., Gruenberg, J., and Zerial, M. (1991). Hypervariable C-terminal domain of rab proteins acts as a targeting signal. Nature *353*, 769–772.

Chavrier, P., Parton, R.G., Hauri, H.P., Simons, K., and Zerial, M. (1990). Localization of low molecular weight GTP binding proteins to exocytic and endocytic compartments. Cell *62*, 317–329.

Chenevier, P., Veyret, B., Roux, D., and Henry-Toulmé, N. (2000). Interaction of cationic colloids at the surface of J774 cells: a kinetic analysis. Biophys J *79*, 1298–1309.

Chu, C.J., Dijkstra, J., Lai, M.Z., Hong, K., and Szoka, F.C., Jr (1990). Efficiency of cytoplasmic delivery by pH-sensitive liposomes to cells in culture. Pharm Res *7*, 824–834.

Cosson, P., de Curtis, I., Pouysségur, J., Griffiths, G., and Davoust, J. (1989). Low cytoplasmic pH inhibits endocytosis and transport from the trans-Golgi network to the cell surface. J Cell Biol *108*, 377–387.

Daleke, D.L., Hong, K., and Papahadjopoulos, D. (1990). Endocytosis of liposomes by macrophages: binding, acidification and leakage of liposomes monitored by a new fluorescence assay. BBA - Biomembranes *1024*, 352–366.

Doherty, G.J., and McMahon, H.T. (2009). Mechanisms of endocytosis. Annu. Rev. Biochem. *78*, 857–902.

Drab, M., Verkade, P., Elger, M., Kasper, M., Lohn, M., Lauterbach, B., Menne, J., Lindschau, C., Mende, F., Luft, F.C., et al. (2001). Loss of caveolae, vascular dysfunction, and pulmonary defects in caveolin-1 gene-disrupted mice. Science *293*, 2449–2452.

Feinberg, E.H., and Hunter, C.P. (2003). Transport of dsRNA into cells by the transmembrane protein SID-1. Science *301*, 1545–1547.

Felgner, P.L., Gadek, T.R., Holm, M., Roman, R., Chan, H.W., Wenz, M., Northrop, J.P., Ringold, G.M., and Danielsen, M. (1987). Lipofection: a highly efficient, lipid-mediated DNA-transfection procedure. Proc Natl Acad Sci USA *84*, 7413–7417.

Forgac, M.M. (2007). Vacuolar ATPases: rotary proton pumps in physiology and pathophysiology. Nat Rev Mol Cell Biol *8*, 917–929.

Friend, D.S., Papahadjopoulos, D., and Debs, R.J. (1996). Endocytosis and intracellular processing accompanying transfection mediated by cationic liposomes. Biochim Biophys Acta *1278*, 41–50.

Gibert, M., Monier, M.-N., Ruez, R., Hale, M.L., Stiles, B.G., Benmerah, A., Johannes, L., Lamaze, C., and Popoff, M.R. (2011). Endocytosis and toxicity of clostridial binary toxins depend on a clathrin-independent pathway regulated by Rho-GDI. Cell. Microbiol. *13*, 154–170.

Gilleron, J., Querbes, W., Zeigerer, A., Borodovsky, A., Marsico, G., Schubert, U., Manygoats, K., Seifert, S., Andree, C., Stöter, M., et al. (2013). Image-based analysis of lipid nanoparticle-mediated siRNA delivery, intracellular trafficking and endosomal escape. Nat Biotechnol *31*, 638–646.

Glebov, O.O., Bright, N.A., and Nichols, B.J. (2006). Flotillin-1 defines a clathrin-independent endocytic pathway in mammalian cells. Nat Cell Biol *8*, 46–54.

Glenney, J.R. (1989). Tyrosine phosphorylation of a 22-kDa protein is correlated with transformation by Rous sarcoma virus. J Biol Chem *264*, 20163–20166.

Glenney, J.R., and Soppet, D. (1992). Sequence and expression of caveolin, a protein component of caveolae plasma membrane domains phosphorylated on tyrosine in Rous sarcoma virus-transformed fibroblasts. Proc Natl Acad Sci U S A *89*, 10517–10521.

Glenney, J.R., and Zokas, L. (1989). Novel tyrosine kinase substrates from Rous sarcoma virus-transformed cells are present in the membrane skeleton. J Cell Biol *108*, 2401–2408.

Goldstein, J.L., Anderson, R.G., and Brown, M.S. (1979). Coated pits, coated vesicles, and receptor-mediated endocytosis. Nature *279*, 679–685.

Gorden, P., Carpentier, J.L., Cohen, S., and Orci, L. (1978). Epidermal growth factor: morphological demonstration of binding, internalization, and lysosomal association in human fibroblasts. Proc Natl Acad Sci U S A *75*, 5025–5029.

Gorvel, J.P., Chavrier, P., Zerial, M., and Gruenberg, J. (1991). rab5 controls early endosome fusion in vitro. Cell *64*, 915–925.

Granot, E., Schwiegelshohn, B., Tabas, I., Gorecki, M., Vogel, T., Carpentier, Y.A., and Deckelbaum, R.J. (1994). Effects of particle size on cell uptake of model triglyceride-rich particles with and without apoprotein E. Biochemistry *33*, 15190–15197.

Hansen, B., Longati, P., Elvevold, K., Nedredal, G.-I., Schledzewski, K., Olsen, R., Falkowski, M., Kzhyshkowska, J., Carlsson, F., Johansson, S., et al. (2005). Stabilin-1 and stabilin-2 are both directed into the early endocytic pathway in hepatic sinusoidal endothelium via interactions with clathrin/AP-2, independent of ligand binding. Exp Cell Res *303*, 160–173.

Harris, E.N., and Weigel, P.H. (2008). The ligand-binding profile of HARE: hyaluronan and chondroitin sulfates A, C, and D bind to overlapping sites distinct from the sites for heparin, acetylated low-density lipoprotein, dermatan sulfate, and CS-E. Glycobiology *18*, 638–648.

Hasegawa, S., Hirashima, N., and Nakanishi, M. (2001). Microtubule involvement in the intracellular dynamics for gene transfection mediated by cationic liposomes. Gene Ther *8*, 1669–1673.

Hayer, A., Stoeber, M., Ritz, D., Engel, S., Meyer, H.H., and Helenius, A. (2010). Caveolin-1 is ubiquitinated and targeted to intralumenal vesicles in endolysosomes for degradation. J Cell Biol *191*, 615–629.

Heyes, J., Palmer, L.R., Bremner, K., and Maclachlan, I. (2005). Cationic lipid saturation influences intracellular delivery of encapsulated nucleic acids. Journal of Controlled Release *107*, 276–287.

Howes, M.T., Kirkham, M., Riches, J., Cortese, K., Walser, P.J., Simpson, F., Hill, M.M., Jones, A., Lundmark, R., Lindsay, M.R., et al. (2010). Clathrin-independent carriers form a high capacity endocytic sorting system at the leading edge of migrating cells. J Cell Biol *190*, 675–691.

Huth, U.S., Schubert, R., and Peschka-Süss, R. (2006). Investigating the uptake and intracellular fate of pH-sensitive liposomes by flow cytometry and spectral bio-imaging. Journal of Controlled Release *110*, 490–504.

Ivanov, A.I. (2007). Exocytosis and Endocytosis (Humana Press).

Ivanov, A.I., Nusrat, A., and Parkos, C.A. (2004). Endocytosis of epithelial apical junctional proteins by a clathrin-mediated pathway into a unique storage compartment. Mol Biol Cell *15*, 176–188.

Izumi, T., Shibata, Y., and Yamamoto, T. (1988). Striped structures on the cytoplasmic surface membranes of the endothelial vesicles of the rat aorta revealed by quick-freeze, deep-etching replicas. Anat. Rec. *220*, 225–232.

Izumi, T., Shibata, Y., and Yamamoto, T. (1989). The cytoplasmic surface structures of uncoated vesicles in various tissues of rat as revealed by quick-freeze, deep-etching replicas. J Electron Microsc (Tokyo) *38*, 47–53.

Jayaraman, M., Ansell, S.M., Mui, B.L., Tam, Y.K., Chen, J., Du, X., Butler, D., Eltepu, L., Matsuda, S., Narayanannair Jayaprakash, K., et al. (2012). Maximizing the potency of siRNA lipid nanoparticles for hepatic gene silencing in vivo. Angew. Chem. Int. Ed. *51*, 8529–8533.

Jentsch, T.J. (2008). CLC chloride channels and transporters: from genes to protein structure, pathology and physiology. Crit Rev Biochem Mol Biol *43*, 3–36.

Kartenbeck, J., Stukenbrok, H., and Helenius, A. (1989). Endocytosis of simian virus 40 into the endoplasmic reticulum. J Cell Biol *109*, 2721–2729.

Khandelwal, P., Ruiz, W.G., and Apodaca, G. (2010). Compensatory endocytosis in bladder umbrella cells occurs through an integrin-regulated and RhoA- and dynamin-dependent pathway. Embo J *29*, 1961–1975.

Kielian, M.C., Marsh, M., and Helenius, A. (1986). Kinetics of endosome acidification detected by mutant and wild-type Semliki Forest virus. Embo J *5*, 3103–3109.

Kirchhausen, T., Harrison, S.C., Chow, E.P., Mattaliano, R.J., Ramachandran, K.L., Smart, J., and Brosius, J. (1987). Clathrin heavy chain: molecular cloning and complete primary structure. Proc Natl Acad Sci U S A *84*, 8805–8809.

Klibanov, A.L., Maruyama, K., Torchilin, V.P., and Huang, L. (1990). Amphipathic polyethyleneglycols effectively prolong the circulation time of liposomes. FEBS Lett *268*, 235–237.

Koltover, I., Salditt, T., Rädler, J.O., and Safinya, C.R. (1998). An inverted hexagonal phase of cationic liposome-DNA complexes related to DNA release and delivery. Science *281*, 78–81.

Kumari, S., Mg, S., and Mayor, S. (2010). Endocytosis unplugged: multiple ways to enter the cell. Cell Res *20*, 256–275.

Lakadamyali, M., Rust, M.J., and Zhuang, X. (2006). Ligands for clathrin-mediated endocytosis are differentially sorted into distinct populations of early endosomes. Cell *124*, 997–1009.

Lakadamyali, M., Rust, M.J., Babcock, H.P., and Zhuang, X. (2003). Visualizing infection of individual influenza viruses. Proc Natl Acad Sci U S A *100*, 9280–9285.

Lamaze, C., Dujeancourt, A., Baba, T., Lo, C.G., Benmerah, A., and Dautry-Varsat, A. (2001). Interleukin 2 receptors and detergent-resistant membrane domains define a clathrin-independent endocytic pathway. Mol Cell *7*, 661–671.

Le, P.U., Guay, G., Altschuler, Y., and Nabi, I.R. (2002). Caveolin-1 is a negative regulator of caveolae-mediated endocytosis to the endoplasmic reticulum. J Biol Chem *277*, 3371–3379.

Lee, K.D., Hong, K., and Papahadjopoulos, D. (1992a). Recognition of liposomes by cells: in vitro binding and endocytosis mediated by specific lipid headgroups and surface charge density. Biochim Biophys Acta *1103*, 185–197.

Lee, K.D., Pitas, R.E., and Papahadjopoulos, D. (1992b). Evidence that the scavenger receptor is not involved in the uptake of negatively charged liposomes by cells. Biochim Biophys Acta *1111*, 1–6.

Legendre, J.Y., and Szoka, F.C., Jr (1992). Delivery of plasmid DNA into mammalian cell lines using pH-sensitive liposomes: comparison with cationic liposomes. Pharm Res *9*, 1235–1242.

Lin, P.J.C., Tam, Y.Y.C., Hafez, I., Sandhu, A., Chen, S., Ciufolini, M.A., Nabi, I.R., and Cullis, P.R. (2013). Influence of cationic lipid composition on uptake and intracellular processing of lipid nanoparticle formulations of siRNA. Nanomedicine: Nanotechnology, Biology and Medicine *9*, 233–246.

Lindberg, J., Fernandez, M.A., Ropp, J.D., and Hamm-Alvarez, S.F. (2001). Nocodazole treatment of CV-1 cells enhances nuclear/perinuclear accumulation of lipid-DNA complexes and increases gene expression. Pharm Res *18*, 246–249.

Madshus, I.H., Olsnes, S., and Sandvig, K. (1984a). Mechanism of entry into the cytosol of

poliovirus type 1: requirement for low pH. J Cell Biol *98*, 1194–1200.

Madshus, I.H., Olsnes, S., and Sandvig, K. (1984b). Requirements for entry of poliovirus RNA into cells at low pH. Embo J *3*, 1945–1950.

Marsh, M., and Helenius, A. (2006). Virus entry: open sesame. Cell *124*, 729–740.

Maxfield, F.R., and Yamashiro, D.J. (1987). Endosome Acidification and the Pathways of Receptor-Mediated Endocytosis. In Immunobiology of Proteins and Peptides IV, (Boston, MA: Springer US), pp. 189–198.

Meier, O., Boucke, K., Hammer, S.V., Keller, S., Stidwill, R.P., Hemmi, S., and Greber, U.F. (2002). Adenovirus triggers macropinocytosis and endosomal leakage together with its clathrin-mediated uptake. J Cell Biol *158*, 1119–1131.

Mislick, K.A., and Baldeschwieler, J.D. (1996). Evidence for the role of proteoglycans in cation-mediated gene transfer. Proc Natl Acad Sci U S A *93*, 12349–12354.

Miyauchi, K., Kim, Y., Latinovic, O., Morozov, V., and Melikyan, G.B. (2009). HIV Enters Cells via Endocytosis and Dynamin-Dependent Fusion with Endosomes. Cell *137*, 433–444.

Montesano, R., Roth, J., Robert, A., and Orci, L. (1982). Non-coated membrane invaginations are involved in binding and internalization of cholera and tetanus toxins. Nature *296*, 651–653.

Mounkes, L.C., Zhong, W., Cipres-Palacin, G., Heath, T.D., and Debs, R.J. (1998). Proteoglycans mediate cationic liposome-DNA complex-based gene delivery in vitro and in vivo. J Biol Chem *273*, 26164–26170.

Mustata, R.C., Grigorescu, A., and Petrescu, S.M. (2009). Encapsulated cargo internalized by fusogenic liposomes partially overlaps the endoplasmic reticulum. J Cell Mol Med *13*, 3110–3121.

Nishikawa, K., Arai, H., and Inoue, K. (1990). Scavenger receptor-mediated uptake and metabolism of lipid vesicles containing acidic phospholipids by mouse peritoneal macrophages. J Biol Chem *265*, 5226–5231.

Olkkonen, V.M., and Stenmark, H. (1997). Role of Rab GTPases in membrane traffic. Int. Rev. Cytol. *176*, 1–85.

Ostrowski, M., Carmo, N.B., Krumeich, S., Fanget, I., Raposo, G., Savina, A., Moita, C.F., Schauer, K., Hume, A.N., Freitas, R.P., et al. (2010). Rab27a and Rab27b control different steps of the exosome secretion pathway. Nat Cell Biol *12*, 19–30–suppp1–13.

Pagano, R.E., and Takeichi, M. (1977). Adhesion of phospholipid vesicles to Chinese hamster fibroblasts. Role of cell surface proteins. J Cell Biol *74*, 531–546.

Palade, G.E. (1953). Fine structure of blood capillaries. J Appl Phys.

Palade, G.E. (1960). Transport in quanta across the endothelium of blood capillaries. Anat. Rec. *136*, 254.

Papahadjopoulos, D., Allen, T.M., Gabizon, A., Mayhew, E., Matthay, K., Huang, S.K., Lee, K.D., Woodle, M.C., Lasic, D.D., and Redemann, C. (1991). Sterically stabilized liposomes: improvements in pharmacokinetics and antitumor therapeutic efficacy. Proc Natl Acad Sci U S A *88*, 11460–11464.

Payne, C.K., Jones, S.A., Chen, C., and Zhuang, X. (2007). Internalization and Trafficking of Cell Surface Proteoglycans and Proteoglycan-Binding Ligands. Traffic *8*, 389–401.

Pearse, B.M. (1975). Coated vesicles from pig brain: purification and biochemical characterization. J Mol Biol *97*, 93–98.

Pelkmans, L., Kartenbeck, J., and Helenius, A. (2001). Caveolar endocytosis of simian virus 40 reveals a new two-step vesicular-transport pathway to the ER. Nat Cell Biol *3*, 473–483.

Peters, K.R., Carley, W.W., and Palade, G.E. (1985). Endothelial plasmalemmal vesicles have a characteristic striped bipolar surface structure. J Cell Biol *101*, 2233–2238.

Powelka, A.M., Sun, J., Li, J., Gao, M., Shaw, L.M., Sonnenberg, A., and Hsu, V.W. (2004). Stimulation-dependent recycling of integrin beta1 regulated by ARF6 and Rab11. Traffic *5*, 20–36.

Radhakrishna, H., and Donaldson, J.G. (1997). ADP-ribosylation factor 6 regulates a novel plasma membrane recycling pathway. J Cell Biol *139*, 49–61.

Razani, B., Engelman, J.A., Wang, X.B., Schubert, W., Zhang, X.L., Marks, C.B., Macaluso, F., Russell, R.G., Li, M., Pestell, R.G., et al. (2001). Caveolin-1 null mice are viable but show evidence of hyperproliferative and vascular abnormalities. J Biol Chem *276*, 38121–38138.

Rejman, J.J., Bragonzi, A.A., and Conese, M.M. (2005). Role of clathrin- and caveolae-mediated endocytosis in gene transfer mediated by lipo- and polyplexes. Mol Ther *12*, 7–7.

Rejman, J., Oberle, V., Zuhorn, I.S., and Hoekstra, D. (2004a). Size-dependent internalization of particles via the pathways of clathrin- and caveolae-mediated endocytosis. Biochem J *377*, 159–169.

Rejman, J., Wagenaar, A., Engberts, J.B.F.N., and Hoekstra, D. (2004b). Characterization and transfection properties of lipoplexes stabilized with novel exchangeable polyethylene glycol-lipid conjugates. Biochim Biophys Acta *1660*, 41–52.

Rink, J., Ghigo, E., Kalaidzidis, Y., and Zerial, M. (2005). Rab Conversion as a Mechanism of Progression from Early to Late Endosomes. Cell *122*, 735–749.

Rodal, S.K., Skretting, G., Garred, O., Vilhardt, F., van Deurs, B., and Sandvig, K. (1999). Extraction of cholesterol with methyl-beta-cyclodextrin perturbs formation of clathrin-coated endocytic vesicles. Mol Biol Cell *10*, 961–974.

Roerdink, F., Wassef, N.M., Richardson, E.C., and Alving, C.R. (1983). Effects of negatively charged lipids on phagocytosis of liposomes opsonized by complement. Biochim Biophys Acta *734*, 33–39.

Ross, P.C., and Hui, S.W. (1999). Lipoplex size is a major determinant of in vitro lipofection efficiency. Gene Ther *6*, 651–659.

Roth, M.G. (2006). Clathrin-mediated endocytosis before fluorescent proteins. Nat Rev Mol Cell Biol *7*, 63–68.

Roth, T.F., and Porter, K.R. (1964). Yolk Protein Uptake in the Oocyte of the Mosquito Aedes Aegypti. J Cell Biol *20*, 313–332.

Rothberg, K.G., Heuser, J.E., Donzell, W.C., Ying, Y.S., Glenney, J.R., and Anderson, R.G. (1992). Caveolin, a protein component of caveolae membrane coats. Cell *68*, 673–682.

Rothberg, K.G., Ying, Y.S., Kolhouse, J.F., Kamen, B.A., and Anderson, R.G. (1990). The glycophospholipid-linked folate receptor internalizes folate without entering the clathrin-coated pit endocytic pathway. J Cell Biol *110*, 637–649.

Rothman, J.E., Bursztyn-Pettegrew, H., and Fine, R.E. (1980). Transport of the membrane glycoprotein of vesicular stomatitis virus to the cell surface in two stages by clathrin-coated vesicles. J Cell Biol *86*, 162–171.

Ruponen, M., Rönkkö, S., Honkakoski, P., Pelkonen, J., Tammi, M., and Urtti, A. (2001). Extracellular glycosaminoglycans modify cellular trafficking of lipoplexes and polyplexes. J Biol Chem *276*, 33875–33880.

Ruponen, M., Ylä-Herttuala, S., and Urtti, A. (1999). Interactions of polymeric and liposomal gene delivery systems with extracellular glycosaminoglycans: physicochemical and transfection studies. Biochim Biophys Acta *1415*, 331–341.

Ruponen, M., Honkakoski, P., Tammi, M., and Urtti, A. (2004). Cell-surface glycosaminoglycans inhibit cation-mediated gene transfer. J. Gene Med. *6*, 405–414.

Sabharanjak, S., Sharma, P., Parton, R.G., and Mayor, S. (2002). GPI-anchored proteins are delivered to recycling endosomes via a distinct cdc42-regulated, clathrin-independent pinocytic pathway. Dev Cell *2*, 411–423.

Sahay, G., Kim, J.O., Kabanov, A.V., and Bronich, T.K. (2010). The exploitation of differential endocytic pathways in normal and tumor cells in the selective targeting of nanoparticulate chemotherapeutic agents. Biomaterials *31*, 923–933.

Sahay, G., Querbes, W., Alabi, C., Eltoukhy, A., Sarkar, S., Zurenko, C., Karagiannis, E., Love, K., Chen, D., Zoncu, R., et al. (2013). Efficiency of siRNA delivery by lipid nanoparticles is limited by endocytic recycling. Nat Biotechnol *31*, 653–658.

Salminen, A., and Novick, P.J. (1987). A ras-like protein is required for a post-Golgi event in

yeast secretion. Cell *49*, 527–538.

Sandvig, K., Pust, S., Skotland, T., and van Deurs, B. (2011). Clathrin-independent endocytosis: mechanisms and function. Curr Opin Cell Biol *23*, 413–420.

Schubert, W., Frank, P.G., Razani, B., Park, D.S., Chow, C.W., and Lisanti, M.P. (2001). Caveolae-deficient endothelial cells show defects in the uptake and transport of albumin in vivo. J Biol Chem *276*, 48619–48622.

Sharma, D.K., Choudhury, A., Singh, R.D., Wheatley, C.L., Marks, D.L., and Pagano, R.E. (2003). Glycosphingolipids internalized via caveolar-related endocytosis rapidly merge with the clathrin pathway in early endosomes and form microdomains for recycling. J Biol Chem *278*, 7564–7572.

Simionescu, N., Lupu, F., and Simionescu, M. (1983). Rings of membrane sterols surround the openings of vesicles and fenestrae, in capillary endothelium. J Cell Biol *97*, 1592–1600.

Simões, S., Slepushkin, V., Pires, P., Gaspar, R., Pedroso de Lima, M.C., and Düzgüneş, N. (2000). Human serum albumin enhances DNA transfection by lipoplexes and confers resistance to inhibition by serum. Biochim Biophys Acta *1463*, 459–469.

Sönnichsen, B., de Renzis, S., Nielsen, E., Rietdorf, J., and Zerial, M. (2000). Distinct membrane domains on endosomes in the recycling pathway visualized by multicolor imaging of Rab4, Rab5, and Rab11. J Cell Biol *149*, 901–914.

Stegmann, T., Hoekstra, D., Scherphof, G., and Wilschut, J. (1986). Fusion activity of influenza virus. A comparison between biological and artificial target membrane vesicles. J Biol Chem *261*, 10966–10969.

Stenmark, H., and Olkkonen, V.M. (2001). The Rab GTPase family. Genome Biol *2*, REVIEWS3007.

Stenmark, H. (2009). Rab GTPases as coordinators of vesicle traffic. Nat Rev Mol Cell Biol *10*, 513–525.

Straubinger, R.M., Düzgünes, N., and Papahadjopoulos, D. (1985). pH-sensitive liposomes mediate cytoplasmic delivery of encapsulated macromolecules. FEBS Lett *179*, 148–154.

Straubinger, R.M., Hong, K., Friend, D.S., and Papahadjopoulos, D. (1983). Endocytosis of liposomes and intracellular fate of encapsulated molecules: Encounter with a low pH compartment after internalization in coated vesicles. Cell *32*, 1069–1079.

Straubinger, R.M., Papahadjopoulos, D., and Hong, K.L. (1990). Endocytosis and intracellular fate of liposomes using pyranine as a probe. Biochemistry *29*, 4929–4939.

Suzuki, K., and Namiki, H. (2007). Cytoplasmic pH-dependent spreading of polymorphonuclear leukocytes: regulation by pH of PKC subcellular distribution and F-actin assembly. Cell Biol Int *31*, 279–288.

Szoka, F.C., Jr, Jacobson, K., and Papahadjopoulos, D. (1979). The use of aqueous space markers to determine the mechanism of interaction between phospholipid vesicles and cells. Biochim Biophys Acta *551*, 295–303.

Szoka, F.C., Jr, Jacobson, K., Derzko, Z., and Papahadjopoulos, D. (1980). Fluorescence studies on the mechanism of liposome-cell interactions in vitro. Biochim Biophys Acta *600*, 1–18.

Szoka, F.C., Jr, Magnusson, K.E., Wojcieszyn, J., Hou, Y., Derzko, Z., and Jacobson, K. (1981). Use of lectins and polyethylene glycol for fusion of glycolipid-containing liposomes with eukaryotic cells. Proc Natl Acad Sci USA *78*, 1685–1689.

Tabas, I., Myers, J.N., Innerarity, T.L., Xu, X.X., Arnold, K., Boyles, J., and Maxfield, F.R. (1991). The influence of particle size and multiple apoprotein E-receptor interactions on the endocytic targeting of beta-VLDL in mouse peritoneal macrophages. J Cell Biol *115*, 1547–1560.

Un, K., Sakai-Kato, K., Oshima, Y., Kawanishi, T., and Okuda, H. (2012). Intracellular trafficking mechanism, from intracellular uptake to extracellular efflux, for phospholipid/cholesterol liposomes. Biomaterials *33*, 8131–8141.

Unanue, E.R., Ungewickell, E., and Branton, D. (1981). The binding of clathrin triskelions to membranes from coated vesicles. Cell *26*, 439–446.

van der Bliek, A.M., and Meyerowitz, E.M. (1991). Dynamin-like protein encoded by the Drosophila shibire gene associated with vesicular traffic. Nature *351*, 411–414.

Vigers, G.P., Crowther, R.A., and Pearse, B.M. (1986). Location of the 100 kd-50 kd accessory proteins in clathrin coats. Embo J *5*, 2079–2085.

Walenga, R.W., Opas, E.E., and Feinstein, M.B. (1981). Differential effects of calmodulin antagonists on phospholipases A2 and C in thrombin-stimulated platelets. J Biol Chem *256*, 12523–12528.

Wang, L., and MacDonald, R.C. (2004). Effects of microtubule-depolymerizing agents on the transfection of cultured vascular smooth muscle cells: enhanced expression with free drug and especially with drug-gene lipoplexes. Mol Ther *9*, 729–737.

Weinstein, J.N., Yoshikami, S., Henkart, P., Blumenthal, R., and Hagins, W.A. (1977). Liposome-cell interaction: transfer and intracellular release of a trapped fluorescent marker. Science *195*, 489–492.

Wong, A.W., Scales, S.J., and Reilly, D.E. (2007). DNA internalized via caveolae requires microtubule-dependent, Rab7-independent transport to the late endocytic pathway for delivery to the nucleus. J Biol Chem *282*, 22953–22963.

Woodward, M.P., and Roth, T.F. (1978). Coated vesicles: characterization, selective dissociation, and reassembly. Proc Natl Acad Sci U S A *75*, 4394–4398.

Wrobel, I., and Collins, D. (1995). Fusion of cationic liposomes with mammalian cells occurs

after endocytosis. Biochim Biophys Acta *1235*, 296–304.

Xu, Y., and Szoka, F.C., Jr (1996). Mechanism of DNA release from cationic liposome/DNA complexes used in cell transfection. Biochemistry *35*, 5616–5623.

Yamada, E. (1955). The fine structure of the renal glomerulus of the mouse. J Biophys Biochem Cytol *1*, 551–566.

Yan, X., Kuipers, F., Havekes, L.M., Havinga, R., Dontje, B., Poelstra, K., Scherphof, G.L., and Kamps, J.A.A.M. (2005). The role of apolipoprotein E in the elimination of liposomes from blood by hepatocytes in the mouse. Biochem Biophys Res Commun *328*, 57–62.

Yokota, S. (1982). Immunoelectron microscopic localization of albumin in smooth and striated muscle tissues of rat. Histochemistry *74*, 379–386.

Yoshimura, T., Shono, M., Imai, K., and Hong, K. (1995). Kinetic analysis of endocytosis and intracellular fate of liposomes in single macrophages. J Biochem *117*, 34–41.

Zaitseva, E., Yang, S.-T., Melikov, K., Pourmal, S., and Chernomordik, L.V. (2010). Dengue virus ensures its fusion in late endosomes using compartment-specific lipids. PLoS Pathog *6*, e1001131.

Zelphati, O., and Szoka, F.C., Jr (1996a). Mechanism of oligonucleotide release from cationic liposomes. Proc Natl Acad Sci USA *93*, 11493–11498.

Zelphati, O., and Szoka, F.C., Jr (1996b). Intracellular distribution and mechanism of delivery of oligonucleotides mediated by cationic lipids. Pharm Res *13*, 1367–1372.

Zhou, X., and Huang, L. (1994). DNA transfection mediated by cationic liposomes containing lipopolylysine: characterization and mechanism of action. Biochim Biophys Acta *1189*, 195–203.

Zhu, D., Lennon, S.P., Peters, M.H., Finney, W.C., and Singh, M. (2006). Brownian diffusion and surface kinetics of liposome and viral particle uptake by human lung cancer cells in-vitro. Ann Biomed Eng *34*, 1573–1586.

Zuhorn, I.S., Kalicharan, R., and Hoekstra, D. (2002a). Lipoplex-mediated transfection of mammalian cells occurs through the cholesterol-dependent clathrin-mediated pathway of endocytosis. J Biol Chem *277*, 18021–18028.

Zuhorn, I.S., Visser, W.H., Bakowsky, U., Engberts, J.B.F.N., and Hoekstra, D. (2002b). Interference of serum with lipoplex-cell interaction: modulation of intracellular processing. Biochim Biophys Acta *1560*, 25–36.

Chapter 2 : Tool Creation

2.1 Introduction

A major research focus in cell biology has been to delineate the components and pathways of communication among intracellular compartments and the extracellular environment in eukaryotic cells. This research has led to the identification of a variety of proteins that co-localize with specific intracellular compartments and that are used as markers to identify the respective compartment. In the past 15 years, fluorescent protein fusions to compartment specific proteins have been created using recombinant techniques that are used to colocalize materials with complementary fluorescence to the tagged compartment (Doherty and McMahon, 2009; Rappoport and Simon, 2008; Roth, 2006). However, it is important to recognize the numerous studies that have preceded, which allow for the large toolkit of compartment specific markers currently used. It is often found that fluorescent protein fusions cause perturbations in protein function. For example, any addition to the N-terminus of the Cystic fibrosis transmembrane conductance regulator (CFTR) disrupts function (Chan et al., 2000). Thus it is important to use similar constructs to those that have been previously characterized to recapitulate wild type protein localization and function or perform control experiments on new constructs to validate that they colocalize with the expected compartment.

The internalization pathways dependent upon: clathrin, caveolin, and flotillin have all been studied dynamically in living cells with fluorescent fusion proteins. Fusion of green fluorescent protein (GFP) to either the C- or N- termini of the clathrin light chain, CltA, are functional, which was first noted in the original paper investigating clathrin dynamics (Gaidarov et al., 1999). Colocalization of CltA-GFP with endogenous clathrin, AP-2 complex, and transferrin

confirmed that the fusion is structurally and functionally active. GFP fusion to the C-terminus of caveolin-1 (Cav1) is functional as it colocalizes with unlabeled Cav1 and allows normal SV40 infection (Pelkmans et al., 2001). However, fusion of GFP to the N-terminus of Cav1 is a dominant-negative inhibitor of SV40 entry, which requires caveolae for productive infection. N- or C-terminal fusions to flotillin-1 (Flot1) are indistinguishable from the native protein, and colocalization between Flot1-GFP and CD59 is observed (Glebov et al., 2006; Santamaría et al., 2005). Low levels of Flot1-GFP expression recapitulates the endogenous localization, but higher levels saturate the pathway and uniform cellular distribution is observed (Frick et al., 2007). Thus both CltA and Flot1 are functional when fused at either terminus, but Flot1 localization is sensitive to expression levels. Cav1, however, can only be fused at the C-terminus to recapitulate wildtype function and localization.

Subsequent to cellular entry, there are a multitude of endosomal compartments that sort, recycle, and degrade endocytosed material (Mukherjee et al., 1997). The best characterized compartments are early-to-late endosomes, recycling and sorting compartments, and the lysosome. The Rab family of small GTPases constitute the largest set of regulatory proteins involved in endocytosis (Stenmark and Olkkonen, 2001). The best characterized are Rab5a, Rab7a, Rab4a, and Rab11a that regulate early, late, quick recycling and slow recycling endosomes, respectively. These Rab family small GTPases have all been fused at their N-termini to fluorescent proteins and demonstrated to localize faithfully to their respective compartments (Bucci et al., 2000; Sönnichsen et al., 2000). It appears that all fusions to the N-termini of Rab proteins are functional, however, the C-terminus is involved in subcellular targeting and consequently must remain unmodified for proper function and localization (Chavrier et al., 1991). The

multivesicular body (MVB) constitutes a loosely defined compartment that is involved in sorting and recycling, among other cellular functions. CD82 is a tetraspanin family member that has been demonstrated to localize to MVBs by immunoelectron microscopy, and fusion of yellow fluorescent protein (YFP) to the N-terminus of human CD82 has been demonstrated to localize similarly to wildtype protein (Escola et al., 1998; Sherer et al., 2003). Lastly, LAMP-1 is one member of a large family of heavily glycosylated membrane proteins found in the lysosome (Chen et al., 1988). Fusion of GFP to the C-terminus of LAMP1 was demonstrated to localize to late endocytic organelles (Falcón-Pérez et al., 2005).

The literature validates that many endosomal markers can remain functionally active when fused to fluorescent proteins, and can serve as proxy for endosomal compartments. The specific endosomal makers described above are used in the following studies. However, the fusions were re-created with cyan fluorescent protein (CFP) using the endogenous human proteins and put under the control of an inducible promoter. Stable cell lines with these fusion products were created with lentivirus to enable a more homogeneously labeled population of cells than can be achieved by transfection. HeLa cells were chosen for all studies because of their flat shape that is optimal for microscopy and they are easily transfectable. Control experiments to tune expression levels of the fluorescent protein markers and generate standard curves of FITC-dextran were performed and described below.

Protein / Species	Compartment	Vector / Fluorescent Protein	Reference
*CltA / Murine	Clathrin	pEGFP-C1 / GFP	Gaidarov, 1999
CltA* / Murine	Clathrin	pEGFP-N1 / GFP	Gaidarov, 1999
Cav1* / Canine	Caveolae	pEGFP-N1 / GFP	Pelkmans, 2001
FLOT1* / Murine	Flotillin	pEGFP-N1 / GFP	Glebov, 2006
*FLOT1 / Human	Flotillin	pEGFP-C1 / GFP	Santamaria, 2005
*Rab4a / Human	Early recycling endosome	pEGFP-C3 / GFP	Sonnichsen, 2000
*Rab4a / Human	Early recycling endosome	pEYFP-C3 / YFP	Sonnichsen, 2000
*Rab5a / Human	Early endosome	pEGFP-C3 / GFP	Sonnichsen, 2000
*Rab5a / Human	Early endosome	pECFP-C3 / CFP	Sonnichsen, 2000
*Rab11a / Human	Late recycling endosome	pEGFP-C3 / GFP	Sonnichsen, 2000
*Rab11a / Human	Late recycling endosome	pEYFP-C3 / YFP	Sonnichsen, 2000
*Rab11a / Human	Late recycling endosome	pECFP-C3 / CFP	Sonnichsen, 2000
*Rab7a / Canine	Late endosome	pEGFP-C1 / GFP	Bucci, 2000
LAMP1* / Human	Late endosome / Lysosome	pEGFP-N3 / GFP	Falcon-Perez, 2005
*CD82 / Human	Multi-vesicular body	pEYFP-C1 / YFP	Escola, 1998 Sherer, 2003

Table 2.1 Fluorescent fusions to validated endosomal compartment specific markers.
The compartment that each protein labels is indicated, and the vector and fluorescent protein that the fusion was created in is shown along with the reference. (*) Indicates the end that the fluorescent protein is fused to, i.e. *CD82 denotes an N-terminal fusion to CD82 generating YFP-CD82.

Determination of cellular organelle pH via ratiometric microscopy using fluorescent indicators is well established (Haggie and Verkman, 2009; O'Connor and Silver, 2007). Fluorescein isothiocyanate (FITC) is a fluorescein derivative commonly used for intracellular pH determination (Lanz et al., 1997). FITC is a useful pH probe as it is easily added to primary amines, and exhibits an internalized pH responsiveness at its pH sensitive excitation wavelength of 491 nm and a pH insensitive excitation at its isosbestic point near 435 nm. In addition FITC has a pKa of ~6.5, which is well suited for physiological pH measurements between pH 5 and 7.

2.2 Methods

2.2.1 Cell Culture

HEK293T, HeLa and all HeLa derivatives containing endosomal marker fusions were maintained in T75 flasks between 10-90% confluence (100% confluent T75 yields ~10 x 10^6 total cells) in RPMI 1640 supplemented with 10% heat inactivated FBS (Gibco, Life Technologies, Benicia, CA) and 25 mM HEPES in a humidified atmosphere with 5% CO_2 at 37 ^oC.

For microscopy studies, HeLa and HeLa derivative cells were cultured in RPMI 1640 supplemented with 10% defined FBS (HyClone, Thermo Fisher, Waltham, MA) and 25 mM HEPES. 48 hours prior to microscopy, cells were seeded at 300,000 cells per 35 mm uncoated glass coverslip bottom FluoroDish (World Precision Instruments, Sarasota, FL). The media was changed 24 hours later and if induction was used, 10 μg/mL doxycycline was added at that time to induce fluorescent marker expression. On the day of imaging, the plate was 90% confluent at ~1,200,000 cells per dish. During imaging experiments, the cells were maintained in PBS supplemented with 6 mM glucose and 1.1 mM pyruvate (PBSgp).

2.2.2 Materials

All cell culture reagents were supplied by the UCSF Cell Culture Facility. Fluorescein isothiocyanate (FITC), amino dextran (40 kDa), and Lysosensor Blue DND-167 were obtained from Molecular Probes (Eugene, OR).

2.2.3 DNA Constructs

All endosomal compartment markers were amplified from a cDNA library made from HeLa cells using SuperScript III First Strand Synthesis System (Invitrogen, Carlsbad, CA).

mTurquoise from pRSET-mTurquoise was amplified using primers 5'-CCGGGATCCACCGGTCGCCACCATGGTGAGCAAGGGCGAG and 5'-GTCGCGGCCGCTTTACTTGTACAGCTCGTC and replaced GFP in pEGFP-N1 between the BamHI and NotI sites to create pmTurquoise-N1. Similarly, mTurquoise from pRSET-mTurquoise was amplified using primers 5'-GCTACCGGTCGCCACCATGGTGAGCAAGGGCGAG and 5'-GAGTCCGGACTTGTACAGCTCGTCCAT and replaced GFP in pEGFP-C1 between the AgeI and BspEI sites to create pmTurquoise-C1.

pCltA-mTurquoise, pCav1-mTurquoise, and pLAMP1-mTurquoise were constructed by PCR amplifying the sequences from a cDNA library made from HeLa cells using gene specific primers listed in Table 2.1. For Cav1 and LAMP1 the PCR products were cloned between the XhoI and BamHI sites in pmTurquoise-N1. For CltA the PCR product was clones between the XhoI and AgeI sites in pmTurquoise-N1.

pmTurquoise-CD82, pmTurquoise-FLOT1, pmTurquoise-Rab4a, pmTurquoise-Rab5a, pmTurquoise-Rab7a, and pmTurquoise-Rab11a were constructed by PCR amplifying the sequences from a cDNA library made from HeLa cells using gene specific primers listed in Table 2.1. For Rab4a, Rab5a, Rab7a, and Rab11a the PCR products were cloned between the XhoI and BamHI sites in pmTurquoise-C1. For FLOT1 the PCR product was cloned between the XhoI and EcoRI sites in pmTurquoise-C1. For CD82 the PCR product was cloned between the XhoI and XbaI sites in pmTurquoise-C1.

To create the lentiviral constructs under doxycycline induction, pLVX-Tight-Puro (Clontech, Mountain View, CA) was first modified to remove the XhoI site 5' to the Ptight promoter by QuikChange mutagenesis (Agilent, Santa Clara, CA). Then a new MCS (Table 2.1) was added between the BamHI and MluI sites to introduce XhoI, BstBI, and XbaI. For CltA, Cav1, and LAMP1 the mTurquoise fusions were digested from the pmTurquoise-N1 versions using XhoI and XbaI and cloned into the modified pLVX-Tight-Puro between the same sites. For CD82, FLOT1, Rab4a, Rab5a, Rab7a, and Rab11a the mTurquoise fusion were amplified from the pmTurquoise-C1 version using 5'-GTACAGCCTTCGAACGCCACCATGGTGAGCAAGGGCGAG and 5'-CCTCTACAAATGTGGTATGG, digested with BstBI and XbaI and cloned into the modified pLVX-Tight-Puro between the same sites.

pLenti-UbC-rtTA and pLVX-Tight-Puro were kindly provided by Warner C. Greene (Gladstone Institute). pRSET-mTurquoise was kindly provided by Kurt Thorn (UCSF). All oligos were purchased from Integrated DNA Technologies (Coralville, IA). All restriction enzymes were from New England Biolabs (Ipswich, MA).

All constructs were confirmed by sequence analysis by McLab (South San Francisco, CA).

Gene Name	NCBI Reference Sequence	CDS Length (nts)	Forward Primer	Reverse Primer
Cav1	NM_001753	537	GATCTCGAGCGCCACCATGTCTGGGGGCAAATAC	GGTGGATCCGGTATTTCTTTCTGCAAGTT
CltA	NM_001833	657	GATCTCGAGCGCCACCATGGCTGAGCTGGATCCG	GCGACCGGTGGGTGCACCAGCGGGGCCTG
CD82	NM_002231	804	GATCTCGAGGGATGGGCTCAGCCTGTATC	TTATCTAGATCAGTACTTGGGGACCTT
FLOT1	NM_005803	1,284	GATCTCGAGGGATGTTTTTCACTTGTGGC	GCAGAATTCTCAGGCTGTTCTCAAAGG
LAMP1	NM_005561	1,254	GATCTCGAGCGCCACCATGGCGGCCCCCGGCAGC	GGTGGATCCGGGATAGTCTGGTAGCCTGC
Rab4a	NM_004578	657	GATCTCGAGGGATGTCGCAGACGGCCATG	GGTGGATCCCTAACAACCACACTCCTG
Rab5a	NM_004162	648	GATCTCGAGGGATGGCTAGTCGAGGCGCA	GGTGGATCCTTAGTTACTACAACACTG
Rab7a	NM_004637	624	GATCTCGAGGGATGACCTCTAGGAAGAAAG	GGTGGATCCTCAGCAACTGCAGCTTTC
Rab11a	NM_004663	651	GATCTCGAGGGATGGGCACCCGCGACGAC	GGTGGATCCTTAGATGTTCTGACAGCA
MCS			GATCCCTCGAGGCCTTCGAAGGCTCTAGATCGCGAA	CGCGTTCGCGATCTAGAGCCTTCGAAGGCCTCGAGG

Table 2.2 Primer sequences used in this study.

2.2.4 Preparation of Virus and Transduction

24 hours before transfection, 300,000 HEK293T cells were seeded into a 6-well plate. The day of transfection, 2 mL of fresh media was added to the cells. For each transfection 3 µL of Lipofectamine 2000 was added to 100 µL of serum free media and incubated for 5 minutes and room temperature. 0.5 µg of marker plasmid was combined with 0.167 µg of each packaging vectors: pVSV-G, pMDL, and pRSV-Rev (Kindly provided by Michael T. McManus, UCSF). The plasmid and Lipofectamine 2000 (Life Technologies, Benicia, CA) mixtures were combined and incubated for 20 minutes at room temperature. This mixture was added directly to the cells

and incubated for 72 hours. The virus containing media was removed from the cells and filtered though a 0.45 μm filter.

HeLa cells were plated at 50,000 cells per well in a 6-well plate. The following day 1 mL of 2x media and 1 mL of media containing virus were combined and allowed to incubate until the well became confluent. The cells were split into a T75 flask and the following day 4 μg/mL of puromycin was added to the flask for selection. The mixture of puromycin resistant cells were used for subsequent studies without further clonal selection.

HeLa-TetOn cells were created using concentrated virus provided by the UCSF Lentiviral core made from pLenti-UbC-rtTA. 100,000 cells were infected with 10 μL of concentrated virus in the presence of 4 μg/mL polybrene. Positive cells were selected with G418 at 400 μg/mL.

2.2.5 Synthesis of FITC-dextran

1 gram of amino dextran (40 kDa) was dissolved in 100 mM sodium bicarbonate at pH 8.4 to 25 mg/mL. A 2-fold molar excess of FITC was added and incubated for 1 hour in the dark at room temperature shaking. The reaction was dialyzed extensively against water with 10 kDa MWCO membrane (Spectrum, New Brunswick, NJ). The conjugate was confirmed to be free of unreacted dye by size exclusion chromatography and exchanged into PBSgp with a PD-10 desalting column (GE Healthcare Life Sciences, Piscataway, NY).

2.2.6 pH Calibration of FITC-dextran

An 8-well chamber slide (Lab-Tek, Thermo Fisher Scientific Inc., Waltham, MA) was seeded with 10,000 cells per chamber. 24 hours later 12.5 mg/mL FITC-dextran in PBSgp was added to

the cells and incubated for 30 minutes at 37 ^{o}C. The cells were subsequently washed extensively with PBS to remove unbound fluorescence. The intracellular pH in all cellular compartments was clamped by incubation in high K^+ solutions containing the ionophores bafilomycin A1 (100 nM), nigericin (10 μM) valinomycin (10 μM) and carbonyl cyanide m-chlorophenyl hydrazone (CCCP, 10 μM). The pH buffers all contained 120 mM KCl, 20 mM NaCl, 1 mM $CaCl_2$, 1 mM $MgCl_2$. pH 4 and 5 buffers contained 50 mM acetic acid. pH 5.5, 6, and 6.5 buffers contained 50 mM MES. pH 7 and 8 buffers contained 50 mM HEPES. pH 9 buffer contained 20 mM Tris. The cells were incubated for 5 minutes before imaging to equilibrate the intracellular pH. Fluorescence ratios at the clamped pH values were fitted to the following equation:

$$\frac{F_{491nm}}{F_{430nm}} = B + \frac{T-B}{1+10^{(pKa-pH)n_H}} \quad \textbf{(Equation 1)}$$

where F is the fluorescence signal in the 491nm and 430nm channels, B and T are the amplitude and offset factors, respectively, pKa is the acid dissociation constant and n_H is the Hill constant.

2.2.7 Microscopy and Image Analysis

Images were acquired on a Nikon Eclipse Ti-E inverted microscope equipped with an In Vivo Scientific temperature controlled chamber with humidification and CO_2 control, infrared autofocus, 100x 1.4 numerical aperture Plan Apo objective, Photometrics Coolsnap HQ2 CCD camera, and Sutter Lambda XL lamp. Filters used were 89000 Sedat Quad, 89021 GFP/mCherry, and 89002 Dual CFP/YFP (Chroma Technology, Bellows Falls, VT). Image acquisition was performed using NIS Elements software and image analysis was performed using NIH ImageJ. For ratiometric pH determination images were taken using the ET490/20x, ET525/36m and ET430/24x, ET535/30m filters of the Sedat Quad and Dual CFP/YFP sets, respectively, with 100 ms exposure. CFP fusions were imaged using the ET430/24x, ET470/24m filters of the Dual

CFP/YFP set with a 100 ms exposure. DiD was imaged using the ET645/30x and ET705/72m filters of the Sedat Quad set with 500 ms exposure and 2x2 binning. TEX615 labeled siRNA was imaged using the ET572/35x and ET632/60m filters of the GFP/mCherry set with 500 ms exposure and 2x2 binning.

Image analysis was performed using freely available Fiji plugins and some were written in *de novo*. Images were first deconvolved using the Parallel Spectral Deconvolution plugin (Piotr Wendykier) using a point spread function generated by the Diffraction PSF 3D plugin (Bob Dougherty). Deconvolved images were then background subtracted and 3D Gaussians were fit to the image using a modified GaussianFit plugin (Nico Stuurman). The X and Y coordinates of each fitted Gaussian spot in each frame were then colocalized with spots in other channels. Colocalization was defined as the center point of one Gaussian spot fitting within the width of a Gaussian spot from another channel.

2.3 Results

2.3.1 Amplification of Coding Sequences from cDNA Library and Sub-cloning into pmTurquoise-N1 or pmTurquoise-C1

PCR products for each coding sequence (CDS) were obtained using the primers listed in Table 2.2. Phusion DNA polymerase (New England Biolabs, Ipswich, MA) was used for each amplification with an annealing temperature of 60 ^{o}C and an elongation time of 1 minute. Products of the expected size were obtained for all genes and subsequently digested and cloned into the appropriate pmTurquoise vector detailed in the methods section (Figure 2.1). After identifying clones with the correct length PCR product cloned into the vector, each construct was confirmed by sequencing.

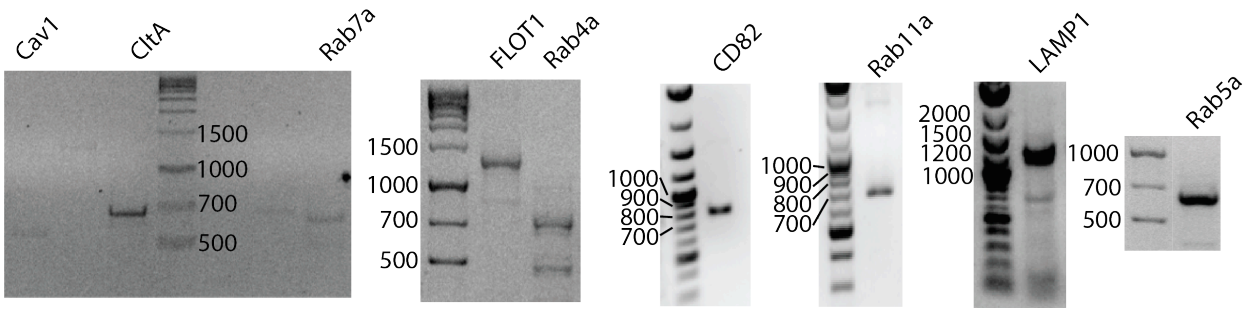

Figure 2.1 PCR products of endosomal markers from HeLa cDNA library.
PCR products obtained that were subsequently cloned into pmTurquoise vectors. Expected sizes are listed in Table 2.2.

2.3.2 Transferring the mTurquoise-CDS Fusions into pLVX-Tight-Puro

After sub-cloning, the fusions between mTurquoise and the coding sequences were transferred into the doxycycline inducible lentiviral plasmid, pLVX-Tight-Puro. The fusions were either cut out directly from the sub-cloning vector with restriction enzymes or amplified by PCR as detailed in the methods. Figure 2.2 shows the gene fusions for each mTurquoise-CDS fusion. All constructs gained the expected ~720 nt size after fusion to mTurquoise. After the inserts were cloned into pLVX-Tight-Puro the constructs were confirmed by sequencing (Figure 2.3).

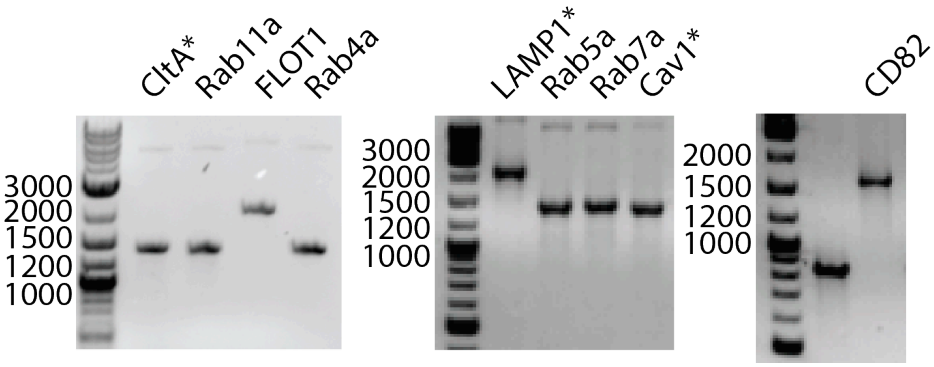

Figure 2.2 mTurquoise-CDS fusions cloned into pLVX-Tight-Puro.
The markers have an additional ~720 nts added to the expected sizes listed in Table 2.2 as a result of mTurquoise fusion.

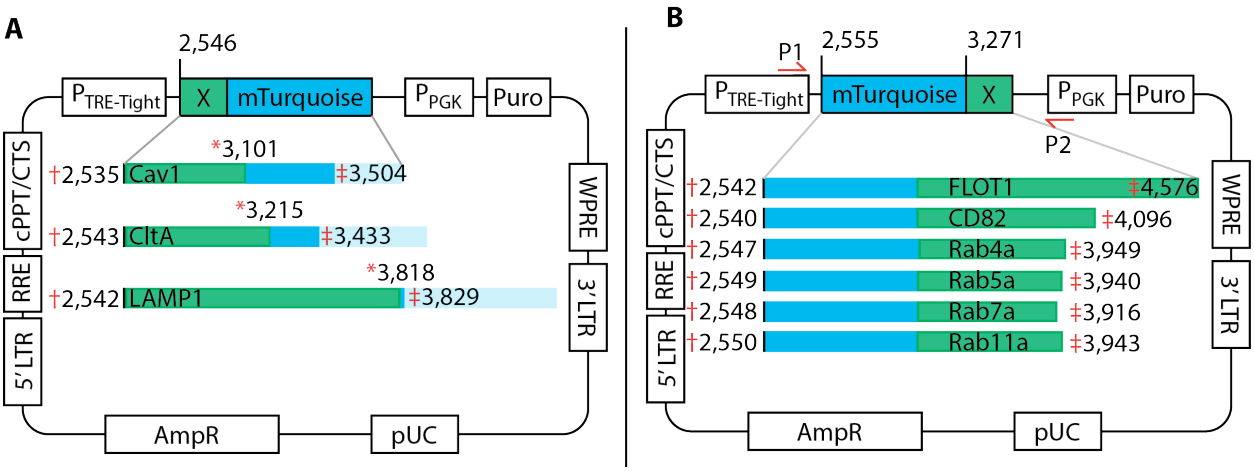

Figure 2.3 Lentiviral constructs.
The numbers indicated are nucleotide positions in the vectors. † indicates the first nucleotide sequenced. ‡ indicates the last nucleotide sequenced. A) * indicates the first nucleotide of mTurquoise. These three constructs were cloned in via restriction enzymes. Sequence results are from the sub-cloning into pmTurquoise. In all cases the entire CDS and 3' junction with mTurquoise is fully sequenced. B) These 6 constructs were cloned via PCR amplification, thus they were fully re-sequenced using primers P1 and P2.

2.3.3 Creation of Cell Lines and Optimizing Doxycycline Inducible mTurquoise-CDS Fusions

Concentrated virus expressing the reverse tetracycline transactivator (rtTA) from the murine Ubiquitin C (UbC) promoter was obtained from the UCSF ViraCore and used directly to make the HeLa-TetON cell line. The viral titer was estimated by the viral core to be 10^8 - 10^9 IFU/mL, thus the approximate MOI was between 10 - 100. This high level of MOI was used to ensure the tightest possible regulation of the $P_{TRE\text{-}Tight}$ promoter. After selection with G418, the pooled cell population was used; clonal selection was not performed.

Subsequent infections were performed at an MOI of 0.1 to ensure that 10% of the cell population was infected with a single viral particle and 90% of the cell population remained un-transduced as described by the Poisson distribution. After selection with puromycin, the pooled cell population was used; clonal selection was not performed. The optimal doxycycline concentration for each marker was determined, and found to be between 5 and 15 µg/mL for all constructs,

with 10 μg/mL being suitable for all markers used (Figure 2.4 and Figure 2.5). In general, at low doxycycline concentrations (1 μg/mL and lower) a few faint puncta are observed and as the concentration of doxycycline is increased, the number of puncta increase as well. At higher levels of doxycycline induction (50 μg/ml), abnormal tubule structures were observed along with retention of fluorescence in the perinuclear region of the cell (Figure 2.6). In addition, it was observed that tetracycline free FBS was not required for any of the cell lines used, as there was no detectable difference between cells grown in tetracycline free FBS or the normal heat inactivated FBS used (Methods).

Similar to the disruption of localization caused by high levels of induction, it was also noted that prolonged passage of cells resulted in aberrant localization even at low doxycycline concentrations. These effects were much more pronounced then the subtle differences caused by strong doxycycline induction. Similar to the images shown in Figure 2.6, cells that had been passaged too long displayed large vacuolar like structures that were virtually identical between markers. As a consequence, cells were not used for colocalization experiments after 5 passages although the aberrant effects described were only observed after 10 passages. No other effects were observed that differentiated the cell lines from one another. The doubling time, ~24 hours, was the same as the parent HeLa cell line used, and there were no changes in gross morphology observed.

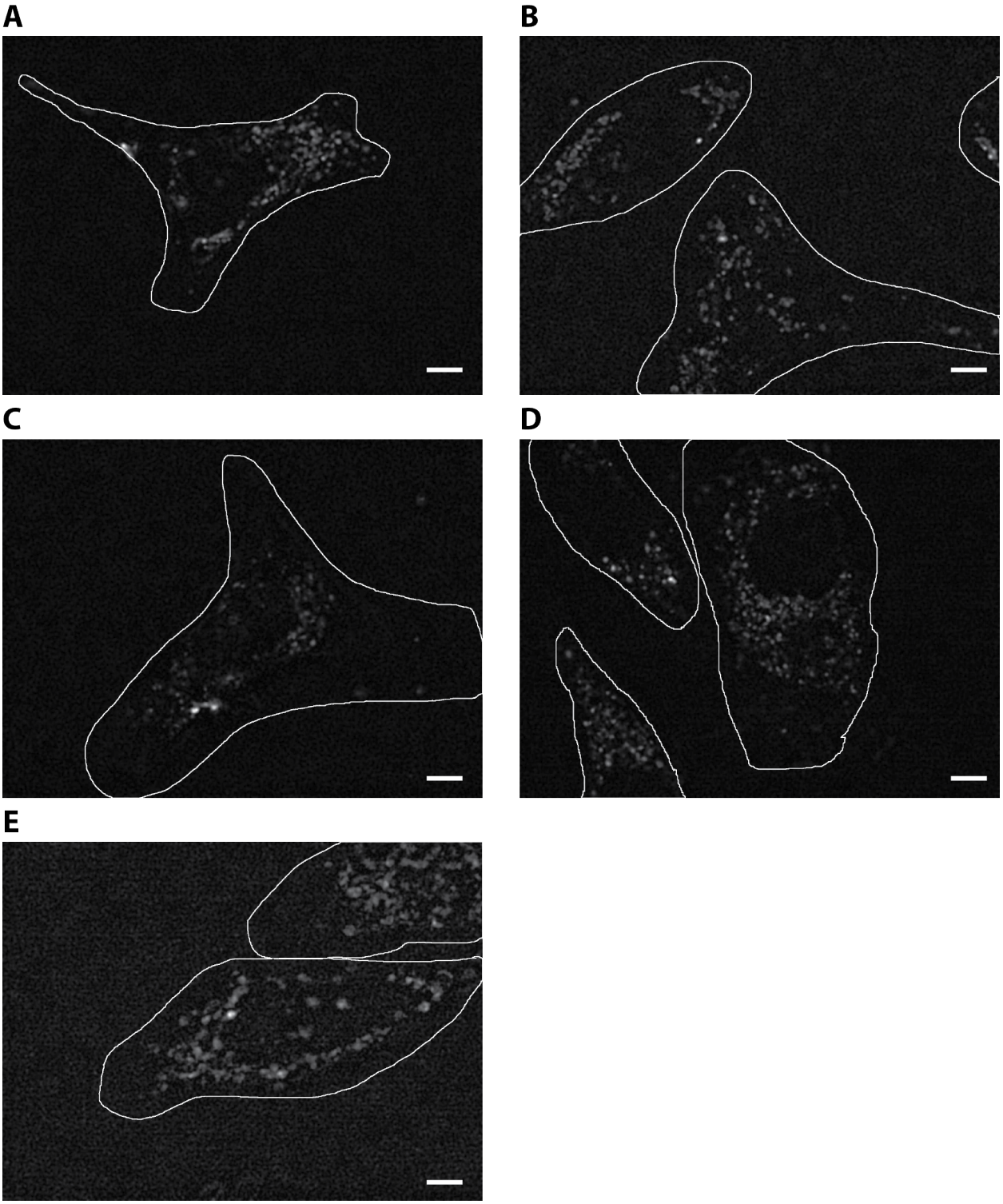

Figure 2.4 Doxycycline induction of mTurquoise-CDS fusions to early endosomal markers. **Deconvolved images of early endosomal markers induced at 10 µg/ml doxycycline. The approximate cell outline is indicated based upon a phase contrast image. Markers are Cav1 (A), CltA (B), Flot1 (C), Rab5a (D), and Rab4a (E). Scale bars are 5 µm.**

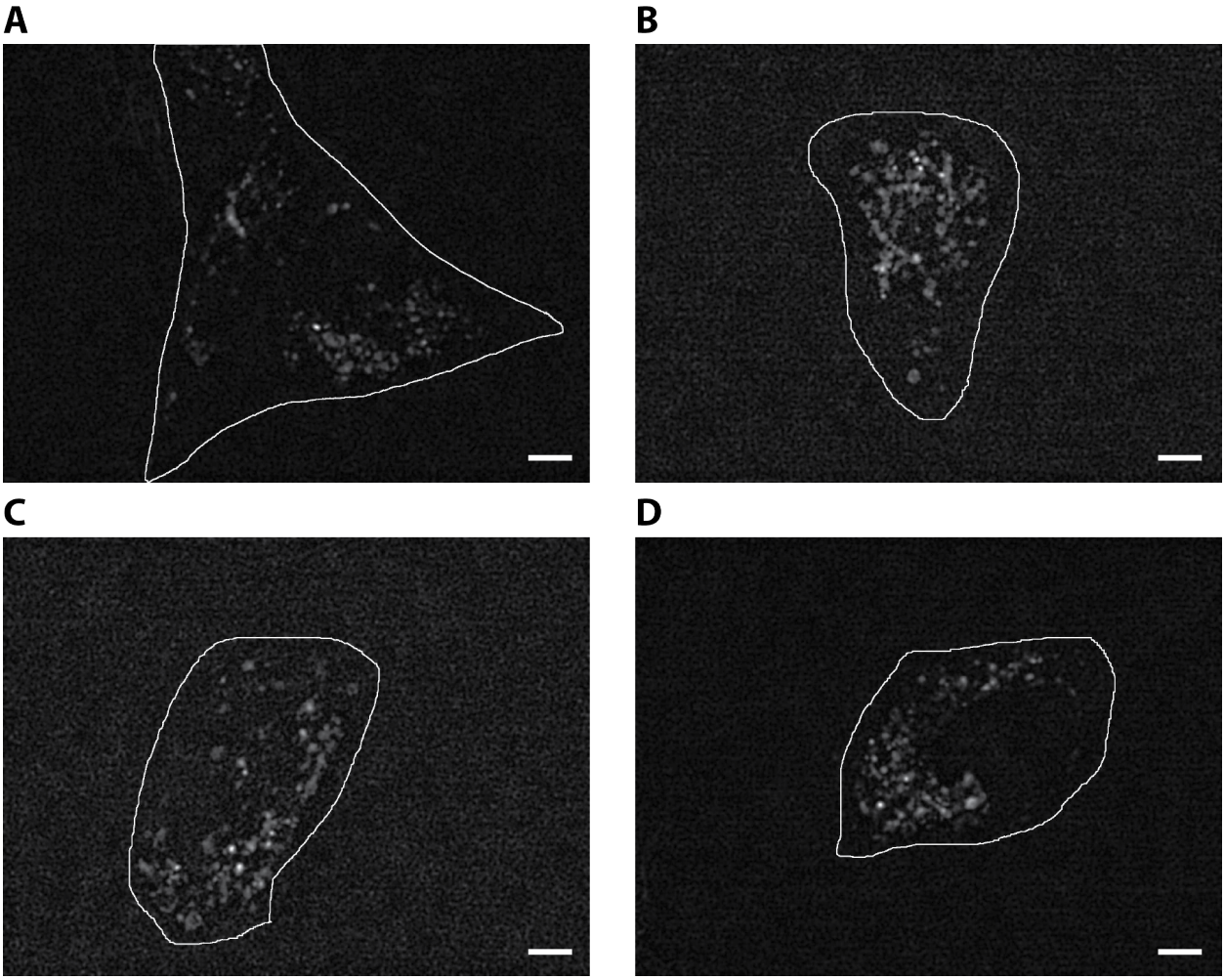

Figure 2.5 Doxycycline induction of mTurquoise-CDS fusions to late endosomal markers. **Deconvolved images of late endosomal markers induced at 10 µg/ml doxycycline. The approximate cell outline is indicated based upon a phase contrast image. Markers are CD82 (A), Rab11a (B), Rab7a (C), and LAMP1 (D). Scale bars are 5 µm.**

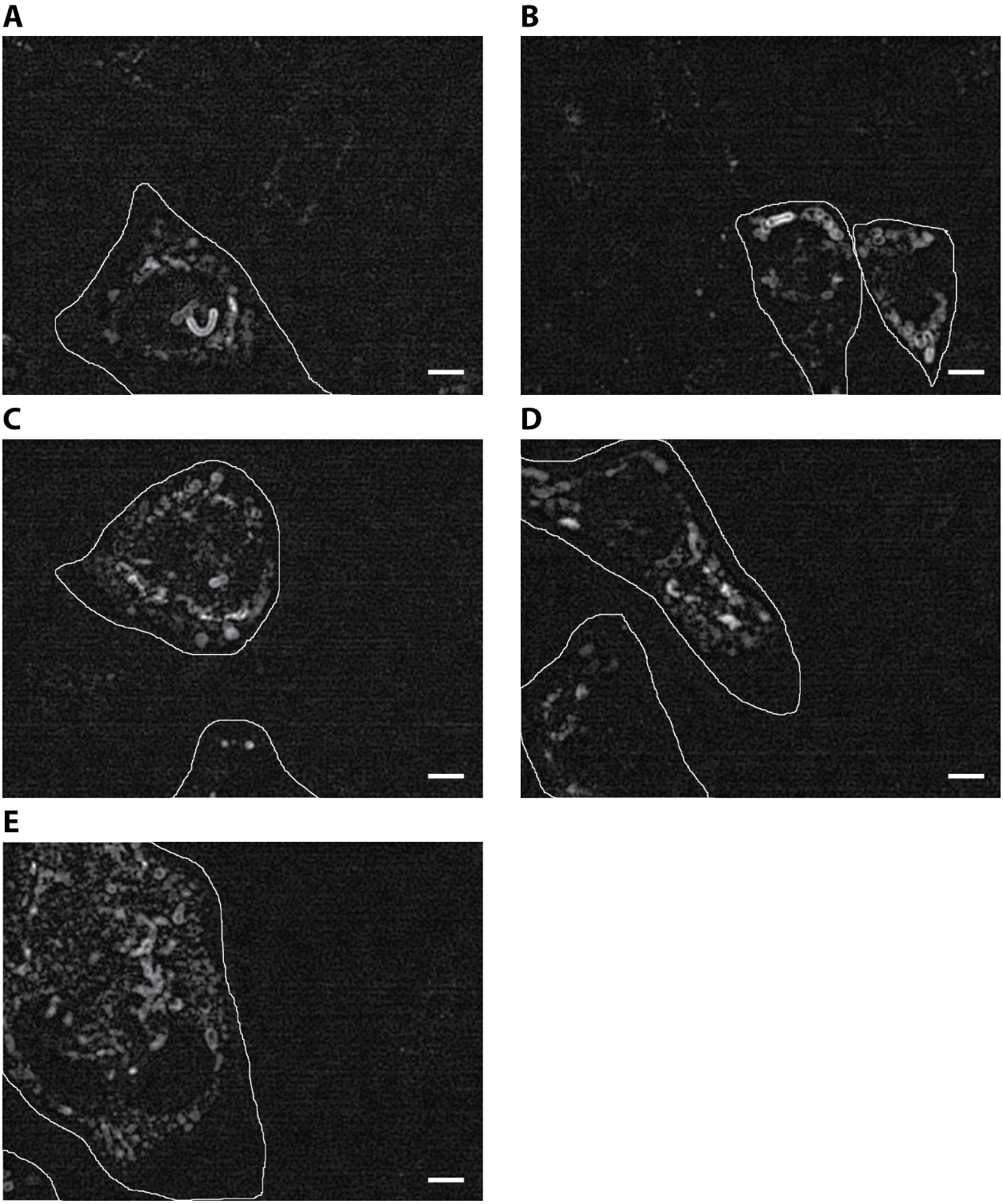

Figure 2.6 Aberrant localization caused by high doxycycline induction or prolonged passage of mTurquoise-CDS fusions.

Deconvolved images of endosomal markers induced at 50 µg/ml doxycycline. The approximate cell outline is indicated based upon a phase contrast image. Markers are Cav1 (A), FLOT1 (B), Rab11a (C), Rab7a (D), and LAMP1 (E). Scale bars are 5 µm.

2.3.4 Intracellular pH Calibration of FITC-dextran

The *in situ* calibration of pH and the ratio between images of FITC-dextran excited at 491 nm and 440 nm was determined described in the Methods section (Figure 2.7). There are two calibration curves in Figure 2.7: one acquired using full illumination used for the calculation of pH in the presence of liposomal formulations detailed in Chapter 3 (Figure 2.7A), and one that was acquired using attenuated illumination for comparison (Figure 2.7B).

The calibration curved used for all measurements of pH in Chapter 3 has a measured pKa of 6.31 +/- 0.05 (S.E.M.) and a Hill slope of 0.93 +/- 0.08 (S.E.M.) (Figure 2.7A). A second calibration curve was acquired using lamp attenuation (Figure 2.7B). The shutter aperture was decreased causing a lamp power reduction from 21.1 mW to 5.5 mW, equivalent to a neutral denisty 0.6 filter (25% transmittance). This allowed me to determine the effect of photobleaching on the calibration. There is a reduced dynamic range as a consequence of the lower lamp intensity. However, the measured pKa of 6.40 +/- 0.06 (S.E.M.) and Hill number of 1.0 +/- 0.11 (S.E.M.), are not statistically different from the calibration done in the absence of lamp attenuation. Overall, these calibration curves are similar to published results of FITC-dextran conjugates with measured pKa values ranging from 6.3 to 6.5 (Geisow, 1984; Sonawane et al., 2003; Haggie, 2007).

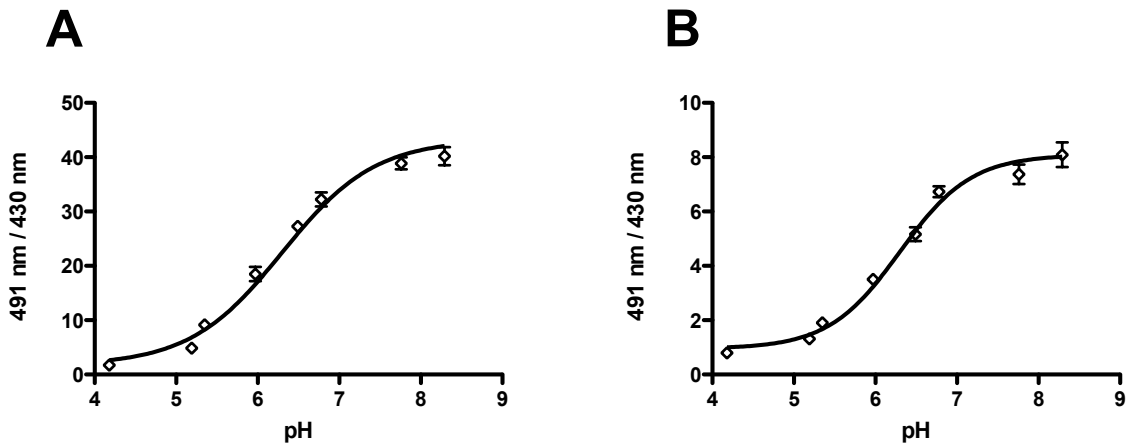

Figure 2.7 FITC-dextran pH calibration curves.
HeLa cells were pulsed with FITC-dextran (40-kDa) for 30 minutes at 37 ^{o}C. The cells were then washed and incubated with specific pH buffers containing high K^{+} and ionophores. Average data +/- S.E.M. are shown for two triplicate experiments using full lamp illumination (A). Average data +/- S.E.M. are shown for triplicate experiments using 25% lamp illumination (B). Number of endosomes analyzed range from 1,423 to 7,039 per pH clamp.

The distributions of the ratios between 491 nm and 430 nm channels at all clamped pH values are shown in Figure 2.8 for the calibration curve used in Chapter 3 (Figure 2.7A). All of the distributions are significantly different from each other after Bonferroni's correction for multiple comparisons. These data indicate that the calibration curve can be used to determine any differences between the liposomal formulations tested in Chapter 3.

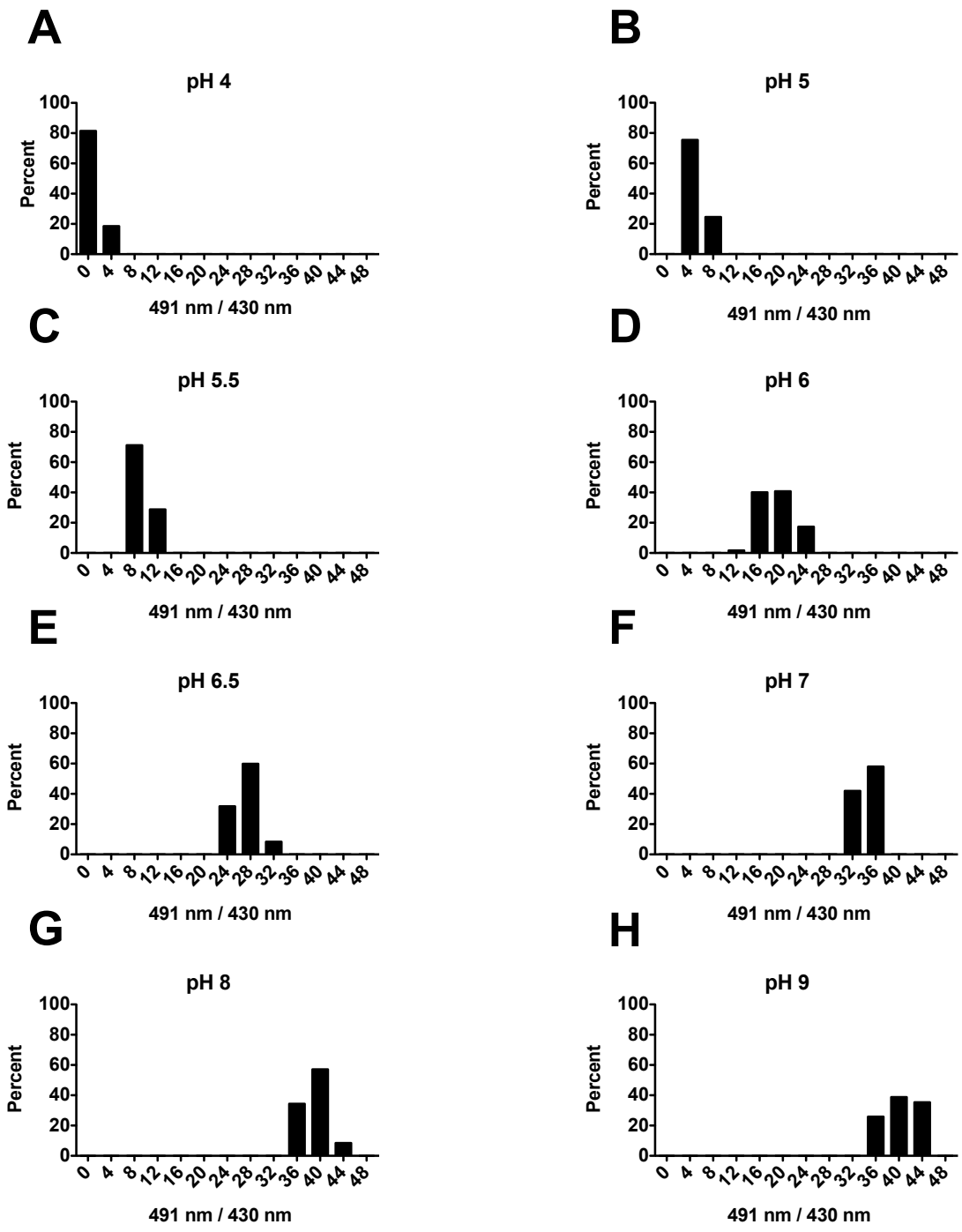

Figure 2.8 Histograms of pH calibration curve ratio data.
All of the data points for the ratios that made the calibration curve in Figure 2.7A are plotted as histograms with the 491 nm and 430 nm ratios on the X-axis. The histograms at pH 4 (A), 5 (B), 5.5 (C), 6 (D), 6.5 (E), 7 (F), 8 (G), and 9 (H) are shown.

The effect of FITC photobleaching was also formally determined under continuous illumination (Figure 2.9). In the absence of lamp power attenuation for the 491 nm channel (21.1 mW), there was 10.3% +/- 0.6% (S.E.M.) signal reduction after one exposure. Attenuation of the lamp intensity in the 491 nm channel by 75% (5.5 mW), reduced the effect of photobleaching by half to 5.6% +/- 0.3% (S.E.M.) after one exposure. The effect of photobleaching in the 430 nm channel was even lower at 2.3% +/- 0.2% (S.E.M.) after one exposure using full illumination with 12.6 mW intensity light. In all of these calculations, background subtracted images were used. As a consequence of the amount of photobleaching using full illumination, only data from a single exposure is used in all experimental calculations of pH described in Chapter 3.

The hardware limitations of the microscope prevented using a neutral density filter for further experiments. The neutral density filter port cannot be automated on the Ti-E microscope, and the far-red fluorophore used to label the liposome bilayer is illuminated under low power (9.8 mW), and would not provide a usable signal. Ideally, all experiments would use a neutral density filter larger than the one used here for comparison to achieve a bleaching rate less than a percent over multiple exposures; however, this was not possible.

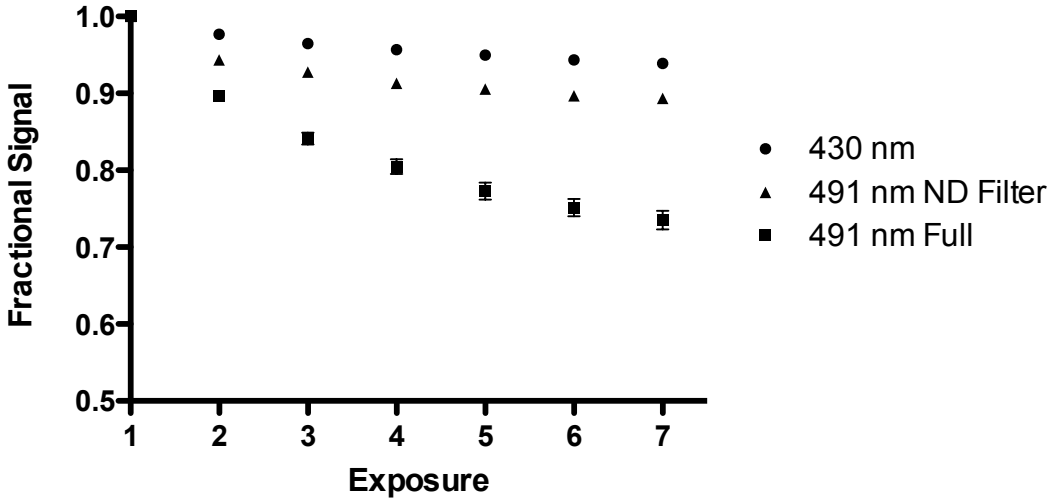

Figure 2.9 Photobleaching of FITC-dextran.
The effect of photobleaching was determined over 7 successive exposures. The average data (+/- S.E.M.) for between 17 and 36 labeled endosomes from 8 separate fields is shown. The bleaching rates for the 430 nm channel (●) and 491 nm channel (■) under full illumination are shown, along with the 491 nm channel (▲) in the presence of a neutral density filter.

The accuracy of the pH measurements determined experimentally using FITC-dextran was reinforced by colocalization with Lysosensor Blue DND-167 (Figure 2.10). Lysosensor has a pKa of 5.1, above which it is non-fluorescent. Thus, compartments that are co-labeled with FITC-dextran and Lysosensor should not have a FITC-dextran measured pH above 5.1 Indeed, compartments with a pH higher than 5.1 did not colocalize with Lysosensor. This further supports the accuracy of pH measurements using FITC-dextran and provides an external validation of the pH measurements.

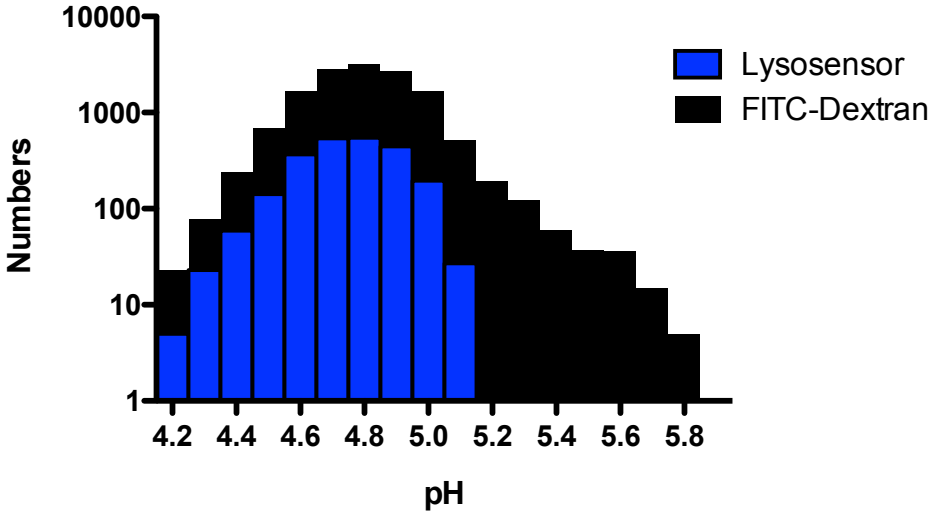

Figure 2.10 Colocalization of Lysosensor Blue DND-167 with FITC-dextran.
Shown are the histograms of late endosomes and lysosomes labeled with FITC-dextran. On the X-axis is the pH from 4.2 to 5.8, and the Y-axis is the number of endosomes on $\log_{10}$ scale. The pH of endosomes labeled with FITC-dextran were determined generating the histogram in black. Restriction of the histogram to endosomes than are also colabeled with Lysosensor Blue are shown in blue. Lysosensor is present in only 1 endosome above pH 5.1 (0.04% of all events) compared to 469 endosomes in the parent FITC-dextran population (4.0%).

2.3.5 Image Processing

In general there are two computational methods for colocalization analysis: pixel based and shape based (Bolte and Cordelières, 2006). Fluorescently labeled endosomes and liposomes imaged with an electron multiplying charge coupled device (EMCCD) camera can be described by a circular area measurement when performing colocalization analysis. However, a more complete and thorough description is the Gaussian function. The Gaussian function is particularly powerful at determining the location of particles when the particle is smaller than the wavelength of emitting light (Cheezum et al., 2001), although it is recognized that movement has significant effects on positional accuracy (Deschout et al., 2012). Elliptical Gaussian fitting outperforms circular Gaussian fitting when particles are in motion, and provides a more detailed

description of the particles in this study (liposomes and endosomes) than a centroid-based method (Deschout et al., 2012). Consequently, colocalization analysis was performed by first fitting every spot in each image to a 2D ellipsoid Gaussian function:

$$f(x,y) = Ae^{\left(-\frac{a(x-xc)^2+2b(x-xc)(y-yx)+c(y-yc)^2}{2}\right)} + B \quad \textbf{(Equation 2)}$$

where A is intensity, B is background, xc and yc are x and y center coordinates respectively. The parameters a, b, and c can further be defined as:

$$a = \frac{\cos^2\theta}{2\sigma_x^2} + \frac{\sin^2\theta}{2\sigma_y^2} \quad \textbf{(Equation 3)}$$

$$b = -\frac{\sin 2\theta}{4\sigma_x^2} + \frac{\sin 2\theta}{4\sigma_y^2} \quad \textbf{(Equation 4)}$$

$$c = \frac{\sin^2\theta}{2\sigma_x^2} + \frac{\cos^2\theta}{2\sigma_y^2} \quad \textbf{(Equation 5)}$$

where σ_x and σ_y are the variance in x and y, and θ is the rotation angle. From Gaussian fitting there are 11 parameters extracted: Volume, Intensity, Background, X, Y, Width, Asymmetry (σ_x/σ_y), σ_x, σ_y, θ, and Error (estimate based upon the Intensity, Background, and Width from (Thompson et al., 2008)).

Gaussian fits that were below an intensity threshold determined per image were not counted. The threshold was determined by sampling the image with a 5 pixel^2 box and determining the average pixel intensity. This process was iterated until a minima was found that did not deviate by 0.1%. The minima per image were then multiplied by 10, which was set as the threshold for eliminating Gaussian fits. For the liposome lipid bilayer labeled with DiD, the excitation at 640 nm was found to have virtually no background and as a consequence the minima was multiplied by 5 to set the threshold for Gaussian fits in that channel. Other parameters that resulted in

Gaussian fit elimination were proximity to the edges of the image greater than 15 pixels, poor Gaussian fits with error values greater than 0.1, and calculated Gaussian intensities that were higher than the intensity of the deconvolved image at the peak pixel.

After Gaussian fitting, all spots were coarse colocalized by pairwise linear distance minimization (Figure 2.11A). After a distance minima was identified, the spot with the larger radius was used to determine if the other spot fit within it. Spots were compared pairwise between channels to find colocalization (Figure 2.11B). Colocalization was first found between the siRNA-TEX615 and DiD channels. Then the matches were used to find colocalization with endosomal markers (3-channel) or the pH-insensitive FITC-dextran channel (4-channel). Finally, matches were found in the pH-sensitive FITC-dextran channel (4-channel).

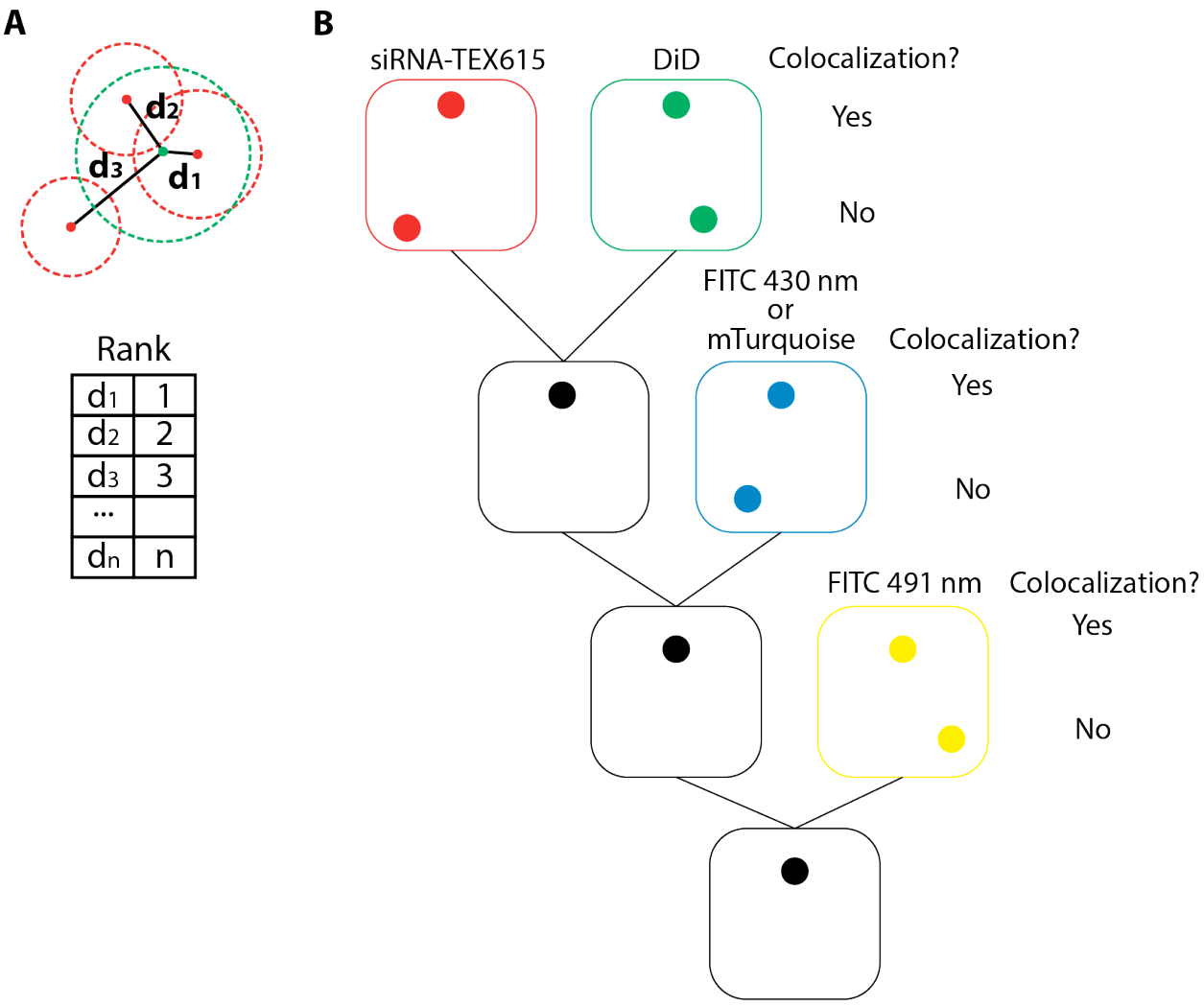

Figure 2.11 Image colocalization analysis flow diagram.
A) Distances between spots in different channels are ranked by their linear distance measurements (d1, d2, d3, etc). The spot with the minimal distance (d1) is then confirmed to colocalize by making sure it is within the radius of the parent spot (green). B) Flow diagram for colocalization analysis.

An image was compared to itself following single pixel displacements along the x coordinate, to validate the colocalization analysis performed (Figure 2.12). Deconvolved images were subjected to Gaussian fitting, which produced the starting non-displaced image (Figure 2.12B). In all images, at least 90% of spots determined by eye in the deconvolved image were found using the Gaussian fitting algorithm. 100% of spots found after Gaussian fitting colocalized to a non-displaced duplicate image (Figure 2.12E). After a single pixel displacement 41.5% +/-

3.39% (S.E.M.) of particles still colocalized, which dropped to 3.97% +/- 1.87 (S.E.M.) after a displacement of 2 pixels, and 0% after 5 pixels (Figure 2.12E). These data demonstrate that the Gaussian fitting algorithm and colocalization analysis are robust and have a ~ 4% false positive rate at 2 pixels.

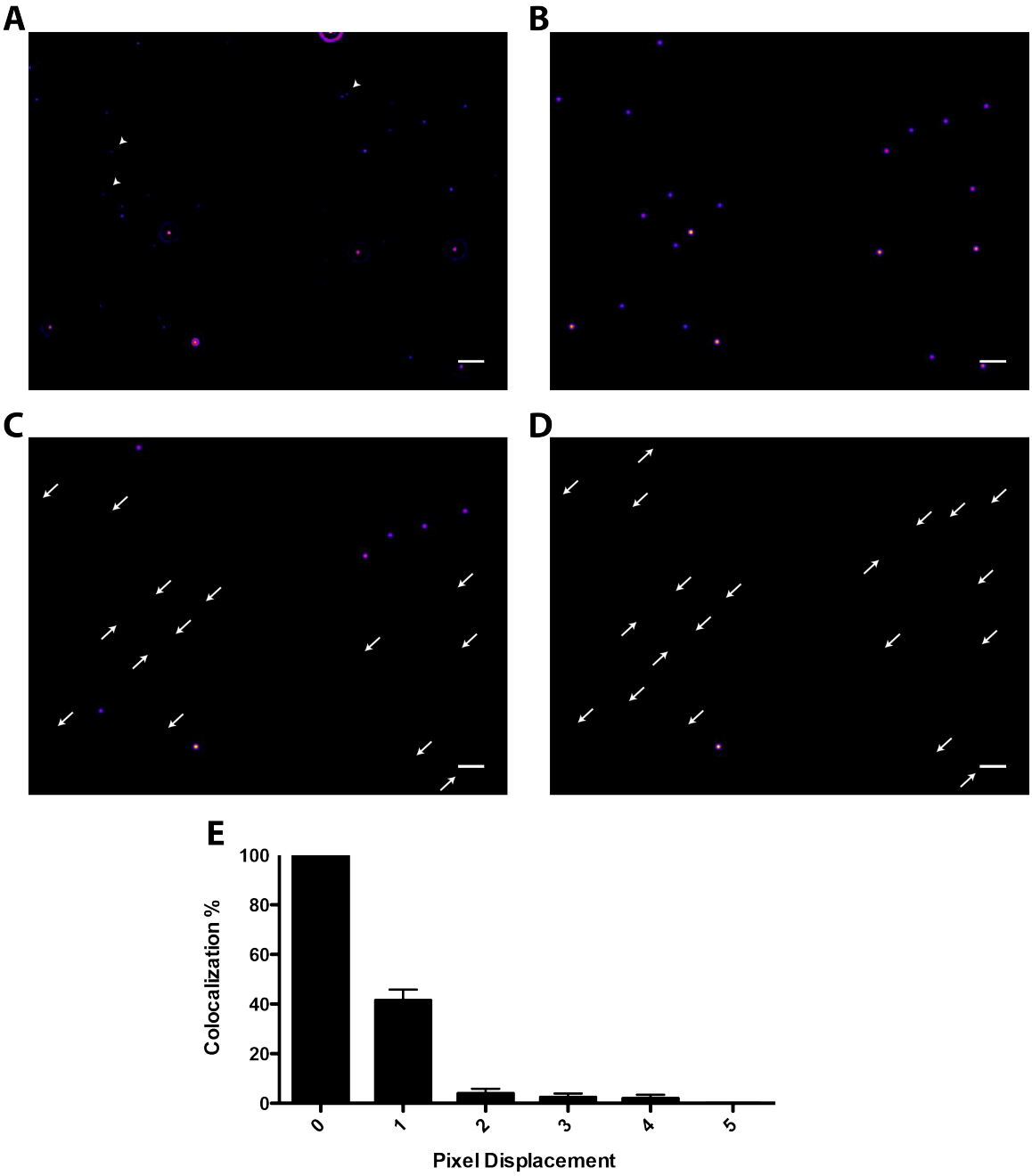

Figure 2.12 Image colocalization analysis.

Images were duplicated and displaced between 1 and 5 pixels and colocalized with the non-displaced image. A) A representative deconvolved image. Arrow heads indicate spots that are not detected by Gaussian fitting (total spots by eye = 24). B) Reconstruction of the Gaussian fit of the image in (A) following colocalization to itself. n = 21 spots were both fit and colocalized. C-D) Reconstruction of the colocalized particles after 1 (C) or 2 pixel (D) displacement. Arrows highlight particles that do not colocalize. E) Percent colocalization as a function of pixel displacement (n = 214, 10 fields). Without pixel displacement 100% of particles are colocalized in all fields. With 5 pixel displacement 0% of particles are colocalized in all fields. Averages +/- S.E.M. are shown. Scale bars in images A-D are 5 µm.

Sample colocalization analysis is shown in Figure 2.13 and Figure 2.14 for a pH measurement experiment with DOTAP:DOPE liposomes and the parameters of the colocalized spots are shown in Table 2.3. The image deconvolution and background subtraction removes much of the out of focus light (Figure 2.13). The Gaussian fitting algorithm accurately finds spots in the deconvolved images and produces x and y coordinate centers, as well as, width and intensity measurements (Figure 2.14). The extracted pH measurements are all within the expected range of early endosomes, which is to be expected as this image set is within 5 minutes after the pulse of liposomes and FITC-dextran. The results are typical of the image processing and Gaussian fitting that is done in the remainder of the experiments with pH measurements and endosomal markers.

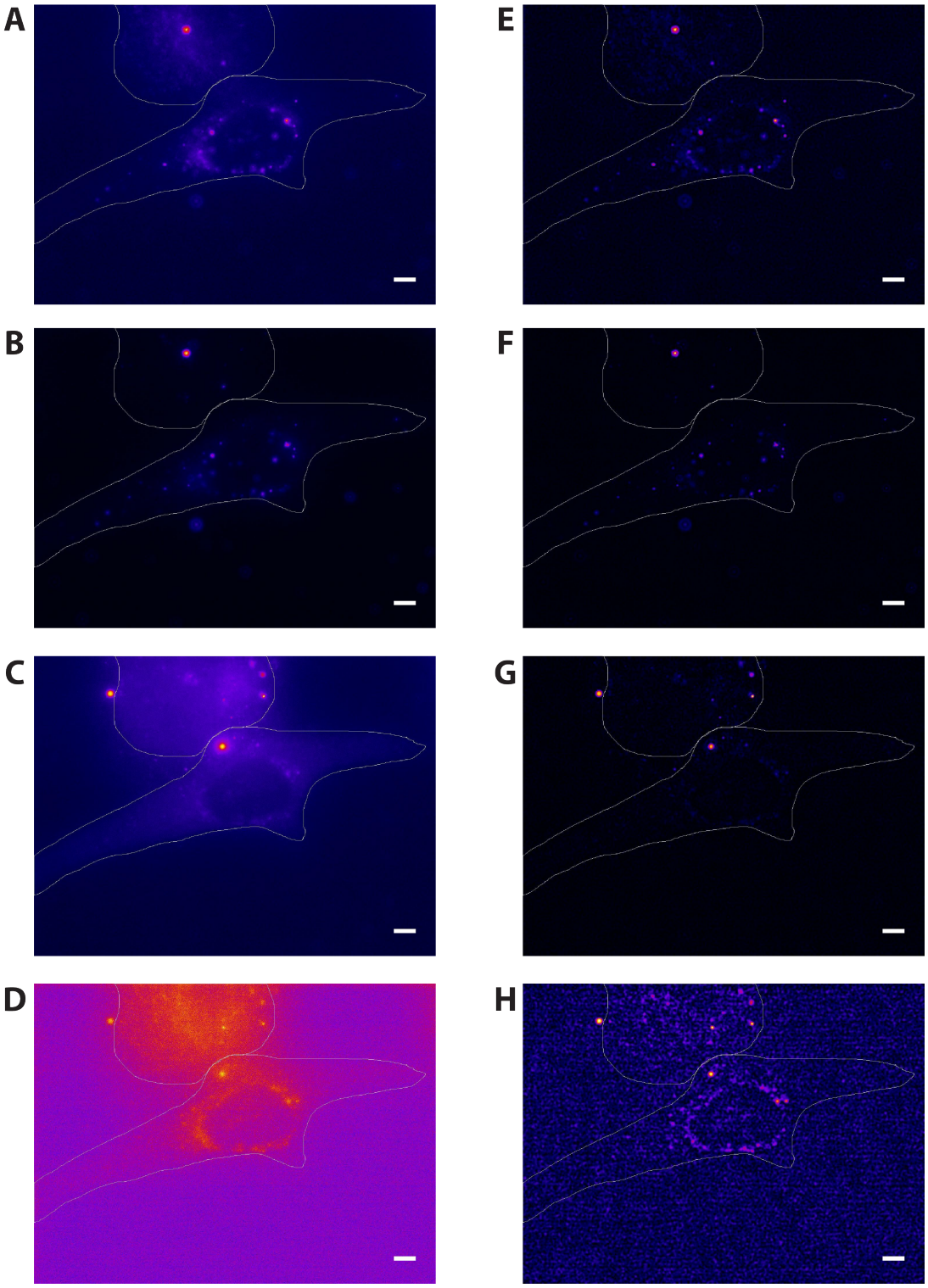

Figure 2.13 Image deconvolution.
The 4 channels collected are siRNA-TEX615 (A,E), DiD (B,F), FITC-Dextran 491 nm (C, G), and FITC-Dextran 430 nm (D, H). The images on the left are the raw image (A-D) and on the right are post-deconvolution and background subtraction (E-H). Cell body outlines are drawn from a phase contrast image and the scale bars are 5 µm.

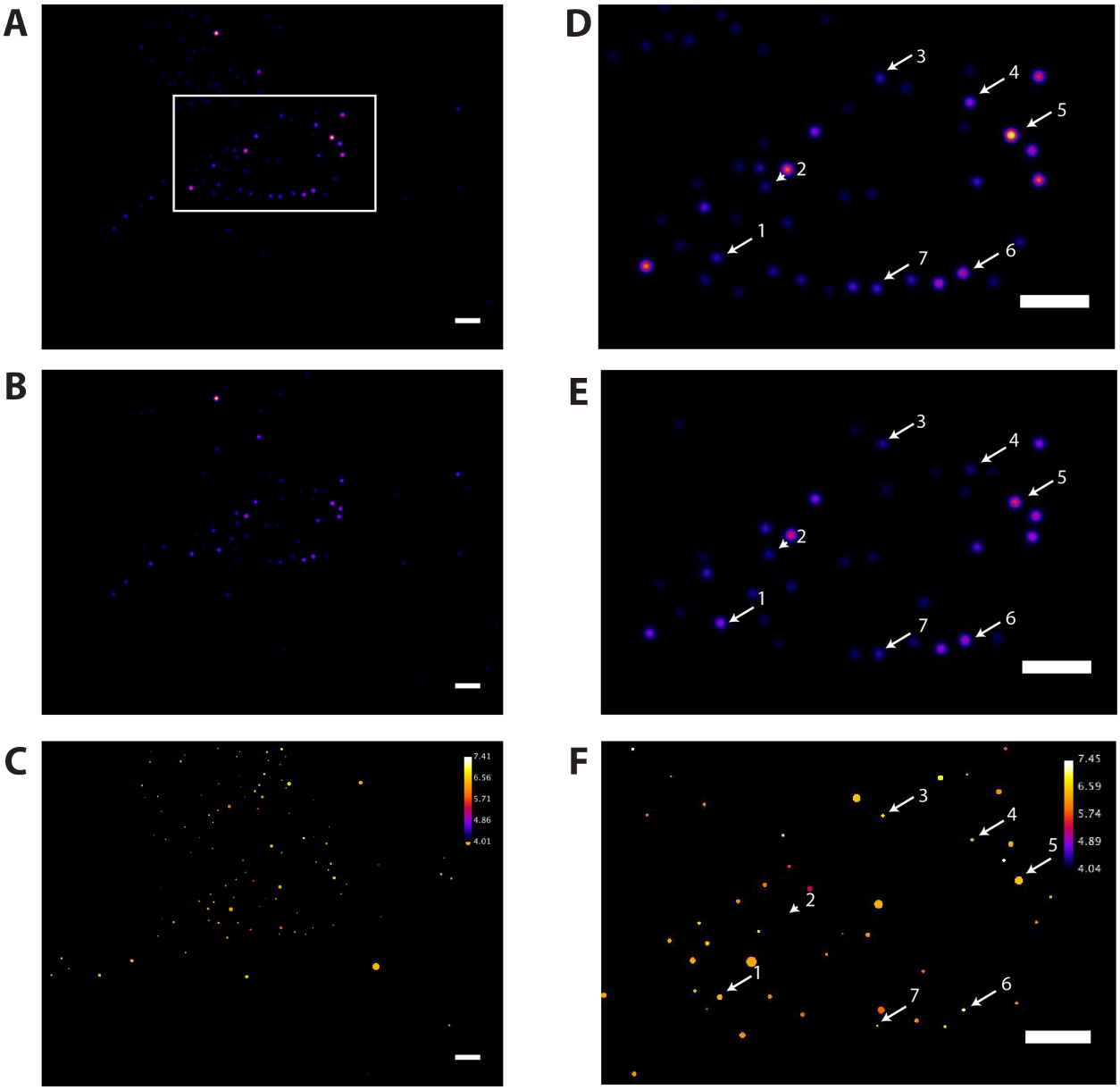

Figure 2.14 Gaussian fitting and example colocalization and pH measurement with FITC-dextran.

The results from Gaussian fitting and matching of the whole image are shown in A-C. The channels are siRNA-TEX615 (A, D), DiD (B, E), and pH (C, F). Cropped images corresponding to the region indicated by the white box in (A) are shown in D-F. There are 6 liposomes that are indicated by arrows that colocalize with a pH-measurable compartment (Particles 1, and 3-7). There is 1 liposome that is indicated by the arrowhead, which fails to colocalize with a pH-measurable compartment. The measurements of each of the 7 liposomes are given in Table 2.3. The scale bars are 5 µm.

Number	siRNA (Log_{10} Fluorescence A.U.)	Lipid (Log_{10} Fluorescence A.U.)	siRNA/Lipid	pH
1	2.53	3.62	0.70	6.42
2	2.47	2.90	0.85	ND
3	2.77	3.20	0.87	6.86
4	3.33	4.19	0.80	6.55
5	2.84	2.83	1.00	6.52
6	3.30	3.61	0.92	7.08
7	2.70	3.24	0.83	6.32

Table 2.3 Properties of liposomes shown in Figure 2.14.
In the images in Figure 2.14 D-F, there are 7 liposomes that are highlighted. This table contains the measurements from the siRNA, lipid, and pH channels for each liposome.

2.4 Conclusion

Nine mTurquoise fusions to endosomal markers were created to be as identical as possible to published constructs. HeLa cells were then transduced to create stable cell lines of each marker. The expression levels of the markers and growth properties of the cell lines were characterized. Each marker was determined to be optimally expressed between 5 and 10 µg/mL doxycycline with no adverse effects on growth rates and cellular morphology. Each marker was assumed to localize correctly under the conditions used.

The pH calibration of FITC-dextran *in situ* is consistent with what has been observed previously and similar to the intrinsic parameters of FITC (Figure 2.7A). After attenuation of lamp power, photobleaching was reduced, and the calibration curve did not significantly change from that determined under full lamp illumination. In addition, the distribution of ratios demonstrate that the calibration curve has significant power to accurately determine the pH of endosomal compartments.

Photobleaching was determined to be ~ 10% and ~ 2% in the 491 and 430 nm channel, respectively, following a single exposure. Since the bleaching rate is high in the conditions used

and could not be avoided due to hardware limitations, only data from the first exposure is used for all experimental determinations of pH using FITC-dextran.

The accuracy of pH measured with FITC-dextran was examined by determining the extent of colocalization with Lysosensor Blue DND-167 (Figure 2.10). The concordance between the lack of colocalization between FITC-dextran and Lysosensor Blue DND-167 above the pH of 5.1 suggests that the pH measurements are accurate in a single exposure despite photobleaching.

The workflow created to process the images and perform Gaussian fitting all relied upon written Java code and plugins for Fiji/ImageJ. The only modification was to the Gaussian fitting program to eliminate poor Gaussian fits in my data set and move the plugin to ImageJ from MicroManager. The newly written colocalization code, simply found Gaussian fits between channels that overlapped due to the particle coordinates and width. It also accurately identified spots that colocalize in all channels, while eliminating spots that do not colocalize with an error rate of ~ 4% at 2 pixels.

2.5 References

Bolte, S., and Cordelières, F.P. (2006). A guided tour into subcellular colocalization analysis in light microscopy. J Microsc *224*, 213–232.

Bucci, C., Thomsen, P., Nicoziani, P., McCarthy, J., and van Deurs, B. (2000). Rab7: a key to lysosome biogenesis. Mol Biol Cell *11*, 467–480.

Chan, K.W., Csanády, L., Seto-Young, D., Nairn, A.C., and Gadsby, D.C. (2000). Severed molecules functionally define the boundaries of the cystic fibrosis transmembrane conductance regulator's NH(2)-terminal nucleotide binding domain. J Gen Physiol *116*, 163–180.

Chavrier, P., Gorvel, J.P., Stelzer, E., Simons, K., Gruenberg, J., and Zerial, M. (1991). Hypervariable C-terminal domain of rab proteins acts as a targeting signal. Nature *353*, 769–772.

Cheezum, M.K., Walker, W.F., and Guilford, W.H. (2001). Quantitative comparison of algorithms for tracking single fluorescent particles. Biophys J *81*, 2378–2388.

Chen, J.W., Cha, Y., Yuksel, K.U., Gracy, R.W., and August, J.T. (1988). Isolation and sequencing of a cDNA clone encoding lysosomal membrane glycoprotein mouse LAMP-1. Sequence similarity to proteins bearing onco-differentiation antigens. J Biol Chem *263*, 8754–8758.

Deschout, H., Neyts, K., and Braeckmans, K. (2012). The influence of movement on the localization precision of sub-resolution particles in fluorescence microscopy. J Biophotonics *5*, 97–109.

Doherty, G.J., and McMahon, H.T. (2009). Mechanisms of endocytosis. Annu. Rev. Biochem. *78*, 857–902.

Escola, J.M., Kleijmeer, M.J., Stoorvogel, W., Griffith, J.M., Yoshie, O., and Geuze, H.J. (1998). Selective enrichment of tetraspan proteins on the internal vesicles of multivesicular endosomes and on exosomes secreted by human B-lymphocytes. J Biol Chem *273*, 20121–20127.

Falcón-Pérez, J.M., Nazarian, R., Sabatti, C., and Dell'Angelica, E.C. (2005). Distribution and dynamics of Lamp1-containing endocytic organelles in fibroblasts deficient in BLOC-3. J Cell Sci *118*, 5243–5255.

Frick, M., Bright, N.A., Riento, K., Bray, A., Merrified, C., and Nichols, B.J. (2007). Coassembly of flotillins induces formation of membrane microdomains, membrane curvature, and vesicle budding. Curr Biol *17*, 1151–1156.

Gaidarov, I., Santini, F., Warren, R.A., and Keen, J.H. (1999). Spatial control of coated-pit dynamics in living cells. Nat Cell Biol *1*, 1–7.

Geisow, M.J. (1984). Fluorescein conjugates as indicators of subcellular pH. A critical evaluation. Exp Cell Res *150*, 29–35.

Glebov, O.O., Bright, N.A., and Nichols, B.J. (2006). Flotillin-1 defines a clathrin-independent endocytic pathway in mammalian cells. Nat Cell Biol *8*, 46–54.

Haggie, P.M., and Verkman, A.S. (2007). Cystic fibrosis transmembrane conductance regulator-independent phagosomal acidification in macrophages. J Biol Chem *282*, 31422–31428.

Haggie, P.M., and Verkman, A.S. (2009). Defective organellar acidification as a cause of cystic fibrosis lung disease: reexamination of a recurring hypothesis. Am J Physiol Lung Cell Mol Physiol *296*, L859–L867.

Lanz, E., Gregor, M., Slavík, J., and Kotyk, A. (1997). Use of FITC as a fluorescent probe for intracellular pH measurement. Journal of Fluorescence *7*, 317–319.

Mukherjee, S., Ghosh, R.N., and Maxfield, F.R. (1997). Endocytosis. Physiol Rev *77*, 759–803.

O'Connor, N., and Silver, R.B. (2007). Ratio imaging: practical considerations for measuring intracellular Ca2+ and pH in living cells. Methods Cell Biol *81*, 415–433.

Pelkmans, L., Kartenbeck, J., and Helenius, A. (2001). Caveolar endocytosis of simian virus 40 reveals a new two-step vesicular-transport pathway to the ER. Nat Cell Biol *3*, 473–483.

Rappoport, J.Z., and Simon, S.M. (2008). A functional GFP fusion for imaging clathrin-mediated endocytosis. Traffic *9*, 1250–1255.

Roth, M.G. (2006). Clathrin-mediated endocytosis before fluorescent proteins. Nat Rev Mol Cell Biol *7*, 63–68.

Santamaría, A., Castellanos, E., Gómez, V., Benedit, P., Renau-Piqueras, J., Morote, J., Reventós, J., Thomson, T.M., and Paciucci, R. (2005). PTOV1 enables the nuclear translocation and mitogenic activity of flotillin-1, a major protein of lipid rafts. Mol Cell Biol *25*, 1900–1911.

Sherer, N.M., Lehmann, M.J., Jimenez-Soto, L.F., Ingmundson, A., Horner, S.M., Cicchetti, G., Allen, P.G., Pypaert, M., Cunningham, J.M., and Mothes, W. (2003). Visualization of retroviral replication in living cells reveals budding into multivesicular bodies. Traffic *4*, 785–801.

Sönnichsen, B., de Renzis, S., Nielsen, E., Rietdorf, J., and Zerial, M. (2000). Distinct membrane domains on endosomes in the recycling pathway visualized by multicolor imaging of Rab4, Rab5, and Rab11. J Cell Biol *149*, 901–914.

Stenmark, H., and Olkkonen, V.M. (2001). The Rab GTPase family. Genome Biol *2*, REVIEWS3007.

Thompson, R.E., Larson, D.R., and Webb, W.W. (2008). Precise Nanometer Localization Analysis for Individual Fluorescent Probes. Biophys J *82*, 2775–2783.

Chapter 3 : pH and Endosomal Colocalization Analysis of Liposomal Formulations

3.1 Introduction

High-resolution single particle tracking (SPT) has been used to study endocytosis of a wide variety of cargo (Braeckmans et al., 2010b; Brandenburg and Zhuang, 2007; Lai and Hanes, 2008; Payne, 2007; Ruthardt et al., 2011; Suh et al., 2005). For instance, virologists have used SPT to uncover the mechanisms by which viruses infect cells. SPT demonstrated that HIV-1 enters and productively infects cells using the endosomal route as opposed to direct fusion at the plasma membrane (Miyauchi et al., 2009). The infection mechanisms and pathways of influenza A, dengue, HCV, and SV40 have also been elucidated by SPT (Avilov et al., 2012; Coller et al., 2009; Liu et al., 2011; Pelkmans et al., 2001; Rust et al., 2004; van der Schaar et al., 2008). In the materials research area, SPT was used to demonstrate that Tat modified quantum dots induced heparan sulfate proteoglycan cross-linking and activated Rac1 resulting in internalization (Imamura et al., 2011). Polymers for nucleic acid delivery including, PAMAM dendrimers, were tracked in cells to determine which pathways of internalization are used and how the polymer is trafficked after internalization (Vercauteren et al., 2011). PEI, polylysine, dextran, and polyfluorene polymers have also been studied by SPT (de Bruin et al., 2008; 2007; Humphries et al., 2011; Jin et al., 2009; Kim et al., 2011; Mickler et al., 2012; Suk et al., 2007; Yu et al., 2009). Finally, cellular internalization of exosomes has been investigated using SPT (Tian et al., 2010; 2012). These papers highlight the power of SPT to understand the complex response cells have to foreign particles and justify my use of the technique to follow liposomes inside cells.

There have been several studies of liposomal systems using SPT (Akita et al., 2010; 2012; Berezhna et al., 2005; Braeckmans et al., 2010a; Chithrani et al., 2010; Rehman et al., 2013; Sauer et al., 2009). The Harashima group demonstrated that octa-arganine (R8) modified liposomes have slower intracellular directional transport compared to adenovirus or endosomes lacking R8 liposomes (Akita et al., 2010). Further modification of these liposomes with a peptide derived from African swine fever virus that binds to dynein light chain resulted in directed movement and accumulation at the microtubule organizing center while R8 liposomes lacking the peptide poorly diffused in the cytoplasm (Akita et al., 2012). These data suggest that either something inherent to the liposome slows down endocytosis or the cell senses and responds differentially to liposomes compared to viruses. Lipoplexes were observed to gradually release contents, while polyplexes rapidly and catastrophically released their contents, supporting the proton sponge effect (Behr, 1997; Rehman et al., 2013; Sonawane et al., 2003). Specialized liposomes with lipid-gold conjugates or magnetic properties have been analyzed by SPT to demonstrate cellular internalization and transport (Chithrani et al., 2010; Sauer et al., 2009). Lastly, SPT has been used to size DOTAP:DOPE liposomes in serum or whole blood *in vitro* and to investigate the decomplexation of DNA using model membranes (Berezhna et al., 2005; Braeckmans et al., 2010a).

As discussed in Chapter 1, endocytosis is intimately involved with liposomal delivery of siRNA. Following cellular entry by endocytosis, the hypothesized mechanism of cytosolic nucleic acids delivery by liposomal vectors is a three step process (Farhood et al., 1995; Hafez et al., 2001; Koltover et al., 1998; Legendre and Szoka, 1992; Xu and Szoka, 1996; Zelphati and Szoka, 1996a; Zuhorn et al., 2005). In the first step, liposomal vector lipids induce a bilayer phase

conversion from a bilayer lamellar, L_α, to inverted hexagonal, H_{II}, phase. The phase inversion causes bilayer destabilization resulting in flipping of anionic membrane lipids from the cytoplasmic leaflet of endosomes to the limiting membrane. Second, anionic lipids diffuse into the liposomal membrane neutralizing the charge complexation between anionic siRNA and cationic lipids. Finally, the siRNA is able to freely diffuse into the cytoplasm of the cell.

In the formulations tested here: CHEMS:DOPE, DOTAP:DOPE, and DLinDMA, each lipid plays an important role in mediating an aspect of the delivery mechanism (Figure 3.1). DOPE and DLinDMA both prefer the inverted hexagonal phase and promote bilayer destabilization. DLinDMA is also cationic below its pKa of 6.8 (Semple et al., 2010), while DOTAP is always cationic. CHEMS stabilizes DOPE membranes until its carboxylate is protonated at pH 5.5 (Ellens et al., 1984; Lai et al., 1985; Legendre and Szoka, 1992). The mechanism of delivery was based upon observations using a DOTAP:DOPE model formulation (Zelphati and Szoka, 1996a), however, the other two formulations have slightly nuanced changes to the general mechanism described above. DLinDMA largely follows the same paradigm except that its cationic charge increases during endocytosis. The CHEMS:DOPE formulation induces membrane destabilization by inducing H_{II} phase, but the charge neutralization step to separate siRNA from the complex is not required as the formulation is already lightly anionic (Ellens et al., 1984; Lai et al., 1985). Unlike the cationic formulations, which can mediate close apposition of the liposomal and endosomal bilayers through electrostatic interactions, the CHEMS:DOPE formulation requires close contact mediated by diffusion or entrapment.

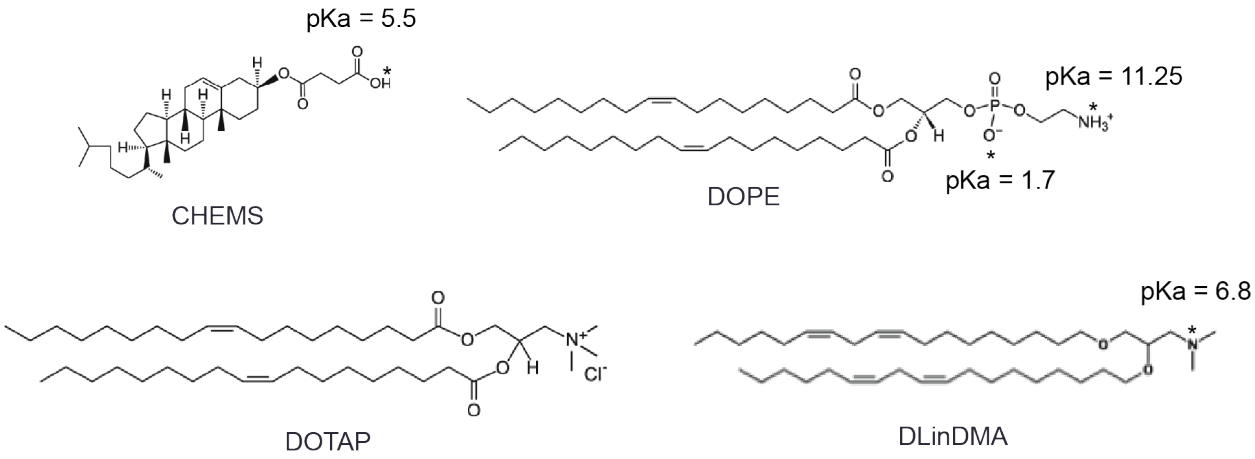

Figure 3.1 Lipid structures used in this study.
The exact formulations are given in the methods section. These four lipids are the primary components of the formulations tested. The pKas of the protonatable groups indicated by (*) are given.

In this chapter the three formulations described above have been tracked by SPT as they are endocytosed. The intra-endosomal pH that the formulations experience has been monitored to determine where the liposomes reside and if endosomal pH correlates with contents release. In addition, the liposomes have been colocalized with endosomal markers described in Chapter 2 to determine if formulation alters the cellular internalization route. From these analyses, I conclude that the formulations tested are sorted by cells through distinct cellular compartments, and there is a correlation between efficient siRNA delivery and increased colocalization with recycling endosomes and/or multivesicular bodies.

3.2 Methods

3.2.1 Cell Culture

HEK293T, HeLa and all HeLa derivatives were maintained in T75 flasks between 10-90% confluence (100% confluent T75 yields ~10 x 10^6 total cells) in RPMI 1640 supplemented with 10% heat inactivated FBS (Gibco, Life Technologies, Benicia, CA) and 25 mM HEPES in a

humidified atmosphere with 5% CO_2 at 37 ^oC.

For microscopy studies, HeLa and HeLa derivative cells were cultured in RPMI 1640 supplemented with 10% defined FBS (HyClone, Thermo Fisher, Waltham, MA) and 25 mM HEPES. 48 hours prior to microscopy, cells were trypsinized and plated at 300,000 cells per 35 mm uncoated glass coverslip bottom FluoroDish (World Precision Instruments, Sarasota, FL). The media was changed 24 hours later and if induction was used, 10 μg/mL doxycycline was added to induce marker-mTurquoise expression. On the day of imaging, the plate was 90% confluent at ~1,200,000 cells per dish. During imaging experiments, the cells were maintained in PBS supplemented with 6 mM glucose and 1.1 mM pyruvate (PBSgp).

3.2.2 Materials

All cell culture reagents were supplied by the UCSF Cell Culture Facility. 1,2-dioleoyl-3-trimethylammonium-propane (DOTAP), 1,2-dioleoyl-sn-glycero-3-phosphoethanolamine (DOPE), 1,2-dipalmitoyl-sn-glycero-3-phosphocholine (DPPC), 1,2-distearoyl-sn-glycero-3-phosphoethanolamine-N-[amino(polyethylene glycol)-2000] (PEG-DSPE), cholesterol (Chol), and cholesteryl hemisuccinate (CHEMS) were obtained from Avanti Polar Lipids (Alabaster, AL). 1,2-dimyristoyl-sn-glycerol-[methoxy(polyethylene glycol)-2000 (PEG-DMG) was obtained from NOF-Corporation (Tokyo, Japan). DLinDMA was provided by Pfizer (Cambridge, MA). Luciferase sense and antisense TEX615 labeled RNA 5'-rGrCrUrArCrArUrUrCrUrGrGrArGrArCrArUrATT/3TEX615/, and 5'-rCrGrArUrGrUrArArGrArCrCrUrCrUrGrUrArUTT/3TEX615/, respectively, were obtained from Integrated DNA Technologies (San Diego, CA). siRNA against luciferase and a scrambled

control for *in vitro* knockdown experiments was provided by Pfizer (Cambridge, MA). 1,1′-dioctadecyl-3,3,3′,3′-tetramethylindodicarbocyanine perchlorate (DiD), Fluorescein isothiocyanate (FITC), amino dextran (40 kDa), and Lysosensor Blue DND-167 were obtained from Molecular Probes (Eugene, OR). The Steady-Glo luciferase assay kit was purchased from Promega (Madison, WI).

3.2.3 Preparation of Liposomes

The formulations tested were as follows: DOTAP:DOPE:PEG-DMG:DiD (56:38:5:1 mole percent), CHEMS:DOPE:PEG-DMG:DiD (38:56:5:1 mole percent) and DLinDMA:DPPC:Cholesterol:PEG-DMG:DiD (40:14:40:5:1 mole percent). 1 μM of total lipid was dried down by rotary evaporation under reduced pressure in a glass test tube for 4 hours then dried overnight under high vacuum. The lipids were dissolved in 200 μL of methanol and rapidly injected into 300 μL of 50 mM citrate pH 4 aqueous buffer containing 35 micrograms of siRNA-TEX615 stirring at 300 rpm at 60 ^{o}C. The mixture was extruded (11x) through 100 nm pores in a polycarbonate membrane (Nucleopore, Whatman, Clifton, NJ), followed by rotary evaporation under reduced pressure to remove the methanol. Liposome preparations were then dialyzed overnight ~4000-fold against 5 mM HEPES, pH 7, 145 mM NaCl, 3.4 mM EDTA with 100 kDa MWCO membrane (Spectrum, New Brunswick, NJ). For studies on cellular binding and RNA knockdown, the formulations were prepared identically except that DiO replaced DiD. The particle size of the DiO labeled formulations was measured using a Malvern Zetasizer NanoZS (Westborough, MA).

For microscopy studies, liposomes were further purified by equilibrium density centrifugation in a linear, 0-18% sucrose gradient. The gradients were prepared by layering 2 mL of 15% sucrose

dissolved in PBS under 2 mL of PBS in Bekman Polyallomer ½ x 2 in. tubes, type 326819 (Beckman Coulter, Indianapolis, IN). The gradients were then spun for 30 revolutions at 45 ^{o} in a cell culture rotator. After mixing the two layers the tubes were frozen at -80 ^{o}C, and thawed at 4 ^{o}C before use. Liposome preparations were added and spun at 100,000 ×g for 16 hours at 4 ^{o}C in a Beckman SW-55Ti rotor (Beckman Coulter, Indianapolis, IN). A needle was used to poke a hole in the bottom of the centrifuge tube and fractions were collected and analyzed for DiD and TEX615 fluorescence. The fractions with the highest levels of fluorescence for both markers were used for microscopy studies. The liposome preparation was stored at -80 ^{o}C in 15% sucrose.

3.2.4 FACS Analysis of Cellular Binding

10,000 HeLa cells were added to each well of a 96-well plate 24 hours before the start of the experiment. For apparent K_d experiments, various concentrations of the liposome preparations were added to the cells in D-PBS and allowed to bind to the cells for 30 minutes at 37 ^{o}C. The cells were then analyzed by FACS. Data was fit by nonlinear regression in Prism to a one site specific binding model with a Hill slope ($Y=B_{max}*X^{h}/(K_d^{h} + X^{h})$). For the internalization rate experiments, each liposome formulation was added to the cells the observed binding K_d concentration in PBSgp and incubated for up to 24 hours. The cells were removed from the plate by incubation in D-PBS and EDTA for 30 minutes at room temperature, then incubated with trypan blue to quench extracellular fluorescence and analyzed by FACS. Data was fit by nonlinear regression in Prism to a one-site total binding model ($Y=B_{max}*X/(K_d+X) + NS*X +$ Background).

3.2.5 *In Vitro* Knockdown of Luciferase

24 hours prior to the start of the experiment, 8,000 HeLa-Luc cells were seeded into each well of a 96-well plate such that the cells were ~80% confluent during the transfection. Lipoplex containing either an anti-luciferase siRNA or a non-specific control were added to the cells and incubation proceeded for 5 hours at which time the media was exchanged and incubation proceeded for 24 hours until luciferase activity was measured. Luciferase expression was measured using the Steady-Glo assay kit (Promega, Madison, WI). Luminescence was measured using an Infinite m1000 Pro microplate reader (Tecan, San Jose, CA).

3.2.6 Microscopy and Image Analysis

Images were acquired on a Nikon Eclipse Ti-E inverted microscope equipped with an In Vivo Scientific temperature controlled chamber with humidification and CO_2 control, infrared autofocus, 100x 1.4 numerical aperture Plan Apo objective, Photometrics Coolsnap HQ2 CCD camera, and Sutter Lambda XL lamp. Filters used were 89000 Sedat Quad, 89021 GFP/mCherry, and 89002 Dual CFP/YFP (Chroma Technology, Bellows Falls, VT). Image acquisition was performed using NIS Elements software and image analysis was performed using NIH ImageJ. For ratiometric pH determination images were taken using the ET490/20x, ET525/36m and ET430/24x, ET535/30m filters of the Sedat Quad and Dual CFP/YFP sets, respectively, with 100 ms exposure. CFP fusions were imaged using the ET430/24x, ET470/24m filters of the Dual CFP/YFP set with a 100 ms exposure. DiD was imaged using the ET645/30x and ET705/72m filters of the Sedat Quad set with 500 ms exposure and 2x2 binning. TEX615 labeled siRNA was imaged using the ET572/35x and ET632/60m filters of the GFP/mCherry set with 500 ms exposure and 2x2 binning.

Image analysis was performed using freely available Fiji plugins and some were written in de novo. Images were first deconvolved using the Parallel Spectral Deconvolution plugin (Piotr Wendykier) using a point spread function generated by the Diffraction PSF 3D plugin (Bob Dougherty). Deconvolved images were then background subtracted and 3D Gaussians were fit to the image using a modified GaussianFit plugin (Nico Stuurman). The X and Y coordinates of each fitted Gaussian spot in each frame were then colocalized with spots in other channels. Colocalization was defined as the center point of one Gaussian spot fitting within the width of a Gaussian spot of another from another channel.

3.3 Results

3.3.1 Liposomal Formulations

The exact composition and preparation of the formulations used in this study are given in the methods section. Each formulation was between 60 - 90 nm (Table 3.1) and while this is a significant difference, cells appear to internalize particles between 50 - 100 nm similarly (Rejman et al., 2004). The zeta potential measurements are in agreement with published values (Ducat et al., 2011; Zelphati et al., 1998). Any observed differences in cellular internalization is likely to be dominated by the effect of surface structure, including charge, lipid head group, and opsonized proteins, rather than size.

Formulation	Size (nm) / PDI	Zeta (mV)
CHEMS:DOPE	67.1 / 0.21	-10.7
DOTAP:DOPE	89.4 / 0.13	15.1
DLinDMA	80.8 / 0.18	5.4

Table 3.1 Physical characteristics of the formulations used.
Average particle sizes and poly-dispersity indices (PDI) for each formulation are shown along with the zeta potentials, which measure surface charge.

The liposomes used for microscopy were additionally purified using sucrose density gradient centrifugation. This step removed liposomes that were devoid of siRNA contents signal and provide a more mono-dispersed preparation of liposomes. The sucrose gradient used was linear between 2 – 18% (Figure 3.2). Liposomes that contained siRNA sediment to between 6 – 10 % sucrose, while empty liposomes remained at the top above 1% sucrose.

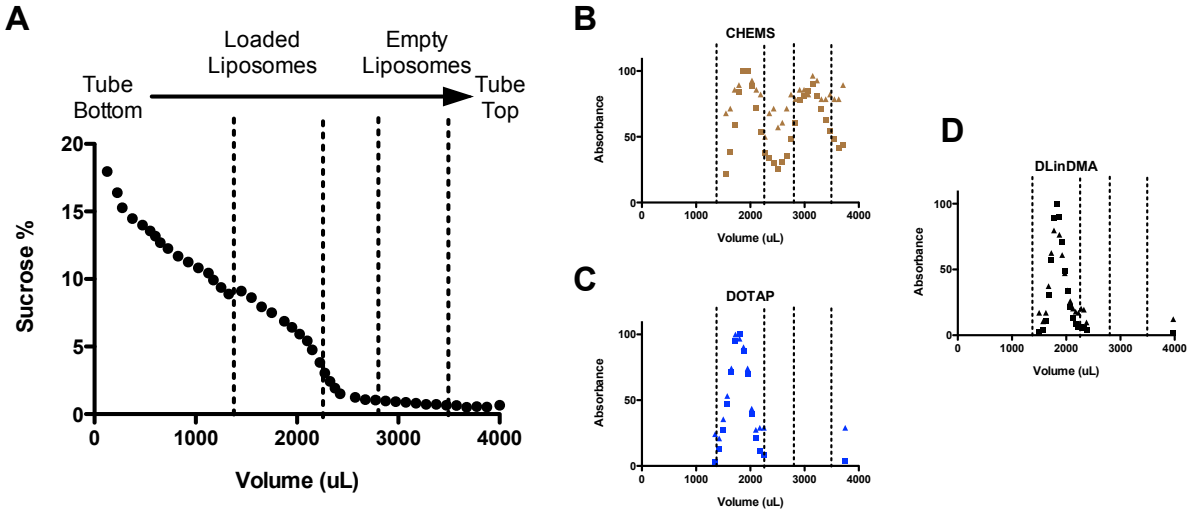

Figure 3.2 Sucrose gradient purification of liposomal siRNA preparations.
A) Liposomes were purified using linear sucrose gradients to separate siRNA loaded liposomes from empty liposomes. siRNA loaded liposomes sediment to between 6 – 10 % sucrose, while empty liposomes floated on top of the gradient at less than 2 % sucrose. B - D) Purification of liposomes with the normalized lipid absorbance (■) and normalized siRNA absorbance (▲) for each formulation CHEMS (B), DOTAP (C), and DLinDMA (D).

3.3.2 siRNA Knockdown of Luciferase Expression

The ability of each formulation to deliver siRNA was tested in vitro. An siRNA against luciferase and a scrambled control was formulated as described in the methods section. The complexes were added to 8,000 HeLa-Luc cells for 24 hours and the level of luciferase activity was determined (Figure 3.3). The DOTAP formulation displayed the best knockdown in vitro with an IC_{50} of 1.30 nM +/- 0.33. When ApoE is added exogenously the ability of DLinDMA to deliver siRNA is improved, although an exact IC_{50} value cannot be calculated precisely.

DLinDMA, in the absence of ApoE, and CHEMS have similar IC_{50} values around 70 nM. All formulations are capable of delivering siRNA to cells, but DOTAP demonstrates a superior ability than the other formulations. In addition, the presence of ApoE results in an enhancement of DLinDMA activity at low siRNA concentrations that is in contrast to the similar extent of internalization independent of ApoE addition.

In comparing these results to the imaging experiments, the relative potencies of the formulations and not the absolute concordance between the experiments are to be taken into account. The knockdown experiments were performed by incubation of cells with liposomes for a similar time scale (4 hours), but the kinetics of luciferase expression require 24 hours of incubation for RNAi to measurably knockdown protein levels. Thus the 24-hour time point measured for luciferase activity is a consequence of liposome endocytosis during the 4 hour incubation. In addition the dose required to knockdown luciferase expression is much higher (10 – 100-fold) than what is used for imaging experiments.

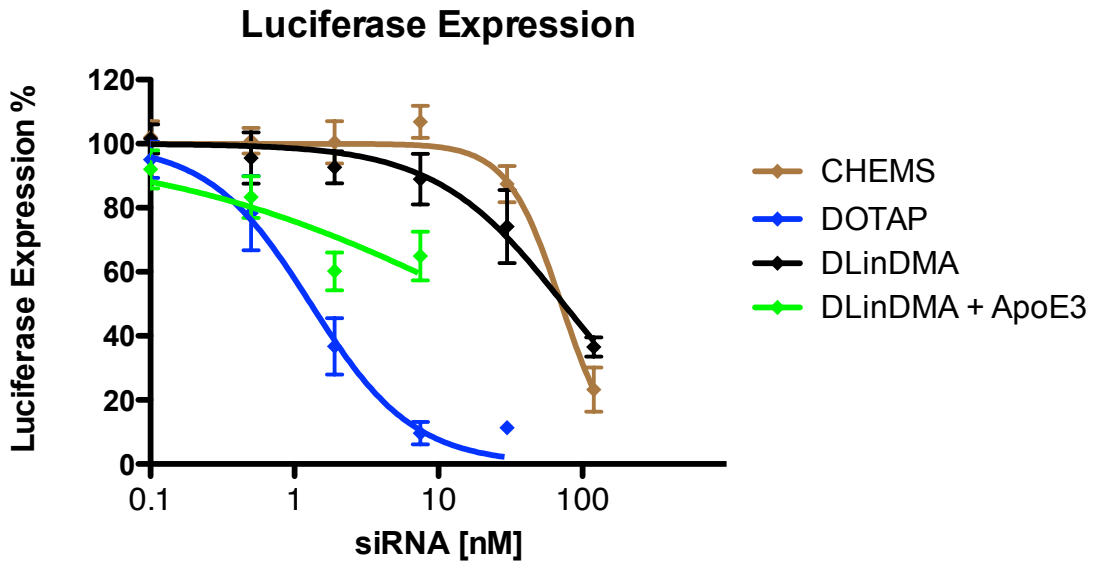

Figure 3.3 *In vitro* luciferase knockdown assay.
Complexes were added to cells for 4 hours and assayed for luciferase activity 24 hours later. Data are average +/- S.D. and fitted by non-linear regression to log(inhibitor) vs normalized response with a variable slope in Prism.

3.3.3 Binding and Internalization of Liposomal Formulations

The apparent K_d of each formulation was first determined by FACS to scale the concentrations used in the microscopy experiments (Figure 3.4). Since microscope experiments are performed in the absence of serum (PBSgp), the apparent K_d for each formulation was also determined under the same conditions but at 4 ^oC to prevent internalization. As expected, the apparent K_d of the formulations follows the zeta potential of each formulation, with the strength of binding determined by cationic charge (Table 3.2). These results indicated that DOTAP binds about 2 times better than the DLinDMA formulations and about 5 times better than the CHEMS formulation. For imaging studies, DOTAP was empirically titrated to 0.2 nM to result in ~ 10 liposomes per cell after incubation for 30 minutes at 37 ^oC. The 0.2 nM concentration for DOTAP was scaled by 2 or 5 for DLinDMA and CHEMS, respectively, and produced a similar number of liposomes per cell.

Interestingly, the addition of 1 µg/mL exogenous ApoE during incubation with the DLinDMA formulation does not alter the apparent binding K_d, while it is known that ApoE is required for efficient siRNA-mediated knockdown *in vivo* and *in vitro* (Akinc et al., 2010), and that HeLa cells express the low density lipoprotein receptor (LDLR) through which ApoE binds and internalizes. These data suggest that the effect of ApoE in enhancing delivery by DLinDMA is during or after cellular internalization.

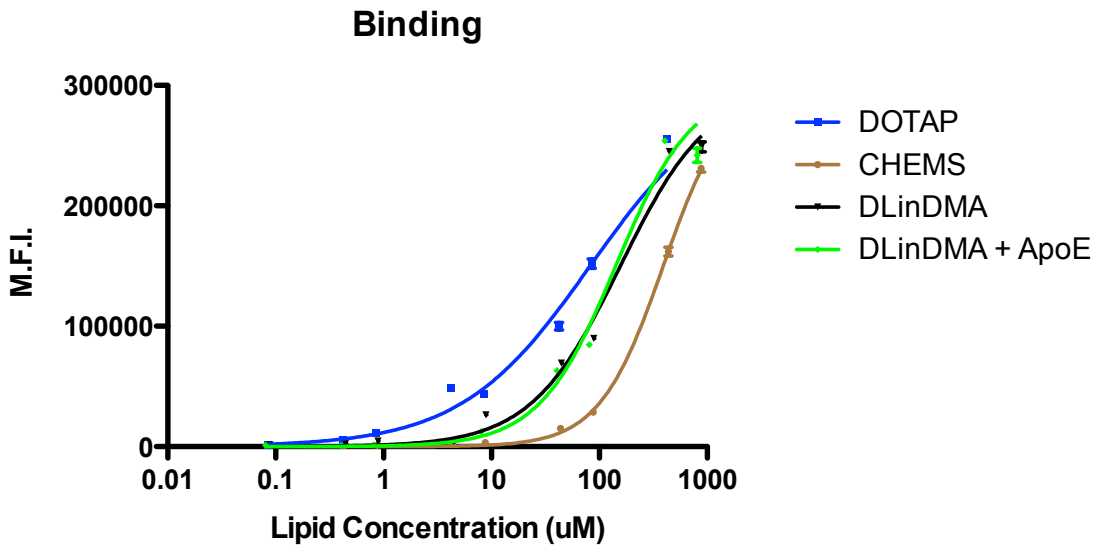

Figure 3.4 Binding of formulations to HeLa cells.
The three different formulations used in the studies were bound to cells at 4 °C at various concentrations between 100 nM and 1 mM to determine the apparent K_d. At each concentration 10,000 cells were counted by FACS. Data +/- 95% CI are shown fitted by non-linear regression to a one site – specific binding with Hill slope model in Prism.

Formulation	K_d (µM)	StDev
CHEMS:DOPE	390.7	8.5
DOTAP:DOPE	73.0	1.8
DLinDMA	156.5	3.9
DLinDMA + ApoE	142.0	2.8

Table 3.2 Apparent K_d measurements from Figure 3.4.
The curves in Figure 3.4 were fit to determine the K_d measurements. Since concentrations over 1 mM lipid could not be achieved, the binding curves were constrained at the top to get coherent fits.

The rate of internalization for each formulation was also determined at the apparent binding K_d concentrations determined in Figure 3.4 (Figure 3.5). Again the media used for microscopy was used for these studies (PBSgp), however, the experiment was performed at 37 ^oC to promote internalization as well. Total intracellular fluorescence was determined by FACS after trypan blue was used to quench extracellular signal and as expected the magnitude of binding after 24 hours of incubated followed the extent of cationic charge for the formulations. Both the magnitude and rate of cellular binding and internalization is consistent with previous findings (Legendre and Szoka, 1992). The rate of internalization is not dependent upon the magnitude of binding as CHEMS:DOPE and DLinDMA in the presence of ApoE exhibit half maximal binding at 4.03 +/- 1.14 and 4.77 +/- 0.50, respectively, despite DLinDMA with ApoE reaching a final magnitude twice that of CHEMS (Table 3.3).

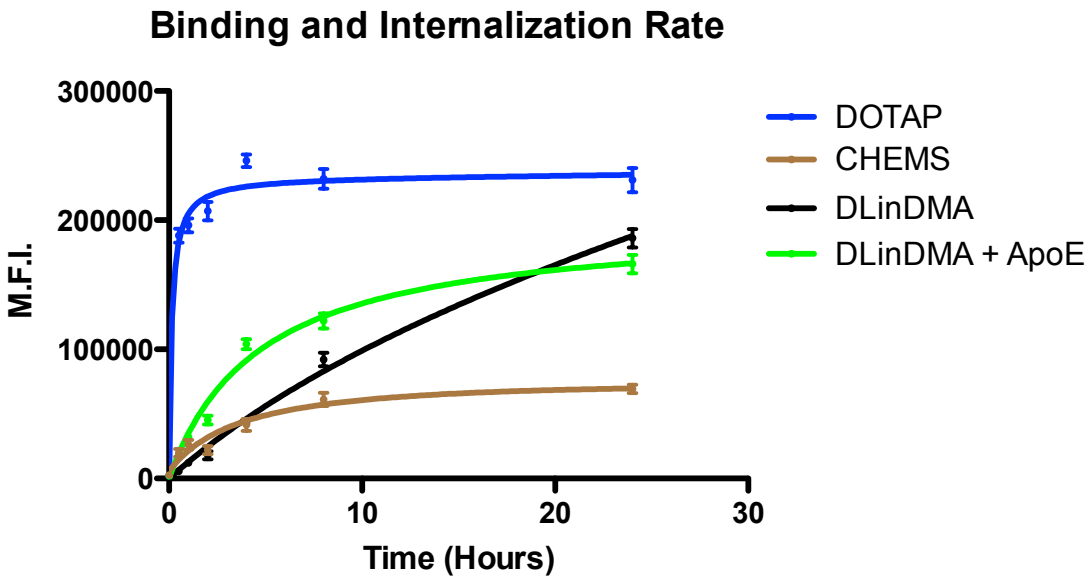

Figure 3.5 Internalization kinetics of formulations into HeLa cells.
The three different formulations used in the studies were incubated with cells at their apparent K_d concentrations and assayed for total intracellular fluorescence over 24 hours. At each concentration 10,000 cells were counted by FACS. Data +/- 95% CI are shown fitted by non-linear regression to a one site – total and nonspecific binding model in Prism.

Formulation	Time to Half Max Internalization (hours)	Maximal Internalization (M.F.I)
CHEMS:DOPE	4.03 +/- 1.14	80,000
DOTAP:DOPE	0.14 +/- 0.01	230,000
DLinDMA	19.23 +/- 1.09	186,000*
DLinDMA + ApoE	4.77 +/- 0.50	200,000

Table 3.3 Internalization rate parameters from Figure 3.5.
The curves in Figure 3.5 were fit to determine the time to half maximal internalization and the maximal internalization measurements. *DLinDMA was constrained at the 24 hour time point for maximal binding.

For DOTAP:DOPE and CHEMS:DOPE the cellular receptors are numerous and non-specific. However, DLinDMA, in the presence of exogenous ApoE, is bound and internalized by the low density lipoprotein receptor (LDLR). A previous publication demonstrated at 20-fold enhancement of DLinDMA cellular uptake in the presence of ApoE after a 4 hour incubation using HeLa cells (Akinc et al., 2010) that is consistent with the data here. However, the effect of ApoE on internalization is not observed at 24 hours of incubation. Interestingly, under the same conditions but in the absence of ApoE, DLinDMA does not appear to be internalized by a saturable process. These data further support that the effect of ApoE in enhancing delivery of DLinDMA is during or after cellular internalization.

3.3.4 pH Measurements of Liposomal Formulations

The liposomes and FITC-dextran were added simultaneously and allowed to co-endocytose. This allowed me to measure the pH of endosomal compartments during endocytosis and cellular trafficking of the liposomes. The initial pulse period was fixed at 30 minutes. I adjusted the concentration of liposomes added to the cells so that after the pulse 10 – 100 liposomes were associated per cell. The concentrations ranged between 0.2 – 1 nM and were scaled based upon

the strength of binding determined earlier (Figure 3.4 & Table 3.2). Following the pulse, non-internalized complexes and FITC-dextran were washed away and images were acquired over a 4 hour chase period.

Figure 3.6 shows the histograms of the 491 nm to 430 nm ratios in clamped cells compared to the experiments with liposomal formulations. The formulations are plotted with the closest clamps to the average pH as indicated in the histograms (Figure 3.7). When comparing the variances of each liposomal population to the corresponding pH clamp using a F-test, the variances of all groups are not significantly different. This result indicates that the underlying variation in the distribution of pH observed for the formulations is explained by the variation in the pH calibration curve. However, this is to be expected, as the image processing method is the same between the calibration curve and the experimental images, and because of the variation of ratios observed in clamped cells.

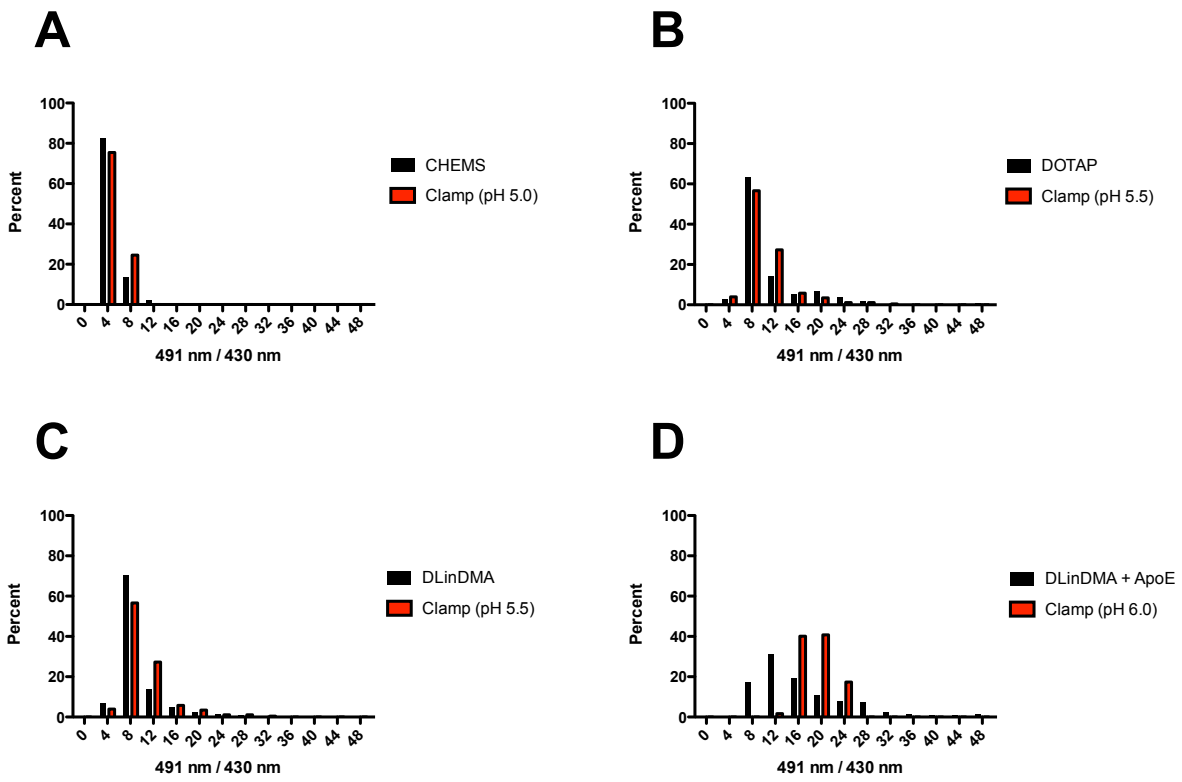

Figure 3.6 Histogram of 491 nm to 430 nm ratios for liposomes and pH clamped cells.
HeLa cells were pulsed with FITC-dextran and the liposomal formulations, washed and chased for 4 hours while images were collected. The histogram of 491 nm to 430 nm ratios for liposomes that colocalize with FITC-dextran interlaced with endosomes clamped at either pH 5.0 (A), pH 5.5 (B and C), or pH 6.0 (D) are shown for the 4 hour experiment. The formulations are: CHEMS (A), DOTAP (B), DLinDMA (C), and DLinDMA with ApoE (D).

The average pH for endosomes containing CHEMS, DOTAP, DLinDMA, and DLinDMA with ApoE acquired over 4 hours are shown in Figure 3.7A. The results indicate that CHEMS colocalizes with a pH consistent with lysosomes at an average pH of 5.03 +/- 0.81 (mean +/- S.D.). The other formulations, DLinDMA, DOTAP and DLinDMA with ApoE, all colocalize to pH compartments consistent with late endosomes and multivesicular bodies (5.42 +/- 1.39, 5.59 +/- 1.18, and 5.81 +/- 1.40, respectively). These data demonstrate that the formulations segregate into compartments with distinct vesicular pH, which agrees with the colocalization of the formulations with compartment markers (section 3.3.6).

In contrast, the average pH of intracellular vesicles labeled with FITC-dextran that do not contain liposomes are shown in Figure 3.7B. The data indicate that FITC-dextran is on average in compartments consistent with lysosomal pH in all experiments except for DLinDMA in the presence of ApoE. In the presence of ApoE the average pH of FITC-dextran is consistent with late endosomes (5.35 +/- 0.47, mean +/- S.D.). These data suggest that 1 μg/ml ApoE present in the imaging media (PBSgp) has an effect on the trafficking of FITC-dextran, and agrees with the observed recycling of ApoE in several studies (Heeren, 2003; Laatsch, 2012). The higher average pH of endosomes in the presence of ApoE can be explained by increased recycling induced by ApoE internalization.

Importantly, t-tests between endosomes containing liposomes versus endosomes lacking liposomes demonstrate significantly increased pH in endosomal compartments containing DOTAP, and DLinDMA both in the absence and presence of ApoE (Figure 3.7A vs B). For DOTAP the difference is 0.62 +/- 0.04 (mean +/- S.D.) pH units, while for DLinDMA in the absence or presence of ApoE is 0.38 +/- 0.03, and 0.46 +/- 0.02, respectively. These data suggest that both DOTAP and DLinDMA have a significant effect on vesicular pH resulting in an apparent buffering of endosomal pH. It is likely that the quaternary amine of DOTAP acts as a sink for Cl^- resulting in inhibition of acidification by ClC channels (Smith, 2010). Similarly, DLinDMA likely buffers endosomal pH because of its tertiary amine, acting in a manner observed with poly-amine polyplexes as a proton sponge (Sonawane, 2003).

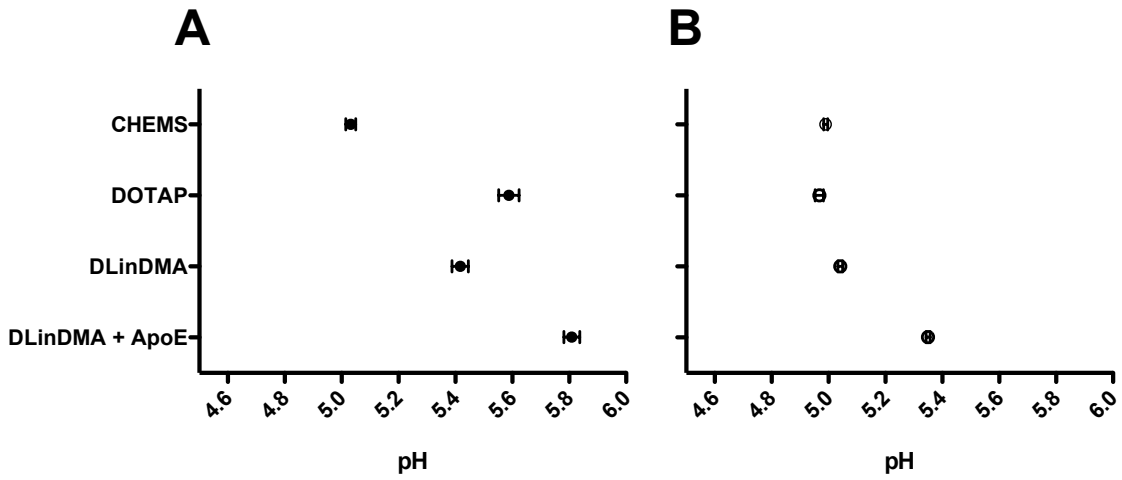

Figure 3.7 Average pH values for endosomes that colocalize with liposomal formulations.
HeLa cells were pulsed with FITC-dextran and the liposomal formulations, washed and chased for 4 hours while images were collected. The average pH of endosomes containing liposomes (A) and endosomes from matched experiments that do not contain liposomes (B) are shown from the 4 hour experiment. Data are plotted as average pH +/- S.E.M.

The increase in population averages of endosomes containing DOTAP and DLinDMA liposomes was plotted with respect to time to determine if the effect on pH was consistent at all times during the experiment (Figure 3.8). The data was binned into 30 minute intervals and demonstrates that at all times in the experiments endosomal pH is increased to a similar level as the overall population averages. In contrast to experiments with poly-amine polyplexes, there is no rapid and dramatic increase in average pH for endosomes containing lipoplex, suggesting that the buffering effect is not strong enough to cause endosomal rupture (Sonawane et al., 2003). These data are consistent with single particle tracking of Lipofectamine 2000 lipoplexes (Rehman et al., 2013).

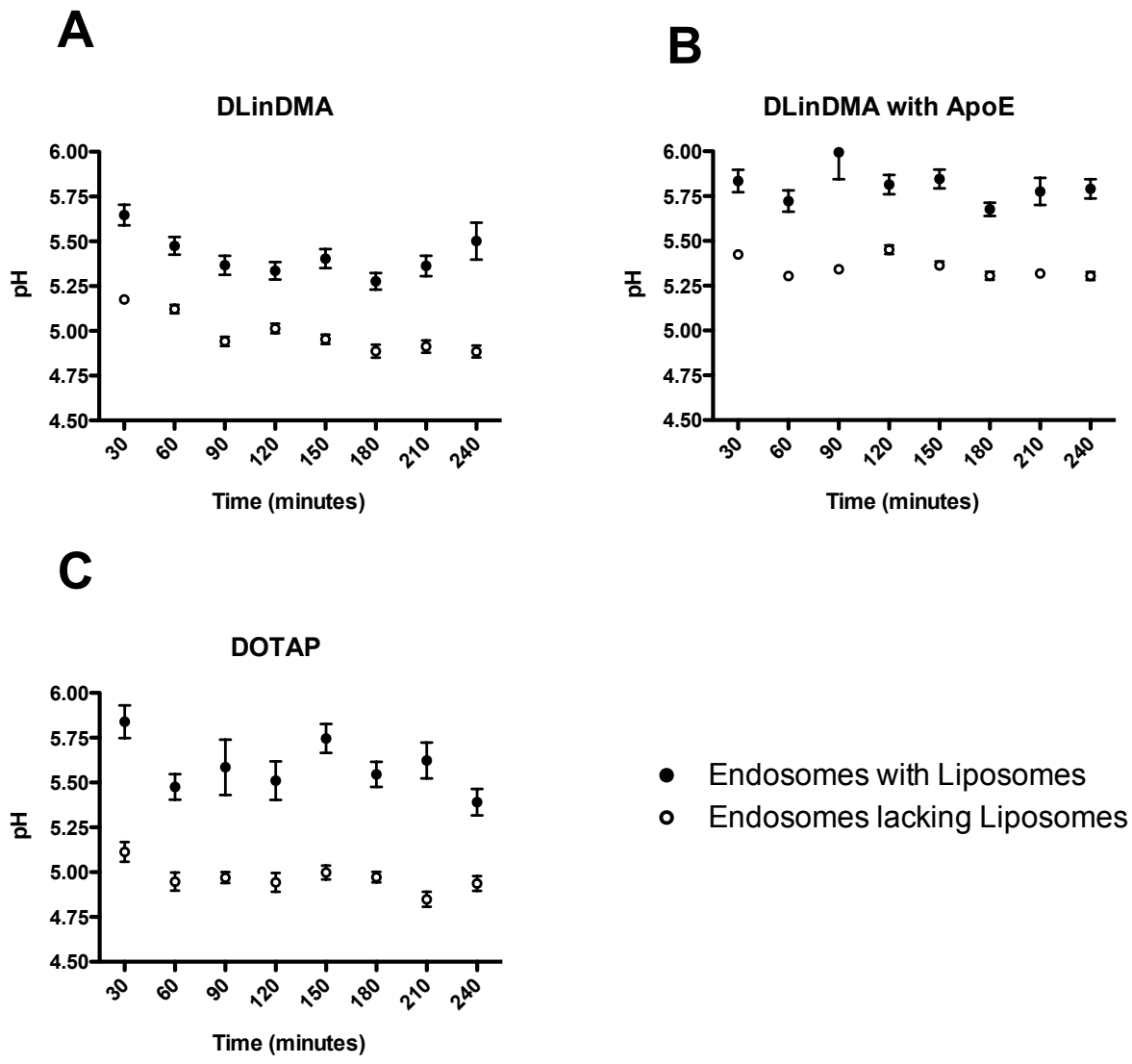

Figure 3.8 Time course of endosome acidification in the presence of DOTAP and DLinDMA liposomes.

HeLa cells were pulsed with FITC-dextran and the liposomal formulations, washed and chased for 4 hours while images were collected. The 4 hour experiment was binned into 30 minute intervals and the average pH per 30 minute interval is plotted. The average pH for endosomes containing liposomes (●) and endosomes lacking liposomes (○) are shown. The formulations are: DLinDMA (A), DLinDMA with ApoE (B), and DOTAP (C). Data are plotted as average pH +/- S.E.M.

The data for the lipid and siRNA signals for each formulation were also analyzed for linear correlations with respect to pH. The $\log_{10}$ of both siRNA and lipid signals in DOTAP liposomes display significant ($p < 0.0001$) linear correlation with respect to pH (Figure 3.9A). The data

indicate an overall ~10-fold loss in both siRNA and lipid signals between pH 4 and 7. This result indicates that in an endosomal context, the integrity of DOTAP liposomes is dependent upon pH. The other formulations tested do not display similar associations with pH, and the TEX615 and DiD fluorophores labeling the siRNA and lipid bilayer are not pH sensitive as shown in Figure 3.9B.

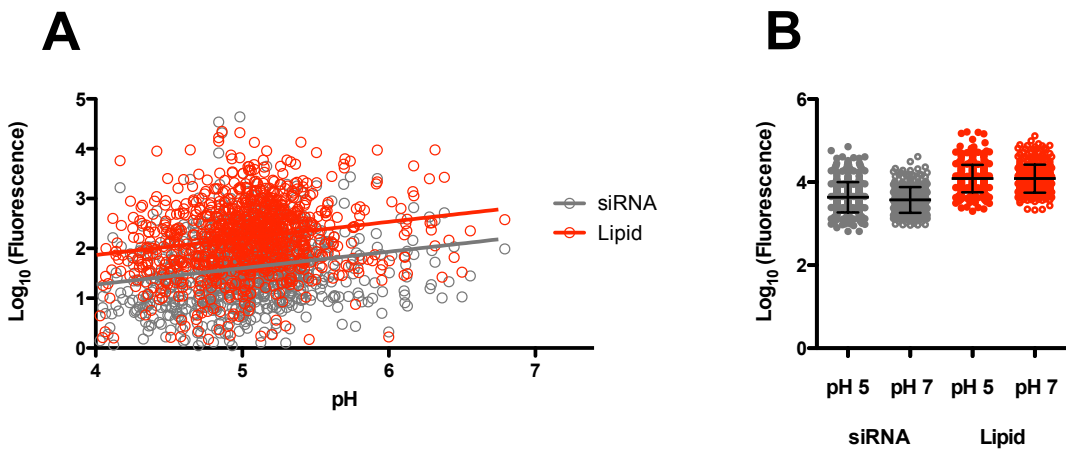

Figure 3.9 Linear associations of log_{10} siRNA and lipid signals in DOTAP liposomes with pH.
The linear association between siRNA and lipid fluorescence intensities (log_{10}) and pH measurements is shown. A) siRNA (gray) intensity and lipid (red) intensity versus pH. B) DOTAP liposomes were imbedded in agarose at pH 5 or pH 7 and the siRNA (gray) and lipid (red) intensities (log_{10}) are plotted for ~ 300 liposomes. Lines represent mean +/- S.D.

3.3.5 Measurements of Liposomal Formulation Integrity

Because the siRNA contents and lipid bilayer were separately labeled, correlations between the intensities of these two signals relative to the starting values are informative of liposome integrity. A greater proportion of lipid signal loss over siRNA would indicate that the lipid bilayer is interacting with biological membranes, but not resulting in de-complexation of siRNA. The distribution of siRNA and lipid signals for each formulation is plotted as a scatter plot to determine how the two signals correlate during a 4 hour imaging experiment (Figure 3.10). In

each graph, the starting populations of liposomes are indicated in green. These starting populations were acquired embedded in agarose and therefore represent the starting distribution of fluorescent intensities in both channels for each liposome preparation. In all cell associated liposomes, there is a 10-fold loss in signal for both the siRNA and lipid channels when compared to the starting population. This suggests that at the low concentrations used in these studies, the particles begin to disassemble when they contact the cell surface, which agrees with previous reports that glycosaminoglycans destabilize lipoplex (Belting and Petersson, 1999; Xu and Szoka, 1996; Zelphati and Szoka, 1996a).

The data in Figure 3.10 also demonstrate that subsequent to cellular internalization, both the siRNA and lipid signals are lost proportionately in all formulations except for the CHEMS formulation. CHEMS has a linear regression slope of 1.15 (1.12 to 1.17, 99.9% CI), while the other formulations have linear regression slopes that overlap 1. The consequence of a slope greater than 1 for CHEMS is that the lipid signal is preferentially lost over the siRNA contents signal. This implies that either DiD transfers out of the CHEMS formulation to a greater extent than the other formulations tested or the lipid bilayer is interacting and exchanging with biological membranes, but not releasing siRNA. Lastly, the distribution of all liposomal formulations in Figure 3.10 is continuous. This suggests that all liposomes disassemble, rather than a sub-population during the 4 hour experiment, which agrees with the findings of other groups (Rehman, 2013).

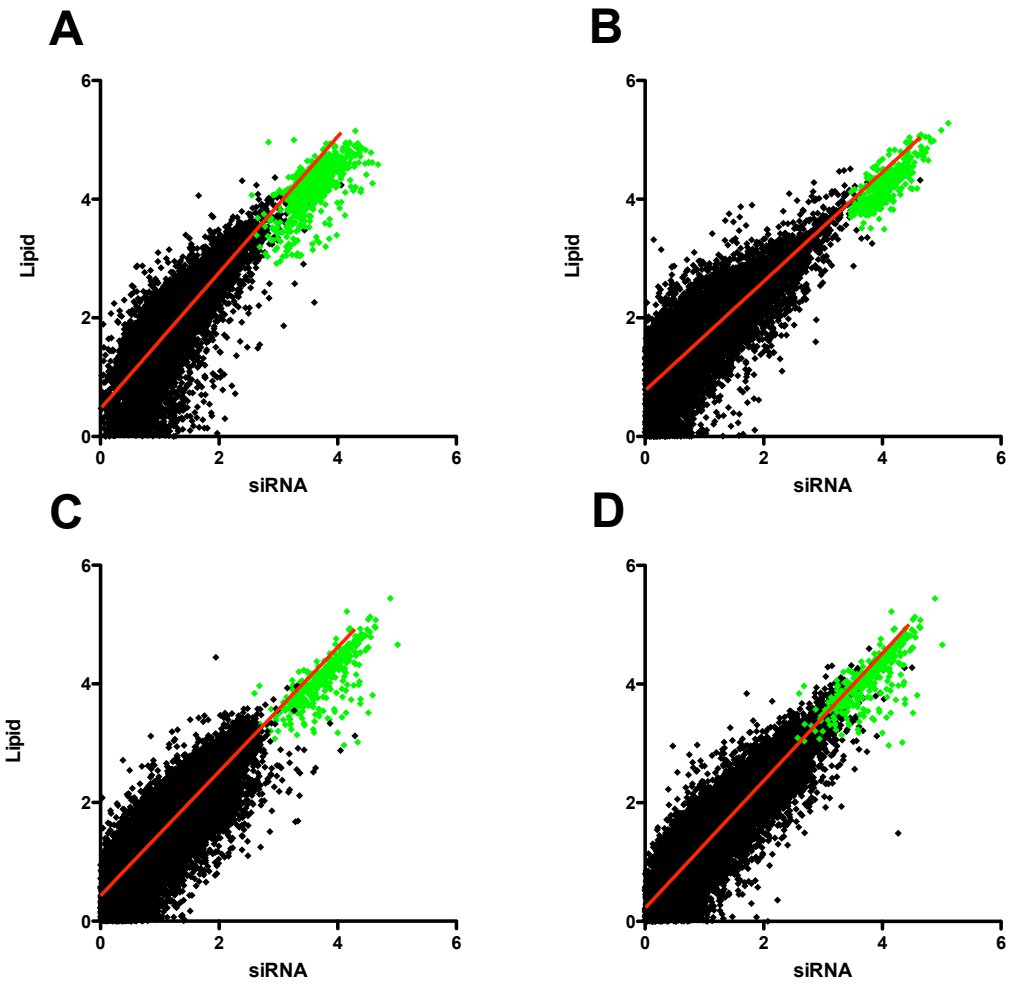

Figure 3.10 Scatter plots of liposome siRNA and lipid signal.
The X- and Y-axis are the $\log_{10}$ of the fluorescence intensity of the siRNA and lipid signal, respectively. A) CHEMS n = 12,113, B) DOTAP n = 27,894, C) DLinDMA n = 24,652, and D) DLinDMA with ApoE n = 26,353. In each graph the population in green is the starting population of liposomes embedded in agarose, and the black population is internalized liposomes. The red lines are linear regressions of the internalized liposome population. Slopes of linear regressions are 1.14 +/- 0.01 (S.E.M.) (A), 0.92 +/- 0.01 (S.E.M.) (B), 1.05 +/- 0.01 (S.E.M.) (C) and 1.07 +/- 0.01 (S.E.M.) (D).

3.3.6 Endosomal Marker Colocalization with Liposomal Formulations

The liposome formulations were colocalized with several endosomal compartment markers that are described in Chapter 2. Liposomes were added at the same concentrations (0.2 – 1 nM) used for the pH measurements. This concentration is low enough so that the internalization pathways

are not saturated. For the early endosomal markers, CltA, Rab5, Cav1, and FLOT1, the cells were pre-incubated with liposomes at 4 ^{o}C for 30 minutes, washed, brought to 37 ^{o}C, and imaged for 1 hour at 37 ^{o}C . For the late endosomal markers, CD82, Rab11a, and LAMP1, the cells were pre-incubated at 37 ^{o}C for 30 minutes, washed and imaged for 4 hours at 37 ^{o}C .

Figure 3.11 A-D shows the percent colocalization with the early endosomal markers with respect to time, and Table 3.4 shows the quality control statistics on the data that was used to generate the curves in Figure 3.11. DOTAP displays an increased colocalization with flotillin-1 during the first hour, starting at 30% and ending at 15% colocalization (Figure 3.11D). DLinDMA shows a preference for both clathrin and Rab5a during the first ~ 10 minutes (Figure 3.11A and B). All formulations colocalize with caveolin-1 to a similar extent (Figure 3.11C).

The late endosomal markers tested, Rab11a, CD82, and LAMP1, display formulation specific colocalization patterns (Figure 3.11 E-G). DOTAP displays a maximal ~ 30% colocalization with recycling endosomes marked with Rab11a at 30 minutes after the start of transfection that continues at ~ 25% colocalization during the remaining 4 hours (Figure 3.11E). DOTAP also displays ~ 30% colocalization with CD82 positive multivesicular bodies at 30 minutes after the start of transfection that drops to the same level (~ 15%) observed for the other formulations by 1 hour (Figure 3.11F). LAMP1 positive lysosomal colocalization of DOTAP is initially low (~ 10%), but eventually increases to ~ 25% by 3 hours (Figure 3.11G). Micrographs of colocalization between DOTAP, Rab11a, CD82, and LAMP1 are shown in Figure 3.12 A-F.

DOTAP displays a change in colocalization pattern during the experiments, while both CHEMS

and DLinDMA reach a uniform level of colocalization during the 30 minute pre-incubation, at which they are maintained throughout the rest of the experiment. DLinDMA has 15% colocalization with all the late endosomal markers tested, which is not due to a reduced number of liposomes per cell as shown in Table 3.4. DLinDMA numbers per cell are within the target range in all experiments, and similar to the numbers achieved with the other formulations. The absence of high levels of colocalization with late endosomal markers and DLinDMA suggests that there are other unlabeled compartments that DLinDMA colocalizes with preferentially.

CHEMS shows a higher colocalization with the lysosomal marker LAMP1 than the other two formulations within the first two hours and remains at a uniform ~ 25% colocalization through out the experiment (Figure 3.11G). Micrographs of colocalization between CHEMS and LAMP1 are shown in Figure 3.12 G and H. Overall colocalization of CHEMS with Rab11a and CD82 is 15% during the 4 hour experiment.

Finally, the observed extent of colocalization with endosomal markers in these studies is consistent with the colocalization of PAMAM dendrimers with similarly tagged markers, which typically ranged between 10 - 50% colocalization (Vercauteren et al., 2011).

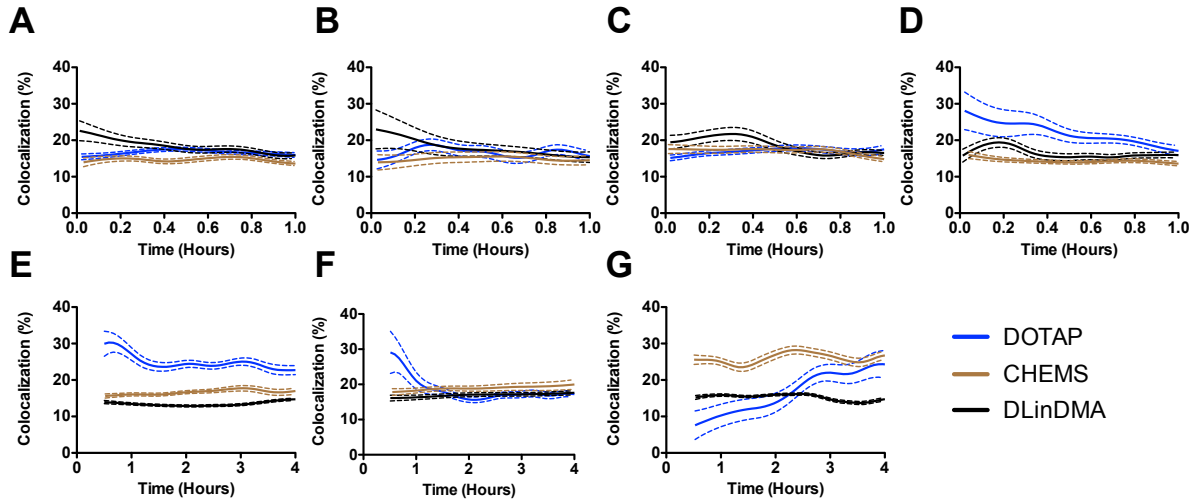

Figure 3.11 Endosomal marker colocalization.
The graphs are local polynomial fitting of liposomal percent colocalization with endosomal markers as a function of time. Errors (S.E.M.) of the fits are represented by dashed lines. The formulations are color-coded: DOTAP, blue; DLinDMA, black; CHEMS, brown. The markers are: A) CltA, B) Rab5a, C) Cav1, D) FLOT1, E) Rab11a, F) CD82, and G) LAMP1.

	CltA			Rab5a		
Formulation	%	n	n per field	%	n	n per field
CHEMS	91.8	16,442	72	63.7	13,900	87
DOTAP	94.5	13,204	56	91.4	14,080	62
DLinDMA	85.6	8,793	41	80.7	12,678	63
	Cav1			FLOT1		
Formulation	%	n	n per field	%	n	n per field
CHEMS	77.8	9,644	50	89.5	19,880	89
DOTAP	83.6	11,559	55	26.7	3,228	48
DLinDMA	70.4	7,865	45	71.6	9,438	53

	Rab11a			CD82		
Formulation	%	n	n per field	%	n	n per field
CHEMS	18.4	24,670	149	61	39,223	71
DOTAP	33.9	12,662	42	90.2	64,332	79
DLinDMA	87.6	92,395	117	89.2	69,238	86
	LAMP1					
Formulation	%	n	n per field			
CHEMS	74.9	18,209	27			
DOTAP	23	2,825	14			
DLinDMA	60.9	130,719	238			

Table 3.4 Quality control data used for the generation of curves in Figure 3.11.
In 1 hour experiments (CltA, Rab5a, Cav1, and FLOT1) there are a total of 250 fields. In 4 hour experiments (Rab11a, CD82 and LAMP1) there are 900 fields. The percentage in the first column of the tables represents the percent of fields with cells in them. For example, CHEMS colocalization with CltA is derived from 230 fields of the 250 total fields or 91.8% (Top left cell). The numbers are the total number of marker-colocalized liposomes per experiment (second column) or per field which is between ~20 - 200 per field in all cases (third column).

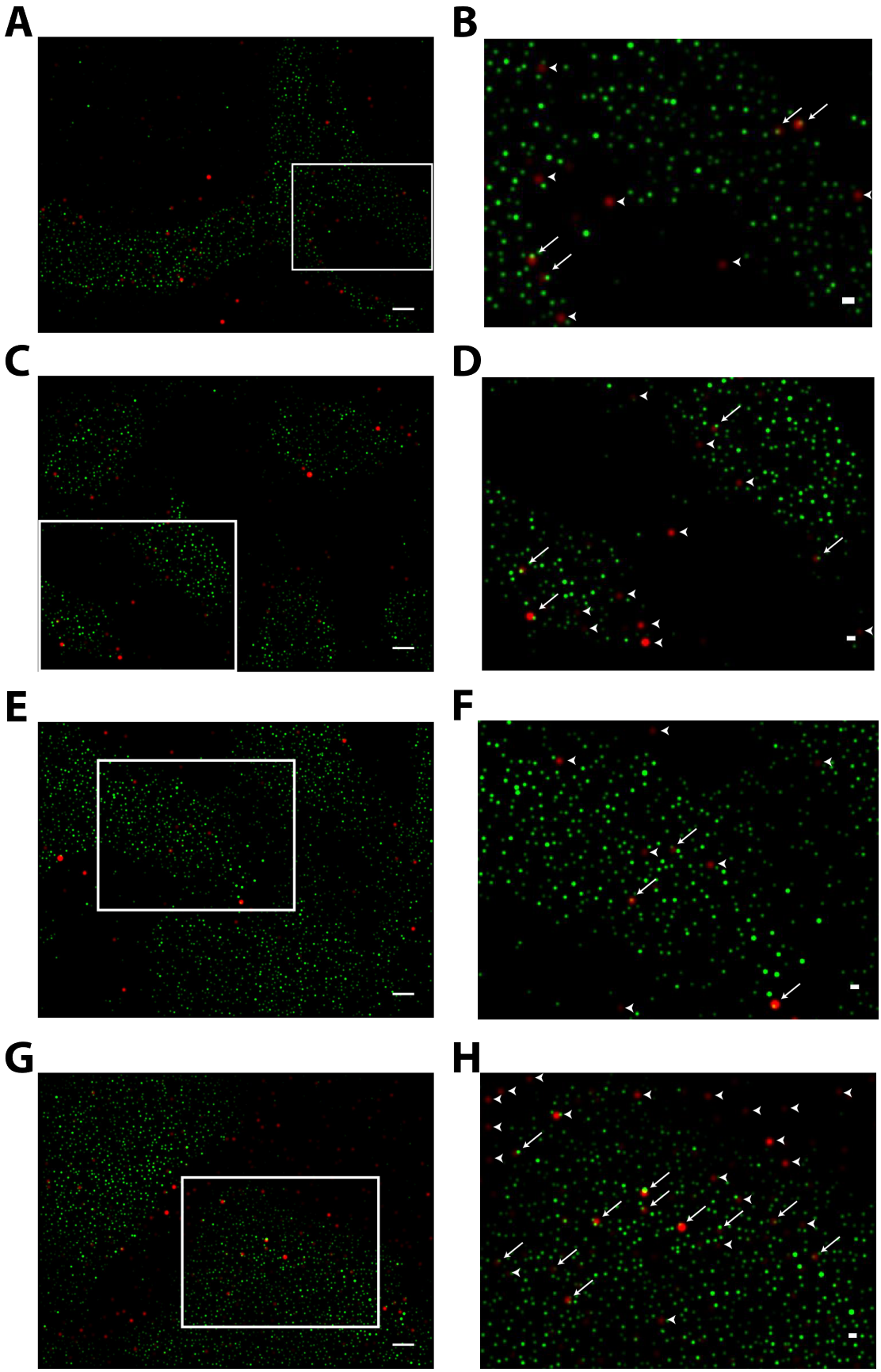
A
B
C
D
E
F
G
H

Figure 3.12 Micrographs of colocalized liposomes with late endosomal markers.
Wide-field epifluorescence images of liposomes incubated with cells expressing endosomal markers. Liposome (red channel) and marker (green channel) combinations are: DOTAP with LAMP1 (A and B), DOTAP with CD82 (C and D), DOTAP with Rab11a (E and F), and CHEMS with LAMP1 (G and H). Full size images with cropped sections indicated by white boxes have scale bars of 5 µm (A, C, E, and G). Cropped sections of corresponding full size images with arrows indicating liposomes that colocalize with markers and arrow-heads indicating liposomes that do not colocalize with markers (B, D, F, and H). Scale bars are 1 µm.

3.4 Conclusion

Here I have described the results of two types of experiments that were done to observe differences in the cellular trafficking of liposomal formulations: 1) FACS based analysis of binding and internalization, and 2) microscopic investigation of liposomes during cellular trafficking. The experiments first confirm that DOTAP is a potent siRNA transfection agent and then provide insight into the underlying mechanism. The results generate hypotheses that can be tested to make liposomal siRNA delivery more efficient.

The FACS based experiments demonstrate that DOTAP binds to cells between 2- and 5-fold better than CHEMS and DLinDMA formulations, respectively. In addition, DOTAP internalizes 30- to 140-fold faster than CHEMS and DLinDMA. The increased binding magnitude and internalization rate partially explain the decreased IC_{50} for siRNA-mediated knockdown of luciferase *in vitro*, however, cellular trafficking events subsequent to binding and internalization were also investigated.

By optically measuring endosomal pH, I first demonstrate that intracellular vesicles that contain DOTAP are, on average, 0.62 pH units higher than vesicles that do not contain DOTAP (Figure 3.7). This suggests that DOTAP either alters the acidification of endosomes or becomes

sequestered in vesicles with slightly higher pH. This property is also observed with DLinDMA, which exhibits a ~ 0.4 pH unit increase. In addition, both DOTAP and DLinDMA cause an overall increase in pH throughout the 4 hour experiment (Figure 3.8). For DOTAP, both the siRNA and lipid signals are correlated with pH and demonstrate a 10-fold loss in between pH 7 and pH 4 (Figure 3.9). These data suggest that DOTAP undergoes a pH-dependent disassembly in an endosomal context.

In analyzing overall particle integrity, the experimental results demonstrate that the siRNA and lipid signals are lost equally from all formulations except CHEMS. Intuitively, one would expect that the lipid signal would be preferentially lost over the siRNA signal as a result of lipid mixing, consistent with what has been observed with HIV-1 fusion (Miyauchi et al., 2009). In this assay it is impossible to directly detect the lipid mixing intermediate as it is not stabilized by viral or cellular proteins (Giraudo et al., 2005; Nüssler et al., 1997) and will be faster than the 500 ms exposure times used (Chizmadzhev et al., 2000). However, it is possible to detect the result of lipid mixing, which would generate either a separate population of liposomes with low lipid signal and high contents signal, a downward bow, or an overall steeper slope in Figure 3.10. The results indicate that in endosomes, lipid mixing is almost always followed by decomplexation of siRNA. CHEMS either does not exhibit the same propensity to disassemble or the DiD fluorophore transfers out of the bilayer at a faster rate than the other formulations.

In turning to the colocalization of the formulations with endosomal markers, the colocalization with the early endosomal markers demonstrates that DOTAP uses the flotillin-dependent pathway to a slightly greater extent than the other formulations. In several cell types, recycling

endosomes are enriched in flotillin-1 and flotillin-1 delivers cargo (GPI anchored proteins) to recycling endosomes (Gagescu, 2000; Sabharanjak, 2002). This provides a link between the increased colocalization of DOTAP with flotillin-1 and Rab11a.

The colocalization of the formulations with the recycling endosome marker Rab11a, shows that DOTAP has a peak colocalization of 30% at 30 minutes after transfection followed by a constant 25% colocalization during the remaining 4 hours (Figure 3.11E). This suggests that DOTAP accumulates in the non-lysosomal recycling compartment, potentially serving as an intracellular depot allowing multiple rounds of fusion and contents release to occur. These results agree with a recent study that found a 2-fold increase in siRNA IC_{50} when Rab11a is knocked down (Sahay et al., 2013).

DOTAP also shows a peak colocalization with the multivesicular body marker, CD82, of 30% at 30 minutes after transfection that decreases to 15% colocalization for the remaining 4 hours (Figure 3.11F). It is believed that the cytoplasmic face of multivesicular bodies is the site of RISC recycling and is primed at that location for loading new guide strands (Gibbings and Voinnet, 2010; Gibbings et al., 2009). The DOTAP:siRNA complexes would be in the lumen of a MVB, and therefore potential increases in colocalization with CD82 would be advantageous if delivery of siRNA occurred at this site as well. In essence, it is possible that DOTAP delivers siRNA to the subcellular site of RISC turnover where it is primed to accept new guide strands.

Finally, the localization of liposomes with LAMP1 demonstrates that CHEMS exhibits a high and constant 25% colocalization with lysosomes starting at 30 minutes after transfection (Figure

3.11G). These data suggest that the low efficiency of CHEMS at delivering siRNA is driven by rapid and relatively high lysosomal accumulation, compared to the other formulations. In contrast, DOTAP demonstrates a slow accumulation into LAMP1 positive compartments starting at ~ 10% 30 minutes after transfection, and climbing to 25% by the end of 4 hours (Figure 3.11G). These data suggest that DOTAP slows or alters endosome kinetics, which is in agreement with the pH measurements using FITC-dextran that demonstrated a significantly higher average pH of vesicles containing DOTAP than empty vesicles.

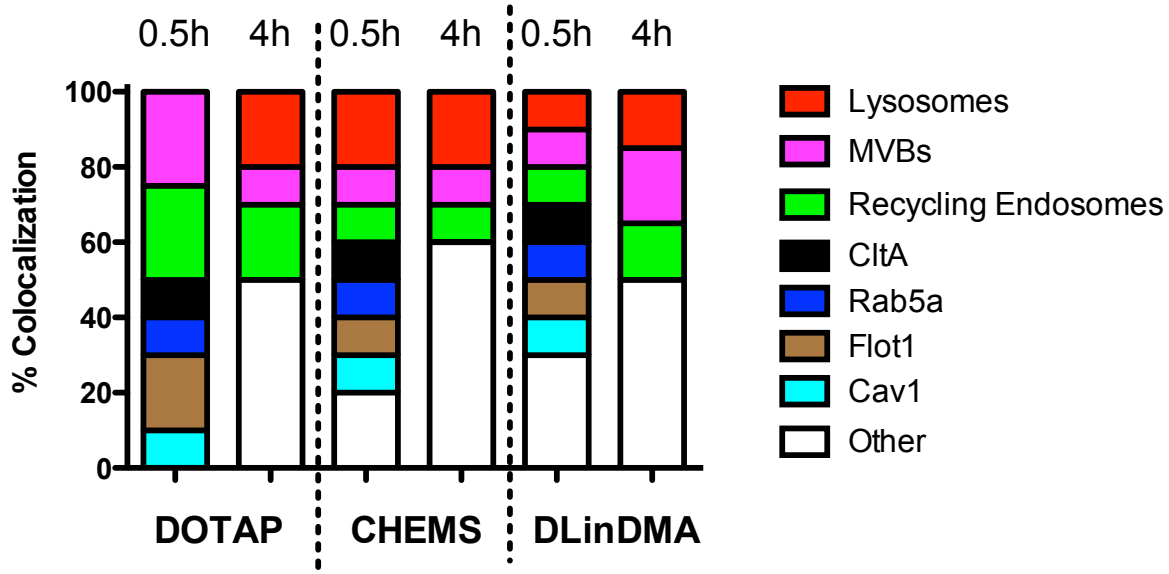

Figure 3.13 Summary of liposomal colocalization with compartment markers.
The additive colocalization of each formulation with the endosomal compartment markers tested. The colocalization of each formulations at 30 minutes and 4 hours is shown.

Figure 3.13 summarizes the colocalization of each formulation with the markers tested. It should be stated that the additive percent colocalization presented in Figure 3.13 is a guide to summarize which markers the formulations display a preference for. There is significant overlap between many of the compartments labeled and summation of all markers tested can lead to over 100% colocalization at certain time points. For example, clathrin and caveolin both colocalize with Rab5a, while flotillin-1 and Rab11a have been demonstrated to colocalize (Gagescu, 2000;

Sabharanjak, 2002; Sharma, 2003; Hagiwara, 2009). There is also overlap of CD82 with both Rab11a and LAMP1 (Möbius, 2003; Piper, 2007). Despite this, at 30 minutes between 70 – 100% of liposomes are accounted for by all the markers used suggesting that these markers adequately describe the trafficking events of the liposome formulations tested. In contrast between 40 and 50% of liposomes are accounted for by the late endosome compartments markers at 4 hours, which suggests that other events can still be detected and described using other compartment markers.

In conclusion, these data provide insights into how the cell differentially traffics and processes liposomal formulations. The cellular trafficking of DOTAP liposomes contributes to its observed potency *in vitro*. DOTAP is characterized by the ability to increase endosomal pH, colocalize with flotillin-1, Rab11a, and CD82 to a greater extent, and with LAMP1 to a lesser extent than the other formulations tested. The observations of liposomal trafficking detailed here, suggest that the differences observed between DOTAP and the other formulations tested are properties that make a liposomal formulation more efficient at delivery, and provide testable hypotheses to directly establish causation in future experiments.

3.5 References

Akinc, A., Querbes, W., De, S., Qin, J., Frank-Kamenetsky, M., Jayaprakash, K.N., Jayaraman, M., Rajeev, K.G., Cantley, W.L., Dorkin, J.R., et al. (2010). Targeted delivery of RNAi therapeutics with endogenous and exogenous ligand-based mechanisms. Mol Ther *18*, 1357–1364.

Akita, H., Enoto, K., Masuda, T., Mizuguchi, H., Tani, T., and Harashima, H. (2010). Particle Tracking of Intracellular Trafficking of Octaarginine-modified Liposomes: A Comparative Study With Adenovirus. Mol Ther *18*, 955–964.

Akita, H., Enoto, K., Tanaka, H., and Harashima, H. (2012). Particle Tracking Analysis for the Intracellular Trafficking of Nanoparticles Modified with African Swine Fever Virus Protein p54-derived Peptide. Mol Ther.

Avilov, S.V., Moisy, D., Naffakh, N., and Cusack, S. (2012). Influenza A virus progeny vRNP trafficking in live infected cells studied with the virus-encoded fluorescently tagged PB2 protein. Vaccine *30*, 7411–7417.

Behr, J.-P. (1997). The Proton Sponge: a Trick to Enter Cells the Viruses Did Not Exploit. CHIMIA International Journal for Chemistry.

Belting, M., and Petersson, P. (1999). Intracellular accumulation of secreted proteoglycans inhibits cationic lipid-mediated gene transfer. Co-transfer of glycosaminoglycans to the nucleus. J Biol Chem *274*, 19375–19382.

Berezhna, S., Schaefer, S., Heintzmann, R., Jahnz, M., Boese, G., Deniz, A., and Schwille, P. (2005). New effects in polynucleotide release from cationic lipid carriers revealed by confocal imaging, fluorescence cross-correlation spectroscopy and single particle tracking. Biochim Biophys Acta *1669*, 193–207.

Braeckmans, K., Buyens, K., Bouquet, W., Vervaet, C., Joye, P., De Vos, F., Plawinski, L., Doeuvre, L., Angles-Cano, E., Sanders, N.N., et al. (2010a). Sizing nanomatter in biological fluids by fluorescence single particle tracking. Nano Lett *10*, 4435–4442.

Braeckmans, K., Buyens, K., Naeye, B., Vercauteren, D., Deschout, H., Raemdonck, K., Remaut, K., Sanders, N.N., Demeester, J., and de Smedt, S.C. (2010b). Advanced fluorescence microscopy methods illuminate the transfection pathway of nucleic acid nanoparticles. Journal of Controlled Release *148*, 69–74.

Brandenburg, B., and Zhuang, X. (2007). Virus trafficking - learning from single-virus tracking. Nat Rev Microbiol *5*, 197–208.

Chithrani, D.B., Dunne, M., Stewart, J., Allen, C., and Jaffray, D.A. (2010). Cellular uptake and transport of gold nanoparticles incorporated in a liposomal carrier. Nanomedicine: Nanotechnology, Biology and Medicine *6*, 161–169.

Chizmadzhev, Y.A., Kuzmin, P.I., Kumenko, D.A., Zimmerberg, J., and Cohen, F.S. (2000).

Dynamics of fusion pores connecting membranes of different tensions. Biophys J *78*, 2241–2256.

Coller, K.E., Berger, K.L., Heaton, N.S., Cooper, J.D., Yoon, R., and Randall, G. (2009). RNA interference and single particle tracking analysis of hepatitis C virus endocytosis. PLoS Pathog *5*, e1000702.

de Bruin, K.G., Fella, C., Ogris, M., Wagner, E., Ruthardt, N., and Bräuchle, C. (2008). Dynamics of photoinduced endosomal release of polyplexes. Journal of Controlled Release *130*, 175–182.

de Bruin, K., Ruthardt, N., Gersdorff, von, K., Bausinger, R., Wagner, E., Ogris, M., and Bräuchle, C. (2007). Cellular Dynamics of EGF Receptor–Targeted Synthetic Viruses. Molecular Therapy *15*, 1297–1305.

Ducat, E., Deprez, J., Gillet, A., Noël, A., Evrard, B., Peulen, O., and Piel, G. (2011). Nuclear delivery of a therapeutic peptide by long circulating pH-sensitive liposomes: Benefits over classical vesicles. Int J Pharm.

Ellens, H., Bentz, J., and Szoka, F.C., Jr (1984). pH-induced destabilization of phosphatidylethanolamine-containing liposomes: role of bilayer contact. Biochemistry *23*, 1532–1538.

Farhood, H., Serbina, N., and Huang, L. (1995). The role of dioleoyl phosphatidylethanolamine in cationic liposome mediated gene transfer. Biochim Biophys Acta *1235*, 289–295.

Gagescu, R., Demaurex, N., Parton, R.G., Hunziker, W., Huber, L.A., and Gruenberg, J. (2000). The recycling endosome of Madin-Darby canine kidney cells is a mildly acidic compartment rich in raft components. Mol Biol Cell *11*, 2775–2791.

Gibbings, D., and Voinnet, O. (2010). Control of RNA silencing and localization by endolysosomes. Trends Cell Biol *20*, 491–501.

Gibbings, D.J., Ciaudo, C., Erhardt, M., and Voinnet, O. (2009). Multivesicular bodies associate with components of miRNA effector complexes and modulate miRNA activity. Nat Cell Biol *11*, 1143–1149.

Giraudo, C.G., Hu, C., You, D., Slovic, A.M., Mosharov, E.V., Sulzer, D., Melia, T.J., and Rothman, J.E. (2005). SNAREs can promote complete fusion and hemifusion as alternative outcomes. J Cell Biol *170*, 249–260.

Hafez, I.M.I., Maurer, N.N., and Cullis, P.R.P. (2001). On the mechanism whereby cationic lipids promote intracellular delivery of polynucleic acids. Gene Ther *8*, 1188–1196.

Hagiwara, M., Shirai, Y., Nomura, R., Sasaki, M., Kobayashi, K.-I., Tadokoro, T., and Yamamoto, Y. (2009). Caveolin-1 activates Rab5 and enhances endocytosis through direct interaction. Biochem Biophys Res Commun *378*, 73–78.

Heeren, J., Grewal, T., Laatsch, A., Rottke, D., Rinninger, F., Enrich, C., and Beisiegel, U. (2003). Recycling of apoprotein E is associated with cholesterol efflux and high density lipoprotein internalization. J Biol Chem *278*, 14370–14378.

Humphries, W.H., Szymanski, C.J., and Payne, C.K. (2011). Endo-lysosomal vesicles positive for Rab7 and LAMP1 are terminal vesicles for the transport of dextran. PLoS ONE *6*, e26626–e26626.

Imamura, J., Suzuki, Y., Gonda, K., Roy, C.N., Gatanaga, H., Ohuchi, N., and Higuchi, H. (2011). Single particle tracking confirms that multivalent Tat protein transduction domain-induced heparan sulfate proteoglycan cross-linkage activates Rac1 for internalization. Journal of Biological Chemistry *286*, 10581–10592.

Jin, H., Heller, D.A., Sharma, R., and Strano, M.S. (2009). Size-dependent cellular uptake and expulsion of single-walled carbon nanotubes: single particle tracking and a generic uptake model for nanoparticles. ACS Nano *3*, 149–158.

Kim, A.J., Boylan, N.J., Suk, J.S., Lai, S.K., and Hanes, J. (2011). Non-degradative intracellular trafficking of highly compacted polymeric DNA nanoparticles. Journal of Controlled Release.

Koltover, I., Salditt, T., Rädler, J.O., and Safinya, C.R. (1998). An inverted hexagonal phase of cationic liposome-DNA complexes related to DNA release and delivery. Science *281*, 78–81.

Laatsch, A., Panteli, M., Sornsakrin, M., Hoffzimmer, B., Grewal, T., and Heeren, J. (2012). Low density lipoprotein receptor-related protein 1 dependent endosomal trapping and recycling of apolipoprotein E. PLoS ONE *7*, e29385.

Lai, M.Z., Vail, W.J., and Szoka, F.C., Jr (1985). Acid- and calcium-induced structural changes in phosphatidylethanolamine membranes stabilized by cholesteryl hemisuccinate. Biochemistry *24*, 1654–1661.

Lai, S.K., and Hanes, J. (2008). Real-time multiple particle tracking of gene nanocarriers in complex biological environments. Methods Mol Biol *434*, 81–97.

Legendre, J.Y., and Szoka, F.C., Jr (1992). Delivery of plasmid DNA into mammalian cell lines using pH-sensitive liposomes: comparison with cationic liposomes. Pharm Res *9*, 1235–1242.

Liu, S.-L., Zhang, Z.-L., Tian, Z.-Q., Zhao, H.-S., Liu, H., Sun, E.-Z., Xiao, G.F., Zhang, W., Wang, H.-Z., and Pang, D.-W. (2011). Effectively and Efficiently Dissecting the Infection of Influenza Virus by Quantum-Dot-Based Single-Particle Tracking. ACS Nano.

Mickler, F.M., Möckl, L., Ruthardt, N., Ogris, M., Wagner, E., and Bräuchle, C. (2012). Tuning Nanoparticle Uptake: Live-Cell Imaging Reveals Two Distinct Endocytosis Mechanisms Mediated by Natural and Artificial EGFR Targeting Ligand. Nano Lett.

Miyauchi, K., Kim, Y., Latinovic, O., Morozov, V., and Melikyan, G.B. (2009). HIV Enters Cells via Endocytosis and Dynamin-Dependent Fusion with Endosomes. Cell *137*, 433–444.

Möbius, W., van Donselaar, E., Ohno-Iwashita, Y., Shimada, Y., Heijnen, H.F.G., Slot, J.W., and Geuze, H.J. (2003). Recycling compartments and the internal vesicles of multivesicular bodies harbor most of the cholesterol found in the endocytic pathway. Traffic *4*, 222–231.

Nüssler, F., Clague, M.J., and Herrmann, A. (1997). Meta-stability of the hemifusion intermediate induced by glycosylphosphatidylinositol-anchored influenza hemagglutinin. Biophys J *73*, 2280–2291.

Payne, C.K. (2007). Imaging gene delivery with fluorescence microscopy. Nanomedicine (London, England) *2*, 847–860.

Pelkmans, L., Kartenbeck, J., and Helenius, A. (2001). Caveolar endocytosis of simian virus 40 reveals a new two-step vesicular-transport pathway to the ER. Nat Cell Biol *3*, 473–483.

Piper, R.C., and Katzmann, D.J. (2007). Biogenesis and function of multivesicular bodies. Annu. Rev. Cell Dev. Biol. *23*, 519–547.

Rehman, Z.U., Hoekstra, D., and Zuhorn, I.S. (2013). Mechanism of Polyplex- and Lipoplex-Mediated Delivery of Nucleic Acids: Real-Time Visualization of Transient Membrane Destabilization without Endosomal Lysis. ACS Nano.

Rejman, J., Oberle, V., Zuhorn, I.S., and Hoekstra, D. (2004). Size-dependent internalization of particles via the pathways of clathrin- and caveolae-mediated endocytosis. Biochem J *377*, 159–169.

Rust, M.J., Lakadamyali, M., Zhang, F., and Zhuang, X. (2004). Assembly of endocytic machinery around individual influenza viruses during viral entry. Nat Struct Mol Biol *11*, 567–573.

Ruthardt, N., Lamb, D.C., and Bräuchle, C. (2011). Single-particle Tracking as a Quantitative Microscopy-based Approach to Unravel Cell Entry Mechanisms of Viruses and Pharmaceutical Nanoparticles. Mol Ther.

Sabharanjak, S., Sharma, P., Parton, R.G., and Mayor, S. (2002). GPI-anchored proteins are delivered to recycling endosomes via a distinct cdc42-regulated, clathrin-independent pinocytic pathway. Dev Cell *2*, 411–423.

Sahay, G., Querbes, W., Alabi, C., Eltoukhy, A., Sarkar, S., Zurenko, C., Karagiannis, E., Love, K., Chen, D., Zoncu, R., et al. (2013). Efficiency of siRNA delivery by lipid nanoparticles is limited by endocytic recycling. Nat Biotechnol *31*, 653–658.

Sauer, A.M., de Bruin, K.G., Ruthardt, N., Mykhaylyk, O., Plank, C., and Bräuchle, C. (2009). Dynamics of magnetic lipoplexes studied by single particle tracking in living cells. Journal of Controlled Release *137*, 136–145.

Scotti, E., Calamai, M., Goulbourne, C.N., Zhang, L., Hong, C., Lin, R.R., Choi, J., Pilch, P.F., Fong, L.G., Zou, P., et al. (2013). IDOL stimulates clathrin-independent endocytosis and MVB-mediated lysosomal degradation of the LDLR. Mol Cell Biol.

Semple, S., Akinc, A., Chen, J., Sandhu, A., Mui, B., Cho, C., Sah, D., Stebbing, D., Crosley, E., Yaworski, E., et al. (2010). Rational design of cationic lipids for siRNA delivery. Nat Biotechnol *28*, 172–176.

Sharma, D.K., Choudhury, A., Singh, R.D., Wheatley, C.L., Marks, D.L., and Pagano, R.E. (2003). Glycosphingolipids internalized via caveolar-related endocytosis rapidly merge with the clathrin pathway in early endosomes and form microdomains for recycling. J Biol Chem *278*, 7564–7572.

Smith, A.J., and Lippiat, J.D. (2010). Direct endosomal acidification by the outwardly rectifying CLC-5 Cl(-)/H(+) exchanger. J Physiol (Lond) *588*, 2033–2045.

Sonawane, N.D., Szoka, F.C., Jr, and Verkman, A.S. (2003). Chloride accumulation and swelling in endosomes enhances DNA transfer by polyamine-DNA polyplexes. J Biol Chem *278*, 44826–44831.

Suh, J., Dawson, M., and Hanes, J. (2005). Real-time multiple-particle tracking: applications to drug and gene delivery. Adv Drug Deliv Rev *57*, 63–78.

Suk, J.S., Suh, J., Lai, S.K., and Hanes, J. (2007). Quantifying the intracellular transport of viral and nonviral gene vectors in primary neurons. Exp. Biol. Med. (Maywood) *232*, 461–469.

Tian, T., Wang, Y., Wang, H., Zhu, Z., and Xiao, Z. (2010). Visualizing of the cellular uptake and intracellular trafficking of exosomes by live-cell microscopy. J Cell Biochem.

Tian, T., Zhu, Y.-L., Hu, F.-H., Wang, Y.-Y., Huang, N.-P., and Xiao, Z.-D. (2012). Dynamics of exosome internalization and trafficking. J Cell Physiol.

van der Schaar, H.M., Rust, M.J., Chen, C., van der Ende-Metselaar, H., Wilschut, J., Zhuang, X., and Smit, J.M. (2008). Dissecting the cell entry pathway of dengue virus by single-particle tracking in living cells. PLoS Pathog *4*, e1000244.

Vercauteren, D., Deschout, H., Remaut, K., Engbersen, J.F.J., Jones, A.T., Demeester, J., de Smedt, S.C., and Braeckmans, K. (2011). Dynamic colocalization microscopy to characterize intracellular trafficking of nanomedicines. ACS Nano *5*, 7874–7884.

Wrobel, I., and Collins, D. (1995). Fusion of cationic liposomes with mammalian cells occurs after endocytosis. Biochim Biophys Acta *1235*, 296–304.

Xu, Y., and Szoka, F.C., Jr (1996). Mechanism of DNA release from cationic liposome/DNA complexes used in cell transfection. Biochemistry *35*, 5616–5623.

Yu, J., Wu, C., Sahu, S.P., Fernando, L.P., Szymanski, C., and McNeill, J. (2009). Nanoscale 3D tracking with conjugated polymer nanoparticles. J Am Chem Soc *131*, 18410–18414.

Zelphati, O., and Szoka, F.C., Jr (1996a). Mechanism of oligonucleotide release from cationic liposomes. Proc Natl Acad Sci USA *93*, 11493–11498.

Zelphati, O., and Szoka, F.C., Jr (1996b). Intracellular distribution and mechanism of delivery of oligonucleotides mediated by cationic lipids. Pharm Res *13*, 1367–1372.

Zelphati, O., Uyechi, L.S., Barron, L.G., and Szoka, F.C., Jr (1998). Effect of serum components on the physico-chemical properties of cationic lipid/oligonucleotide complexes and on their interactions with cells. Biochim Biophys Acta *1390*, 119–133.

Zuhorn, I.S., Bakowsky, U., Polushkin, E., Visser, W.H., Stuart, M.C.A., Engberts, J.B.F.N., and Hoekstra, D. (2005). Nonbilayer phase of lipoplex-membrane mixture determines endosomal escape of genetic cargo and transfection efficiency. Mol Ther *11*, 801–810.

Chapter 4 : siRNA Uptake Through SIDT-1

4.1 Introduction

Since the discovery of RNAi in *C. elegans* (Fire et al., 1998) and the subsequent extension to cultured mammalian cells (Elbashir et al., 2001a; 2001b) rapid progress has been made at developing therapeutics harnessing the RNAi mechanism to treat disease. The largest hurdle to overcome in development of a nucleic acid based therapeutic is the delivery problem that has existed since before the discovery of RNAi and continually hampered gene therapy. The delivery problem centers around the resistance of cellular membranes to passage of charged macromolecules. Viral vectors have evolved to be efficient and potent at delivery of genetic material to infected cells, but have several well known drawbacks: systemic inflammatory response, immune system rejection, insertional mutagenesis, and payload limitations of nucleic acid size and structure. These limitations are ameliorated, at least in part, by the development of non-viral vectors, but bring back the delivery problem.

As a corollary to understanding vector based delivery mechanisms comprising the bulk of this thesis, alternative mechanisms of nucleic acid transport were also investigated. Typically, macromolecules the size of siRNA, transit cellular membranes by endocytosis, however, the nuclear pore, gap junctions and the transporter associated with antigen processing (TAP) are well-characterized transporters of macromolecules (Kizana et al., 2009; Mohr et al., 2009; Zhao et al., 2006). A more pertinent example is the nucleic acid channel (NACh), which has been demonstrated by patch-clamp experiments to be specific for ssDNA, voltage and energy independent, requires calcium and is regulated by cytosolic malate dehydrogenase (Hanss et al., 1998; 2002; Rappaport et al., 1995). However, a double stranded RNA (dsRNA) specific

transporter has been identified, in *C. elegans* named, systemic interference defective 1 (*sid*-1) (Feinberg and Hunter, 2003) (Tijsterman et al., 2004).

sid-1 has two human homologs named SIDT-1 and SIDT-2 that share 34% and 32% similarity to SID-1, respectively. Unmodified siRNA has been demonstrated to be internalized when SIDT-1 is over expressed in cultured cells, and mediate the knockdown of GFP and luciferase (Duxbury et al., 2005). Interestingly, this transporter does not appear to require energy for transport as neither oligomycin nor cold inhibit cellular accumulation of dsRNA (Duxbury et al., 2005; Feinberg and Hunter, 2003). More recently SID-1 was demonstrated to be a dsRNA specific ligand gated channel (Shih et al., 2011), and the extracellular domain was determined by SAXS to be a tetramer with a central dimple consistent with a 2.3 nm diameter pore to accommodate A-form dsRNA helix (Pratt et al., 2012). Despite the observed ligand gated channel activity of SID-1, there is no putative dsRNA binding domain in the protein. While it is possible that some other molecule acts as an allosteric regulatory ligand, it is unlikely as dsRNA uptake is observed when SID-1 is ectopically expressed in *D. melanogaster* S2 cells that lack a sid-1 homologue (Feinberg and Hunter, 2003).

A dsRNA transporter such as SID-1 could potentially be an important mechanism to deliver therapeutic siRNA. Several hybrid platforms have been developed that use endogenous LDL or albumin transport mechanisms through conjugation of cholesterol or short chain fatty acids to siRNA (Lorenz et al., 2004; MacKellar et al., 1992; Nakayama et al., 2012; Wolfrum et al., 2007). The “lipophillic” siRNA becomes incorporated into serum LDL, HDL, and albumin that mediates its prolonged circulation and liver uptake. However, the question of how the siRNA

gets incorporated into cytoplasmic RISC is poorly understood. One hypothesis was that SIDT-1 mediated the delivery. It was demonstrated that SIDT-1 knockdown or inhibition with an antibody blocked cholesterol-siRNA uptake in cultured cells, suggesting that SIDT-1 was involved in the cellular internalization (Wolfrum et al., 2007).

SIDT-1 has been shown to be a potentially important regulator of conjugate siRNA delivery, thus in this chapter I investigated if either one or both the human SIDT-1 and SIDT-2 proteins were capable of dsRNA uptake in human cells. In addition, I attempted to purify the large extra cellular domain of SIDT-1 to demonstrate that it interacted specifically with dsRNA *in vitro* (Figure 4.1).

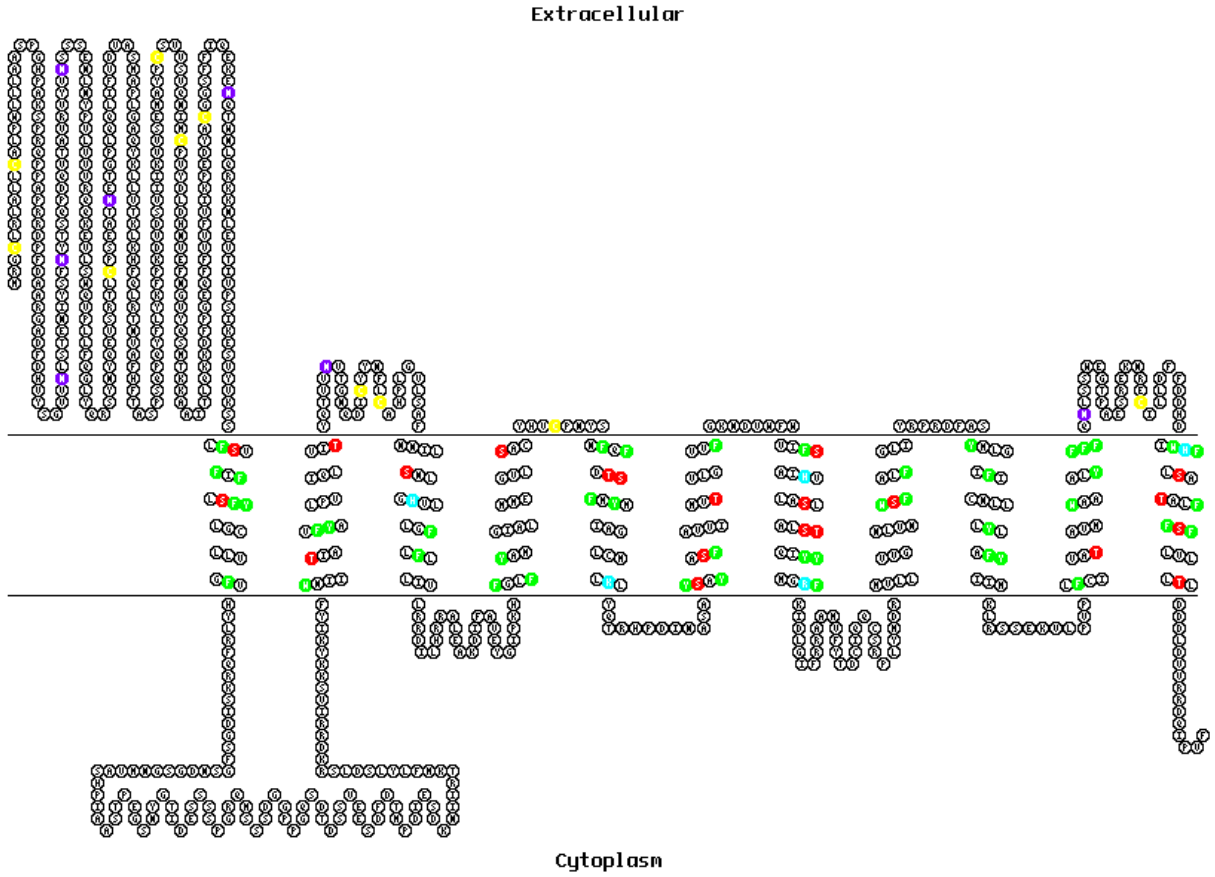

Figure 4.1 Predicted topology of SIDT-1.
Cys are yellow; N-glycosylation sites are purple; His, Lys, Arg are cyan; Tyr, Trp, and Phe are green; Thr, Ser are red.

4.2 Methods

4.2.1 Cell Culture

MCF-7 and HeLa-Luc were maintained in T75 flasks between 10-90% confluence (100% confluent T75 yields ~10 x 10^6 total cells) in RPMI 1640 supplemented with 10% heat inactivated FBS (Gibco, Life Technologies, Benicia, CA) and 25 mM HEPES in a humidified atmosphere with 5% CO_2 at 37 ^oC.

4.2.2 Materials

All cell culture reagents were supplied by the UCSF Cell Culture Facility. siRNA against luciferase (sense: 5'-GCUACAUUCUGGAGACAUATT; antisense: 5'-UAUGUCUCCAGAAUGUAGCTT) and a nonspecific control (NS) (5'-UGGUUUACAUGUCGACUAAUU and 5'-UUAGUCUACAUGUAAACCAUU) used for *in vitro* knockdown experiments was provided by Pfizer (Cambridge, MA). SIDT-1 siRNA (sense: 5'-UGAUAAAGCCUGAAGAUUATT; antisense: 5'-UAAUCUUCAGGCUUUAUCATT) and all oligos were purchased from Integrated DNA Technologies (San Diego, CA). 500 bp dsRNA was synthesized by amplifying a 500 bp fragment of luciferase from pGL3 (Promega, Madison, WI) with primers 5'- TAATACGACTCACTATAGGGCGGAGTTCATGATCAGTGC and 5' - TAATACGACTCACTATAGGGCCTGGTTCCTGGAACAATTGC that have T7 promoters incorporated at the 5' ends. The DNA PCR product was then used as template for reverse transcription using T7 High Yeild RNA Synthesis Kit from New England Biolabs (Ipswich, MA). The Steady-Glo luciferase assay kit was purchased from Promega (Madison, WI). All restriction enzymes were from New England Biolabs (Ipswich, MA). All constructs were confirmed by sequence analysis by McLab (South San Francisco, CA).

4.2.3 Cloning SIDT-1 and SIDT-2

Both SIDT-1 and SIDT-2 were cloned from cDNA obtained from OpenBiosystems (Thermo Fisher, Waltham, MA). SIDT-1: Clone ID: 40125773 Accession: BC117222 and SIDT-2 : Clone ID: 40035836 Accession: BC114522. SIDT-1 was amplified with Phusion DNA polymerase (New England Biolabs, Ipswich, MA) using 5'-AGGAGGGCCACCATGCGCGGCTGCCTGCGGCTC and 5'-AGCGAATTCTTATCCTCAGAAGACAGGGATCTGGTC primers. SIDT-2 was amplified with primers 5'-AGGAGGGCCACCATGTTCGCTCTGGGCTTGCCC and 5'-AGCGAATTCTTATCCTCAGAAGACATAGATCTTGTC. The PCR products were mixed with pORF-mcs (Invivogen, San Diego, CA) digested with NcoI and EcoRI using the CloneEZ kit from Genscript (Piscataway, NJ). Clones were confirmed to be correct by sequence analysis generating plasmids pSIDT-1 and pSIDT-2.

SIDT-1-GFP and SIDT-2-GFP were constructed by overlap PCR. The unfused coding sequences were amplified using primers 5'-AGGAGGGCCACCATGCGCGGCTGCCTGCGG and 5'-ACCACCACCGGAGCCACCACCACCGAAGACAGGGATCTGGTC to amplify SIDT-1, 5'-AGGAGGGCCACCATGTTCGCTCTGGGCTTGCCC and 5'-ACCACCACCGGAGCCACCACCACCGAAGACATAGATCTTGTC to amplify SIDT-2, and 5'-GGTGGCTCCGGTGGTGGTGGTTCCATGGTGAGCAAGGGCGAG and 5'-GAATTCTTATCCTCACTTGTACAGCTCGTCCAT to amplify GFP. The amplified SIDT products were mixed with the GFP product and re-amplified using the forward SIDT primer and the reverse GFP primer. The fused product was then cloned into pORF-mcs (Invivogen, San Diego, CA) digested with NcoI and EcoRI using the CloneEZ kit from Genscript (Piscataway,

NJ). Clones were confirmed to be correct by sequence analysis generating plasmids pSIDT-1-GFP and pSIDT-2-GFP.

SIDT-1 NTD was cloned into pET15b as a fusion to mKate with primers 5'-AGGAGGGCCACCATGAAGTTATACATGGAGGGT and 5'-GAATTCTTATCCTCAGTGATGATGATGATGATGTTTATGGCCCAGTTTAGA to amplify SIDT-1 NTD and 5'-TCGCACCCTGAAAATACAAATTCTCTTTATGGCCCAGTTTAGA and 5'-GGGGGAGGGGGTAGTCATCATCATCATCATCACTGAGGATCCGGCTGCTAA to amplify pET15b-mKate. The construct was cloned in using CloneEZ kit from Genescript (Piscataway, NJ). Clones were confirmed to be correct by sequence analysis generating plasmids pET15b-SIDT-1NTD.

4.2.4 *In Vitro* Knockdown of Luciferase

25,000 HeLa-Luc cells were seeded into each well of a 96-well plate and then transfected with 200 ng of plasmid DNA 6 hours later using 1 µL of Lipofectamine 2000 per well (Life Technologies, Grand Island, NY). 18 hours later the media was removed and replaced with serum free media containing 100 ng/mL siRNA against luciferase or a non-specific control. The cells were incubated for 5 hours followed by addition of serum and continued incubation for 18 hours. The cells were lysed and luciferase expression was measured using the Steady-Glo assay kit (Promega, Madison, WI). Luminescence was measured using an Infinite m1000 Pro microplate reader (Tecan, San Jose, CA).

4.2.5 Microscopy

30,000 HeLa-luc cells were seeded onto a coverslip bottom 35 mm dish at 10% confluence and

allowed to adhere for two days before transfection with pSIDT-1-GFP and pSIDT-2-GFP. 500 ng of plamid DNA was mixed with 3 μL of Lipofectamine 2000 and incubated with the cells for 24 hours. The media was changed and the cells were visualized on a Nikon Eclipse TS100 inverted microscope with a 40x oil objective and a B1-A HYQ FITC filter cube (Nikon, Melville, NY).

4.2.6 Expression and Purification of SIDT-1 NTD

ArcticExpress cells (Agilent Technologies, Santa Clara, CA) were transformed with pET15b-mKate-SIDT1NTD. A 10 mL overnight culture grown in terrific broth (TB) with 200 μg/mL ampicillin and 0.2% glucose at 37 °C was used to inoculate 1 L of TB containing 200 μg/mL ampicillin. The culture was grown until it reached an OD_{600} of 0.6, where it was cooled in ice water bath for 10 minutes and 100 mM isopropylthio-β-galactoside (IPTG) was added and the culture was grown overnight at 12 °C for 18 hours.

The cell pellet was collected by centrifugation at 4 °C for 30 minutes at 6,000 ×g. The cells were resuspended in 50 mL of PBS and frozen at -80 °C. The cells were thawed and 2 mg/mL of lysozyme, 1 mM dithiothreitol and 0.1% triton-X 100 was added and incubated at 4 °C shaking for 1 hour. The lysed cells were then sonicated until the solution was no longer viscous. The soluble fraction was separated by centrifugation at 4 °C for 30 minutes at 12,000 ×g. The supernatant was filtered through at 0.45 μm PES filter and applied to a Ni charged 1 mL HiTrap SP FF (GE Healthcare), equilibrated with 20 mM Tris pH 7.5. The column was washed with three column volumes each of 250 mM NaCl, 400 mM NaCl, 50 mM imidazole, and 100 mM imidazole all containing 20 mM Tris pH 7.5. Fractions were analyzed by 12% SDS-PAGE.

4.2.7 Gel Shift Assay

100 ng of either RNase III (1.5 pmoles), or mKate-SIDT-1 NTD (1.6 pmoles) was incubated with 250 ng of siRNA (17.9 pmoles) or 500 bp dsRNA (0.76 pmoles) for 30 minutes on ice and then crosslinked by UV treatment on ice for 15 minutes in the presence of 1 ng/μL methylene blue (Liu et al., 1996). The concentration of divalent cation was fixed at 50 mM, and the reactions were buffered to pH 7.5 with 50 mM Tris-HCl. siRNA was run in a 15% polyacrylamide TBE gel and 500 bp dsRNA was run in a 3% agarose TBE gel.

HeLa cells were transfected with pSIDT-1-GFP using conditions described for microscopy. The cells were then washed and incubated with 250 ng of 500 bp dsRNA in 1 mL of PBS on ice for 30 minutes and then crosslinked on ice for 15 minutes in the presence of 1 ng/μL methylene blue (Liu et al., 1996). The cells were then washed and lysed with cell culture lysis reagent (CCLR, Promega, Madison, WI). The lysate was run in a 12% SDS polyacrylamide gel and the fluorescence of GFP was visualized.

4.3 Results

4.3.1 Cloning SIDT-1 and SIDT-1

Five constructs were created for the expression of SIDT-1 and SIDT-2 in mammalian and bacterial cells (Figure 4.2). Full length SIDT-1 and SIDT-2 were cloned under a EF1α/HTLV promoter for constitutive and high levels of expression. In addition, GFP was fused in frame to the predicted cytoplasmic C-termini of SIDT-1 and SIDT-2, similar to what has been done before (Duxbury et al., 2005) with a glycine and serine linker to separate the proteins. Lastly, the large extracellular domain (Figure 4.1 - residues 26 - 310) lacking the signal sequence was cloned as a fusion to monomeric Katushka (mKate) separated by a TEV cleavable linker under

the control of the T7 promoter for high level expression in E. coli. The mKate fusion allowed for ease of purification and increased solubility and expression of the SIDT-1 domain.

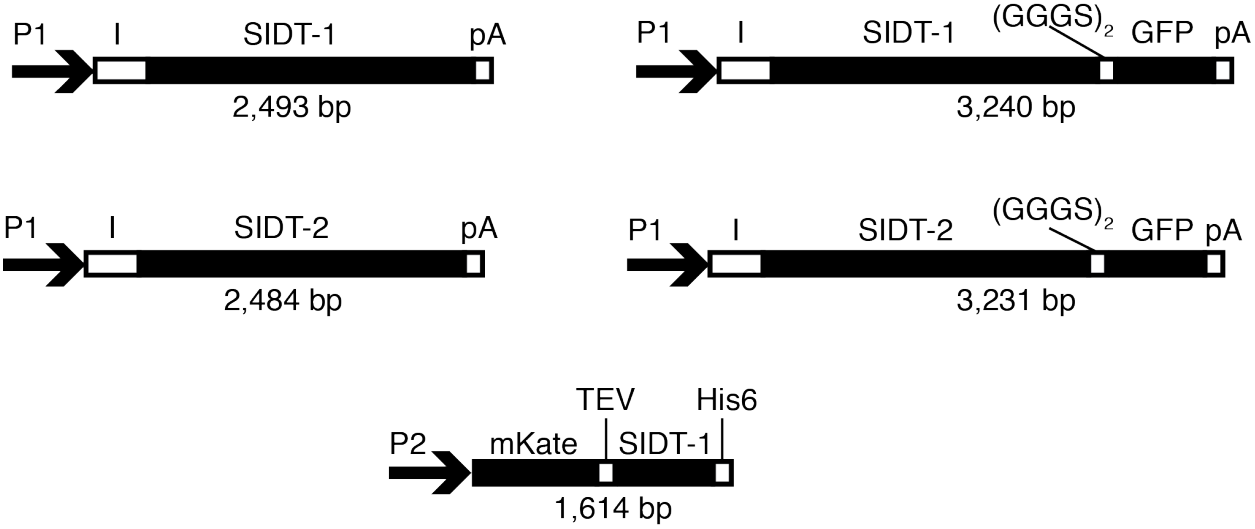

Figure 4.2 SIDT-1 and SIDT-2 plasmid constructs.
P1 is a composite Human Elongation Factor 1α and Human T-Cell Leukemia Virus promoter. I is an artificial intron containing a LacI regulated promoter for expression in E. coli. $(GGGS)_2$ is a tandem Gly-Gly-Gly-Ser linker. pA is the SV40 polyadenylation signal. P2 is the T7/lacO promoter. TEV is the tobacco etch virus protease sequence, ENLYFQG. His6 is the hexahistidine tag for Ni affinity purification.

4.3.2 SIDT-1 and SIDT-2 Mediated RNAi

SIDT-1 and SIDT-2 were tested in cultured cells for the ability to confer RNAi to exogenous siRNA added to the culture media. pSIDT-1 and pSIDT-2 were transfected into HeLa cells constitutively expressing firefly luciferase. 24 hours following transfection the media was replaced with serum free media containing 100 ng/mL siRNA. The siRNA was either a non-specific control or against luciferase. SIDT-1 conferred the ability to specifically knockdown luciferase expression, however, SIDT-2 did not (**Figure 4.3**). These results are similar to those observed with SIDT-1 and the *C. elegans* homolog (Duxbury et al., 2005; Feinberg and Hunter, 2003). There was modest, but insignificant knockdown of luciferase in cells transfected with a GFP expressing plasmid (pGFP). Because the effect size of knockdown was minimal and

trending towards significance with SIDT-2, transfections with more pDNA were performed to increase the expression. In these subsequent experiments the results were not significant (Figure 4.4). Specifically, luciferase siRNA was always able to knockdown even when pGFP was transfected. These data suggest the transfection agent (Lipofectamine 2000) was acting in trans to mediate transfection of the siRNA, masking uptake through the SIDT channels. Attempts to make cells stably expressing SIDT-1 and SIDT-2 were unsuccessful and further attempts to reproduce and improve the results shown in **Figure 4.3** were not performed. The expression levels of SIDT-1 in these experiments were not measured as we do not have an antibody against the SIDT-1 or SIDT-2.

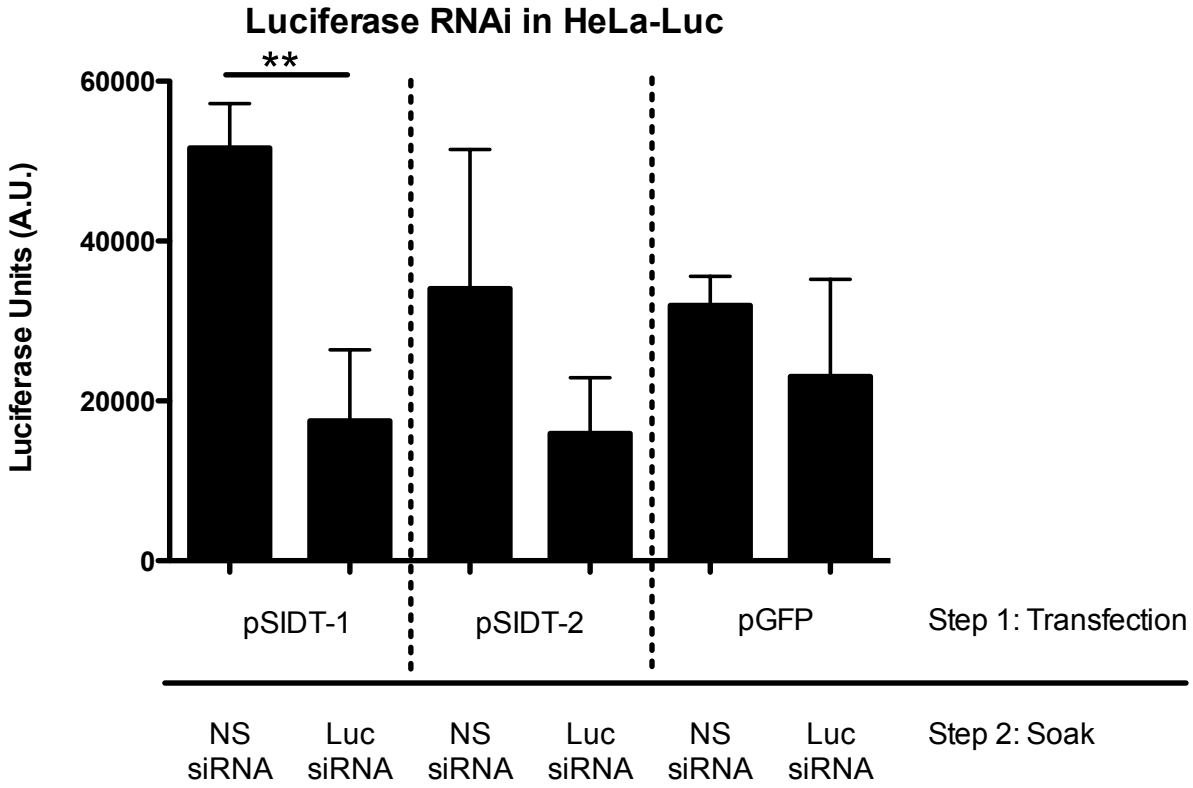

Figure 4.3 RNAi mediated by SIDT-1 and SIDT-2 in HeLa-Luc cells.
HeLa-Luc cells were first transfected with plasmids expressing SIDT-1, SIDT-2, or GFP (Step 1). 24 hours later, media was replaced with fresh media containing either non-specific (NS) or luciferase (Luc) siRNA (Step 2). Cells were assayed for luciferase activity. ** $p < 0.01$. Data are mean +/- S.D, n of 3 per group.

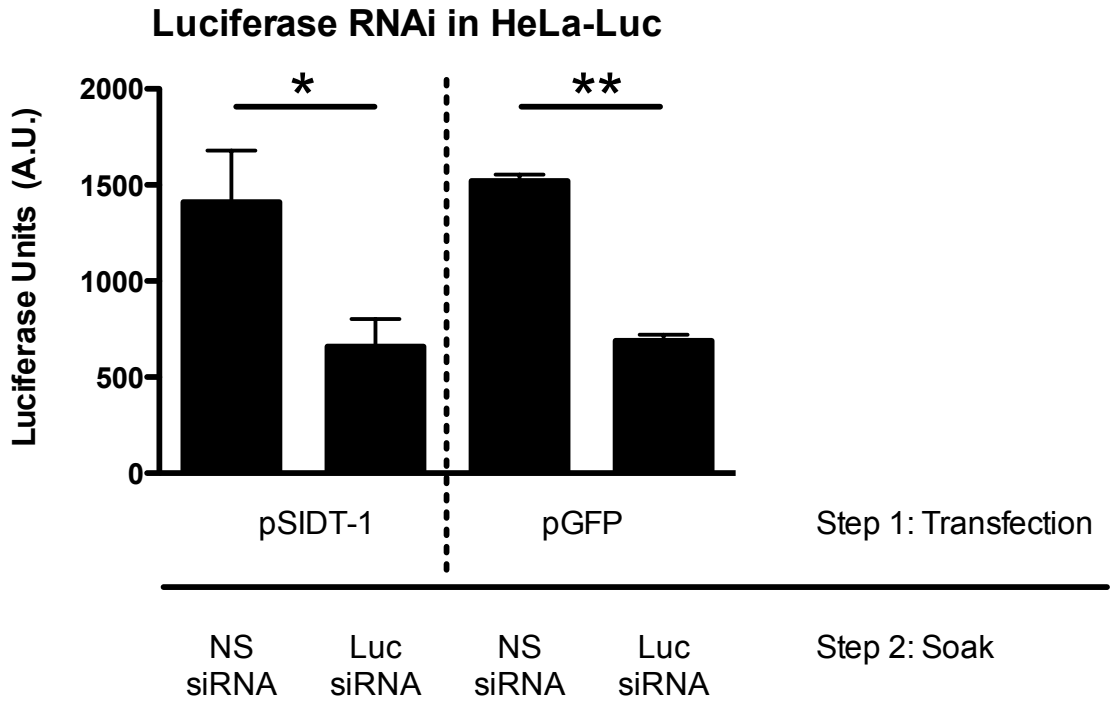

Figure 4.4 Repeat of RNAi mediated by SIDT-1 in HeLa-Luc cells.
As described for Figure 4.3 HeLa-Luc cells were transfected with plasmids expressing SIDT-1 or GFP (Step 1). 24 hours later, media was replaced with fresh media containing either non-specific (NS) or luciferase (Luc) siRNA (Step 2). Cells were assayed for luciferase activity. * $p < 0.05$. ** $p < 0.01$. Data are mean +/- S.D, n of 3 per group.

The breast cancer cell line, MCF-7, endogenously expresses SIDT-1 over 30 times the mean value for ~80 cell lines tested (Su et al., 2004). Consequently, the reverse experiment was tested in these cells, where firefly luciferase and either a non-specific or specific siRNA against SIDT-1 was transfected into the cells, which were then incubated in media containing luciferase siRNA (Figure 4.5). In this experiment, siRNA mediated knockdown of SIDT-1 inhibited the activity of siRNA against luciferase to accumulate in MCF-7 cells and cause knockdown of luciferase expression. These results indicate that SIDT-1 is involved in mediating an RNAi effect when siRNA is added to extracellular media.

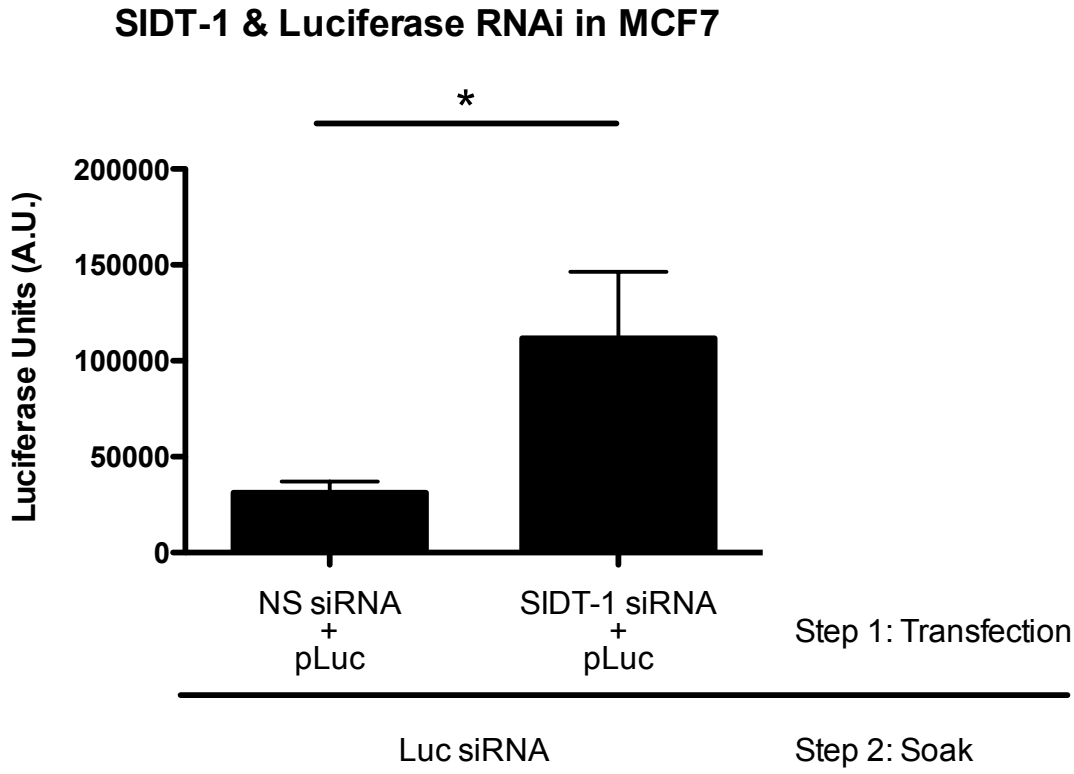

Figure 4.5 RNAi mediated knockdown of SIDT-1 in MCF-7 cells.
MCF-7 cells were first co-transfected with plasmids expressing pLuc and either non-specific (NS) or SIDT-1 siRNA (Step 1). 24 hours later, media was replaced with fresh media containing luciferase (Luc) siRNA (Step 2). Cells were assayed for luciferase activity. * $p < 0.05$. Data are mean +/- S.D, n of 3 per group.

4.3.3 SIDT-1 and SIDT-2 Cellular Localization

The plasmids pSIDT-1-GFP and pSIDT-2-GFP were transfected into HeLa-luc cells and visualized for cellular localization of SIDT-1 and SIDT-2 (Figure 4.6). In contrast to the cytoplasmic localization of GFP, SIDT-1 localized primarily to internal membranes consistent with the Golgi apparatus and endoplasmic reticulum. SIDT-2 however, was poorly transfected and expressed in a minority of cells. In the cells that did express high levels of SIDT-2, the localization was similar to SIDT-1 but with more pronounced nuclear membrane staining. The localization patterns of SIDT-1 and SIDT-2 are consistent with membrane bound proteins. Although the majority of the protein is localized in internal membranes there is presumably

enough plasma membrane localization to mediate its effect.

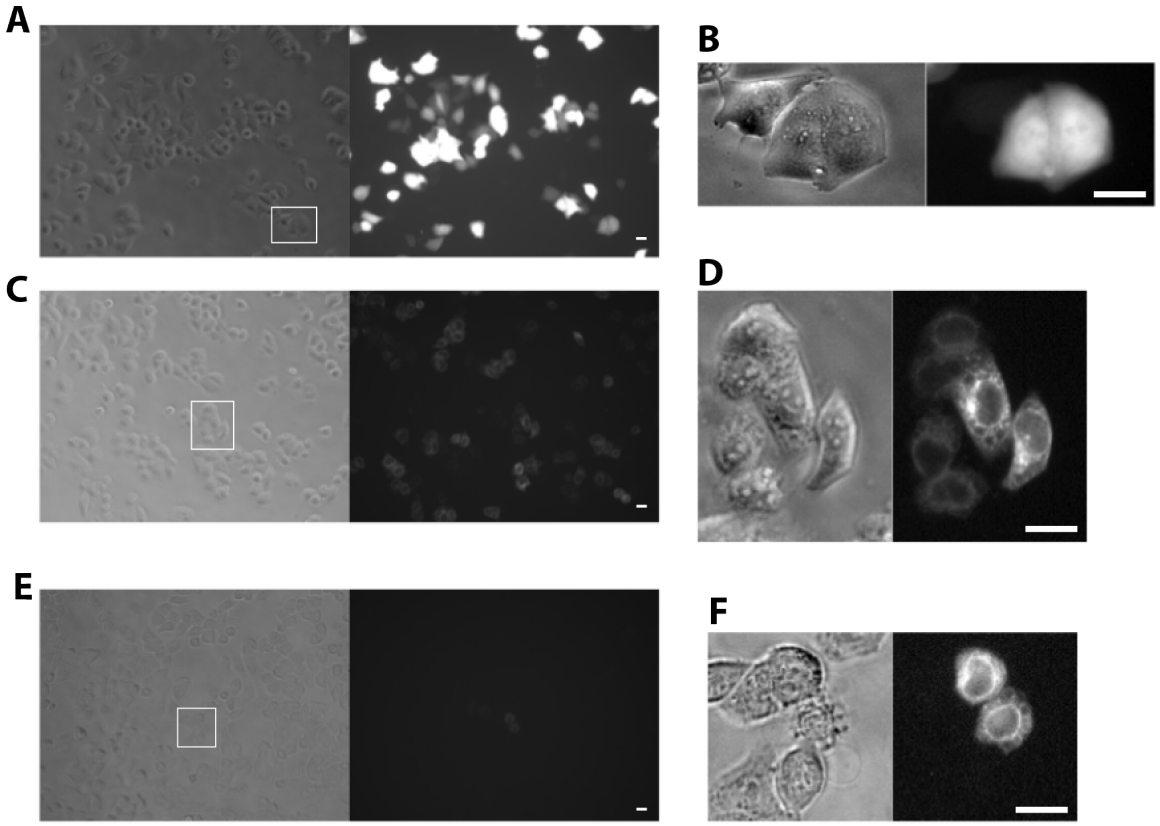

Figure 4.6 Cellular localization of pSIDT-1-GFP and pSIDT-2-GFP in HeLa cells.
Bright field and fluorescent images of HeLa cells transfected with pGFP (A), pSIDT-1-GFP (C), and pSIDT-2-GFP (E). Images in B, D, and F are blown up regions A, C, and E, respectively, indicated by the white box in the corresponding bright field image. Images were taken with a 40x objective and scale bars represent 20 µm in all images.

4.3.4 Expression and Purification of SIDT-1 N-Terminal Domain

SIDT-1 is hypothesized to be a dsRNA channel, however, it does not have a predicted dsRNA binding domain. Exactly how the protein interacts with and is specific for dsRNA is poorly understood. The function of the protein in mediating cellular uptake of dsRNA, suggests that much of the discrimination and recognition of dsRNA likely resides in the large N-terminal extracellular domain (NTD, Figure 4.1). Consequently, this domain was cloned into an *E. coli* pET vector to achieve high levels of expression. To facilitate identification and purification of the domain, the far-red fluorescent protein mKate was fused to the N-terminus of the protein,

separated by a TEV cleavable linker. Initial expression attempts in BL21 RIPL yielded inclusion body accumulation of the NTD and refolding attempts were poorly successful.

ArcticExpress cells were used for expression, which allow for increase soluble yields of proteins by expression at reduced temperature (12 °C) in the presence of cold adapted chaperones, Cpn10 and Cpn60, from *O. antarctica*. Expression in this host allowed for significant soluble expression of the mKate-SIDT-1 NTD fusion (Figure 4.7A and Figure 4.7C Lane 1). Interestingly, a significant amount of mKate lacking any apparent SIDT-1 NTD was also observed (lower band Figure 4.7C lane 1).

After Ni affinity purification of the soluble protein, pure protein was obtained as determined by Coomassie stain and consistent with the expected molecular weight of 61 kDa (Figure 4.7B lanes 14-17). In the purified mKate-SIDT-1NTD lanes a clear dimer was observed suggesting that SIDT-1 multimerizes. It is unlikely that the dimer is a result of the mKate fusion as the protein has 4 mutations making mKate monomeric at concentrations as high at 10 mg/mL (Shcherbo et al., 2007).

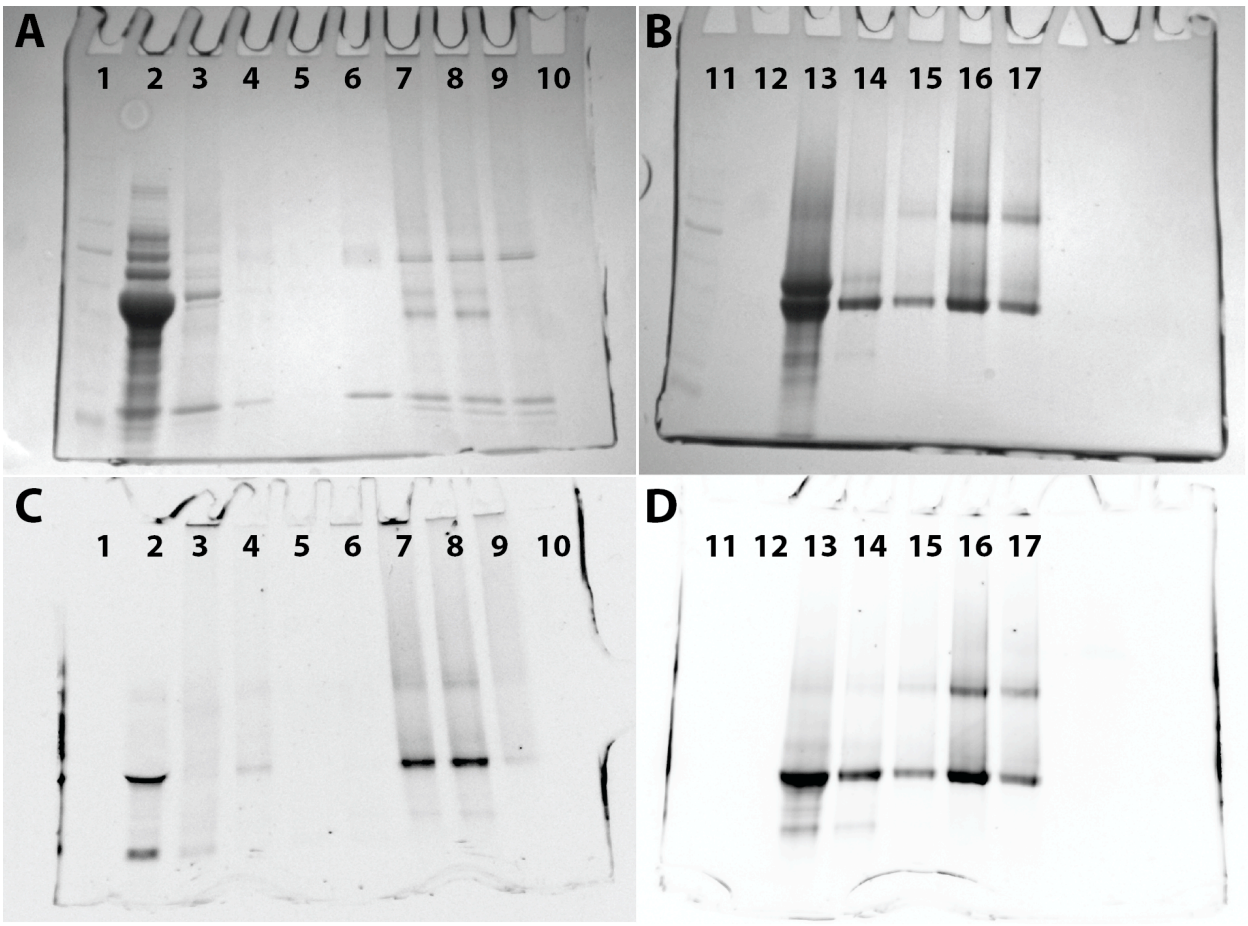

Figure 4.7 Purification of mKate-SIDT-1 N-terminal domain.
A and B are Coomassie stained gel images. C and D are mKate fluorescence images. Lanes 1 ad 11 are protein ladder. Lane 2 is the soluble *E. coli* lysate. Lanes 3-6 are deoxycholate extractions of the insoluble lysate. Lanes 7-9 are SDS extractions of the insoluble lysate. Lanes 10 and 12 are 250 mM and 400 mM NaCl washes of the Ni column. Lanes 13-15 are 50 mM imidazole elutions and lanes 16 and 17 are 100 mM imidazole elutions from the Ni column.

4.3.5 Interaction of SIDT-1 NTD with dsRNA *in vitro*

The purified SIDT-1 NTD was tested for interaction with dsRNA by a gel shift assay. Two dsRNA substrates were tested, a 500 bp dsRNA and a 21 bp siRNA were selected as SID-1 has been shown to be a specific transporter of dsRNA regardless of size (Shih et al., 2009). In addition, the larger 500 bp dsRNA would make for a more apparent gel shift if weak interactions were occurring. Protein and RNA complexes were crosslinked by UV treatment with methylene blue prior to electrophoresis to ensure that stable complexes were formed (Liu et al., 1996).

Since many nucleic acid binding proteins require divalent cations not only for catalysis but also binding, Mn, Ni, Zn, Ca, and Mg were tested (data shown for Ca and Mg). *E. coli* RNase III showed a clear gel shift of the 500 bp dsRNA in the presence of Ca, which allows for binding, but not catalysis (Campbell et al., 2002). (Figure 4.8A, lane 2). However, RNase III did not show an apparent shift in the siRNA as it cleaves dsRNA to products between 13-24 bp and binds weakly to these sized products (Ji, 2008).

In contrast to RNase III, SIDT-1 NTD did not appear to alter the mobility of either the 500 bp dsRNA or the siRNA (Figure 4.8A, lanes 3-4; Figure 4.8B, lanes 4-6) suggesting that the protein does not interact with dsRNA directly. Addition of divalent cation did not alter the ability of SIDT-1 NTD to interact with dsRNA (Figure 4.8A, lanes 3-4; Figure 4.8B, lanes 5-6). These gel shift experiments were performed at a 10:1 molar ratio of siRNA to protein and 1:2 molar ratio of dsRNA to protein and alteration of the nucleic acid to protein ratios did not alter the results (data not shown).

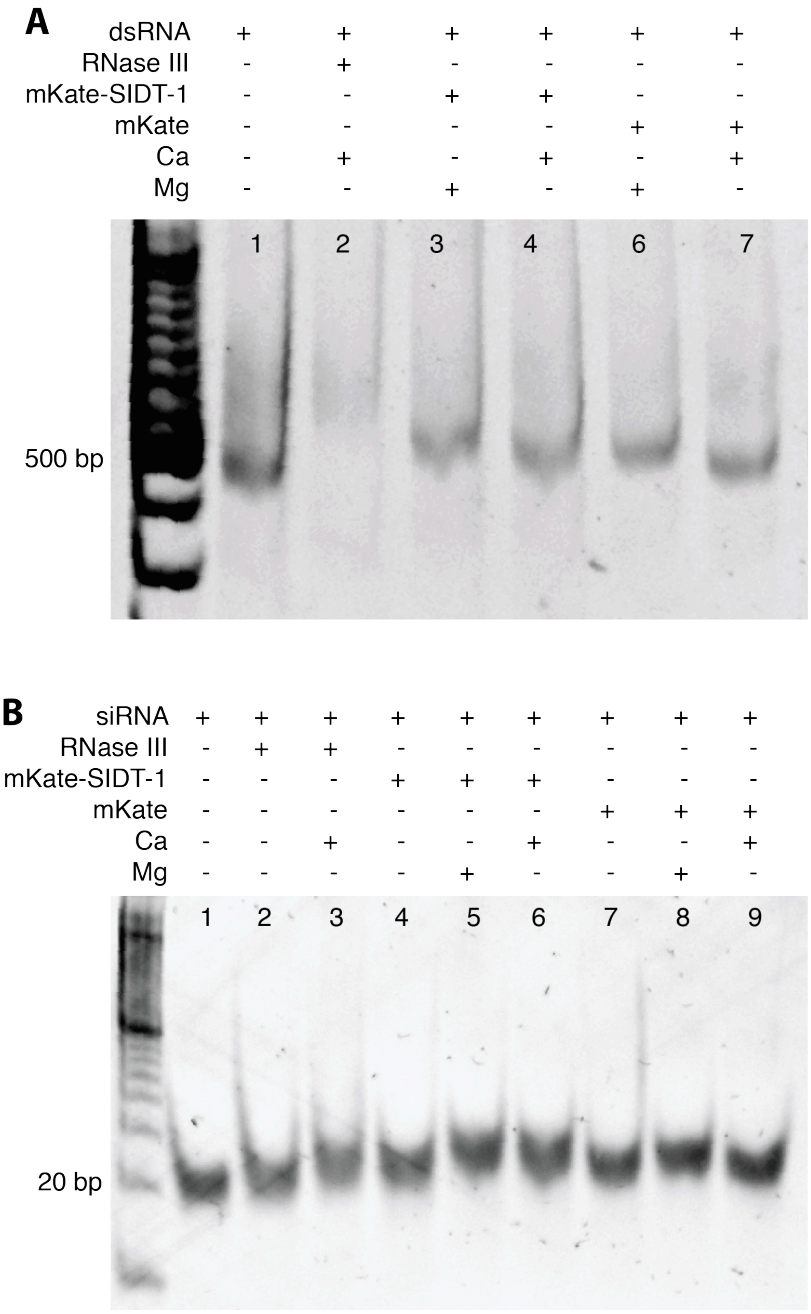

Figure 4.8 Gel shift assays for SIDT-1 NTD interaction with dsRNA.
Fixed concentrations of protein and dsRNA (A), or siRNA (B) were incubated in the presence of divalent cations Ca and Mg then crosslinked by UV and run on a 3% agarose gel (A) or a 15% polyacrylamide gel (B).

The shift in mobility of SIDT-1 NTD was also investigated using the mKate fluorescence. In these assays, both the dsRNA and protein can be simultaneously visualized with the protein migrating towards the cathode and the nucleic acid migrating towards the anode (Figure 4.9A

and B). In these experiments both mKate and mKate-SIDT-1 NTD altered the mobility of dsRNA in the presence of Mn (Figure 4.9A and B, lanes 4-6), but not Ca and Mg (data not shown). The interaction was pH dependent occurring at pH 6, but to a lesser degree at pH 7.5 and 10 (data not shown) indicating that the effect was due to protonation of the hexahistidine tag and coordination of Mn. These data provide further evidence that SIDT-1 NTD does not directly interact with dsRNA.

Finally, full length SIDT-1-GFP was assayed for interaction with dsRNA, by transfecting HeLa cells with pSIDT-1-GFP and after 24 hours post transfection the cells were washed with PBS and exogenous extracellular 500 bp dsRNA was added and crosslinked using methylene blue. The membrane fraction was then run on native SDS-PAGE and SIDT-1-GFP was visualized (Figure 4.9C). These experiments indicate that SIDT-1 in the context of the entire protein with native glycosylation does not interact with dsRNA as there is no upward mobility shift in SIDT-1-GFP when incubated with dsRNA and crosslinked compared to its mobility in the absence of dsRNA and/or the crosslinking agent methylene blue. It is possible that endogenous dsRNA is already bound and subsequently crosslinked, however, the cells were extensively washed with PBS prior to addition of exogenous extracellular dsRNA and the SIDT-1-GFP band in the absence of additional dsRNA does not appear as a smear, which would be expected in endogenous dsRNA of various sizes were bound and crosslinked.

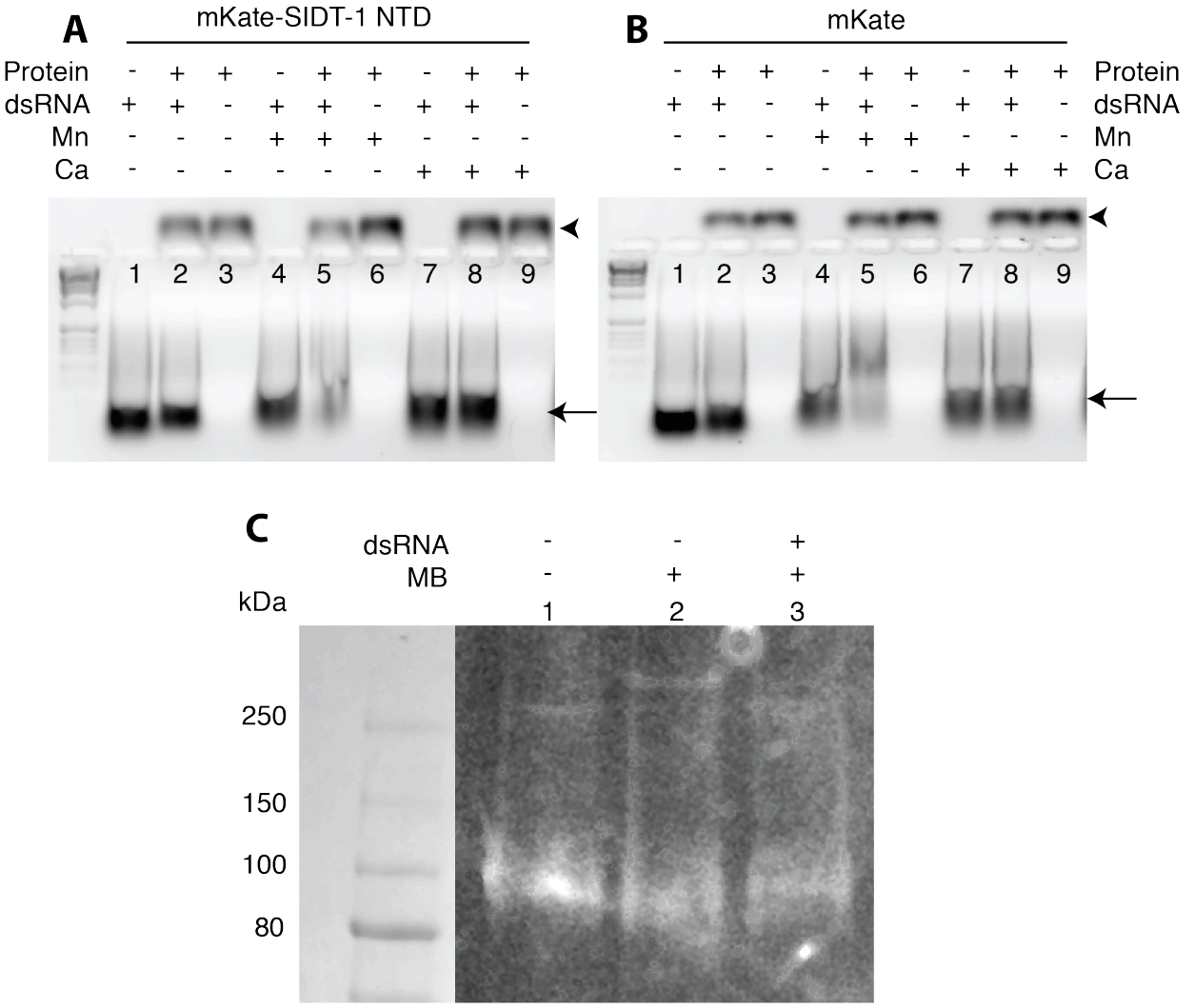

Figure 4.9 dsRNA and protein gel shift assay for SIDT-1 NTD and full length SIDT-1 interaction with dsRNA.

mKate-SIDT-1 NTD (A) and mKate (B) were incubated in the presence of Mn or Ca at pH 6 then crosslinked by UV and run on a 5% agarose gel. The arrow head indicates the mKate protein fluorescence above the well and the arrow indicates the dsRNA. C) HeLa cells expressing full length SIDT-1-GFP was incubated in the presence or absence of a large excess of dsRNA with or without methylene blue (MB).

4.4 Conclusion

The ability of SIDT-1 to mediate the cellular uptake of siRNA into mammalian cells has been replicated by several groups including ours (Figure 4.3 and Figure 4.5) (Duxbury et al., 2005; Feinberg and Hunter, 2003). However, the effect is dependent upon a special condition when the protein is over expressed and likely artifactually localized at the plasma membrane. This occurs

in cancer cells as indicated by the marked over expression of SIDT-1 in MCF-7 cells. However, the MCF-7 cell line is the only line in ~80 human and mouse cancer lines tested that over express SIDT-1 (Su et al., 2004). Thus, the extent to which SIDT-1 is mis-regulated in the progression of cancer *in vivo* is unknown and probably minimal as is how it contributes to cellular transformation. In addition, because it is selective for dsRNA, modifications to make naked siRNA more serum stable would likely abolish the SIDT-1 dependent transport rendering this mode of delivery useless for therapy. In addition, the ability to knockdown gene expression via SIDT-1 in cultured cells requires ~100-fold more siRNA than can be achieved by other transfection methods. Thus while SID-1 is important for the systemic response to RNAi in *C. elegans*, it is a highly unlikely mechanism for siRNA delivery in Humans.

However, the exact role SIDT-1 and SIDT-2 play in mammals is yet to be uncovered. From microscopy evidence it appears to be localized primarily to membranes inside the cell consistent with the ER, Golgi, and the nuclear membrane (Figure 4.6). This localization pattern indicates that SIDT-1 is involved in intracellular transport of dsRNA. The involvement of SIDT-1 in the cellular delivery of cholesterol-siRNA suggests that SIDT-1 is active in endosomal compartments to mediate the cytoplasmic delivery of such siRNA conjugates (Wolfrum et al., 2007). Thus for this method of siRNA delivery SIDT-1 has an observed role. These data taken together suggest that SIDT-1 might play an endogenous role in the innate immune response to long dsRNA and viral infection. Many more studies will have to be performed before the biological function of SIDT-1 will be uncovered.

As with any developing story, there are currently inconsistencies in SIDT-1 transport. The most

glaring is how SIDT-1 is gated by dsRNA. SIDT-1 appears to be the only protein required for its function as expression of SID-1 in *D. melanogaster* is sufficient for dsRNA uptake into S2 cells (Feinberg and Hunter, 2003). Because *D. melanogaster* does not have a sid-1 homologue, there is likely no other protein that is involved in regulating SID-1 gating, although this cannot be stated with complete certainty. While it is possible that a small molecule can act as an allosteric gate, the dsRNA itself seems to be the key to opening up the SID-1 channel (Shih et al., 2011). However, neither SID-1 nor either of the mammalian homologues have a dsRNA binding domain. Further, I found no evidence that the large extracellular domain of SIDT-1 is able to interact with dsRNA *in vitro* (Figure 4.8 and Figure 4.9). However, the SIDT-1 extracellular domain did dimerize suggest that it is involved in the quaternary structure of the protein. This observation is consistent with the tetramers that were observed upon reconstitution of SIDT-1 extracellular domain (Pratt et al., 2012). Thus the selectivity for dsRNA is likely mediated by the quaternary structure of SIDT-1.

The SID-1 family of proteins presents a novel mechanism for siRNA delivery. It will be interesting to see if and how this family of proteins can be utilized for therapy and more importantly what role these proteins play in mammalian biology. For the delivery aspect, there are more efficient mechanisms to get siRNA into cells at concentrations 1000-fold less than the concentrations that not only I, but others have observed and reported, however, the other delivery mechanisms are also frequently toxic. siRNA conjugates, while less potent, may be a safer technology in the long run for treating chronic diseases. The involvement of SIDT-1 in cellular uptake of siRNA conjugates may be an important step by which efficiency can be increased or a limit that cannot be bypassed. In addition, the endogenous role of SIDT-1 in biological processes

may uncover new areas of therapy that can be exploited, for example in viral infection and immunology. With the ever-expanding roles of RNA in biological regulation the proteins involved in communicating those messages will be critical to our understanding of the whole process.

4.5 References

Campbell, F.E., Cassano, A.G., Anderson, V.E., and Harris, M.E. (2002). Pre-steady-state and stopped-flow fluorescence analysis of Escherichia coli ribonuclease III: insights into mechanism and conformational changes associated with binding and catalysis. J Mol Biol *317*, 21–40.

Duxbury, M.S., Ashley, S.W., and Whang, E.E. (2005). RNA interference: a mammalian SID-1 homologue enhances siRNA uptake and gene silencing efficacy in human cells. Biochem Biophys Res Commun *331*, 459–463.

Elbashir, S.M., Harborth, J., Lendeckel, W., Yalcin, A., Weber, K., and Tuschl, T. (2001a). Duplexes of 21-nucleotide RNAs mediate RNA interference in cultured mammalian cells. Nature *411*, 494–498.

Elbashir, S.M., Lendeckel, W., and Tuschl, T. (2001b). RNA interference is mediated by 21- and 22-nucleotide RNAs. Genes Dev *15*, 188–200.

Feinberg, E.H., and Hunter, C.P. (2003). Transport of dsRNA into cells by the transmembrane protein SID-1. Science *301*, 1545–1547.

Fire, A., Xu, S., Montgomery, M.K., Kostas, S.A., Driver, S.E., and Mello, C.C. (1998). Potent and specific genetic interference by double-stranded RNA in Caenorhabditis elegans. Nature *391*, 806–811.

Hanss, B., Leal-Pinto, E., Bruggeman, L.A., Copeland, T.D., and Klotman, P.E. (1998). Identification and characterization of a cell membrane nucleic acid channel. Proc Natl Acad Sci USA *95*, 1921–1926.

Hanss, B., Leal-Pinto, E., Teixeira, A., Christian, R.E., Shabanowitz, J., Hunt, D.F., and Klotman, P.E. (2002). Cytosolic malate dehydrogenase confers selectivity of the nucleic acid-conducting channel. Proc Natl Acad Sci USA *99*, 1707–1712.

Ji, X. (2008). The mechanism of RNase III action: how dicer dices. Curr Top Microbiol Immunol *320*, 99–116.

Kizana, E., Cingolani, E., and Marbán, E. (2009). Non-cell-autonomous effects of vector-expressed regulatory RNAs in mammalian heart cells. Gene Ther *16*, 1163–1168.

Liu, Z., Wilkie, A., Clemens, M., and Smith, C. (1996). Detection of double-stranded RNA-protein interactions by methylene blue-mediated photo-crosslinking. Rna *2*, 611–621N1–.

Lorenz, C., Hadwiger, P., John, M., Vornlocher, H.-P., and Unverzagt, C. (2004). Steroid and lipid conjugates of siRNAs to enhance cellular uptake and gene silencing in liver cells. Bioorg Med Chem Lett *14*, 4975–4977.

MacKellar, C., Graham, D., Will, D.W., Burgess, S., and Brown, T. (1992). Synthesis and physical properties of anti-HIV antisense oligonucleotides bearing terminal lipophilic groups. Nuc Acid Res *20*, 3411–3417.

Mohr, D., Frey, S., Fischer, T., Güttler, T., and Görlich, D. (2009). Characterisation of the passive permeability barrier of nuclear pore complexes. Embo J *28*, 2541–2553.

Nakayama, T., Butler, J.S., Sehgal, A., Severgnini, M., Racie, T., Sharman, J., Ding, F., Morskaya, S.S., Brodsky, J., Tchangov, L., et al. (2012). Harnessing a physiologic mechanism for siRNA delivery with mimetic lipoprotein particles. Mol Ther *20*, 1582–1589.

Pratt, A.J.A., Rambo, R.P.R., Lau, P.-W.P., and MacRae, I.J.I. (2012). Preparation and characterization of the extracellular domain of human Sid-1. PLoS ONE *7*, e33607–e33607.

Rappaport, J., Hanss, B., Kopp, J.B., Copeland, T.D., Bruggeman, L.A., Coffman, T.M., and Klotman, P.E. (1995). Transport of phosphorothioate oligonucleotides in kidney: implications for molecular therapy. Kidney Int *47*, 1462–1469.

Shcherbo, D., Merzlyak, E.M., Chepurnykh, T.V., Fradkov, A.F., Ermakova, G.V., Solovieva, E.A., Lukyanov, K.A., Bogdanova, E.A., Zaraisky, A.G., Lukyanov, S., et al. (2007). Bright far-red fluorescent protein for whole-body imaging. Nat Methods *4*, 741–746.

Shih, J.D., Shih, J.D., Hunter, C.P., and Hunter, C.P. (2011). SID-1 is a dsRNA-selective dsRNA-gated channel. Rna.

Shih, J.D., Fitzgerald, M.C., Sutherlin, M., and Hunter, C.P. (2009). The SID-1 double-stranded RNA transporter is not selective for dsRNA length. Rna *15*, 384–390.

Su, A.I., Wiltshire, T., Batalov, S., Lapp, H., Ching, K.A., Block, D., Zhang, J., Soden, R., Hayakawa, M., Kreiman, G., et al. (2004). A gene atlas of the mouse and human protein-encoding transcriptomes. Proc Natl Acad Sci USA *101*, 6062–6067.

Tijsterman, M., May, R.C., Simmer, F., Okihara, K.L., and Plasterk, R.H.A. (2004). Genes required for systemic RNA interference in Caenorhabditis elegans. Curr Biol *14*, 111–116.

Wolfrum, C., Shi, S., Jayaprakash, K.N., Jayaraman, M., Wang, G., Pandey, R.K., Rajeev, K.G., Nakayama, T., Charrise, K., Ndungo, E.M., et al. (2007). Mechanisms and optimization of in vivo delivery of lipophilic siRNAs. Nat Biotechnol *25*, 1149–1157.

Zhao, C., Tampé, R., and Abele, R. (2006). TAP and TAP-like--brothers in arms? Naunyn Schmiedebergs Arch Pharmacol *372*, 444–450.

Chapter 5 : Conclusions

5.1 Overview

The focus of my PhD research has been to integrate biology with non-viral siRNA delivery. Much of what is done in this field is synthesis of new lipids and characterization of the potency of delivery *in vitro* and *in vivo*. However, I chose to investigate if cells process lipid formulations differentially and if that can explain why some formulations are better than others at transfecting siRNA. In addition, I am also interested in endogenous mechanisms of dsRNA transport and chose to investigate a dsRNA transporter that was discovered in *C. elegans* and has a Human homologue. I believe that a more through understanding of how cells transport RNA, both endogenously and using synthetic non-viral vectors is key to furthering the field and making the systems developed thus far more potent and less toxic.

5.2 Summary of Findings and Future Directions

In this dissertation, I present evidence that cells traffic lipid-based nanoparticles differentially dependent upon lipid formulation. The results indicate that the recycling endosome and multivesicular bodies are important subcellular compartments to which nanoparticles delivering siRNA should be targeted for improved efficiency. In addition, I also investigated the ability of the dsRNA transporter, SIDT-1, to interact with dsRNA directly and found no such evidence for a direct interaction with the large extracellular domain.

In Chapter 2, I describe the creation and characterization of HeLa cells expressing endosomal markers fused to mTurquoise in inducible lentiviral constructs. The cells behaved as expected from studies done with similar constructs made with different fluorescent proteins. I also

describe the calibration of ratiometric fluorescent microscopy to determine endosomal pH. Lastly, I describe the image processing workflow that was created to colocalize labeled endosomes and lipid nanoparticles encapsulating siRNA.

Building upon the work in Chapter 2, I used the tools developed to investigate how the cell traffics three distinct lipid formulations for delivery of siRNA in Chapter 3. I found that a formulation containing the lipid DOTAP transfects siRNA into cells the best, and exhibits increased colocalization with recycling endosomes and multivesicular bodies. In addition, this formulation exists in endosomes with a average pH of ~5.2 consistent with the increased recycling compartment colocalization. Lastly, DOTAP accumulates in lysosomes slower than the other formulations tested. Combined, these characteristics provide a cellular signature for a well transfecting lipid formulation. In contrast, the other formulations tested did not demonstrate such distinct subcellular localization. Lastly, no formulation displayed a preference for utilizing clathrin-, caveolin-, or flotillin-dependent internalization pathways.

Chapter 4 describes investigations of an alternative pathway for cellular delivery of siRNA that utilizes a dsRNA specific transporter, SIDT-1. We confirmed the ability of cells to take up dsRNA when over expressing SIDT-1. We extended these studies to cells expressing SIDT-2 and found that this transporter was much less efficient at dsRNA transport that was partially explained by the much poorer expression of this protein. Lastly, I expressed and purified the large extracellular domain of SIDT-1 and investigated its ability to interact with dsRNA. We found no evidence for such an interaction suggesting that an alternative gaiting ligand might be utilized by SIDT-1.

Continued investigations into the cellular interactions of lipid-based nanoparticles will increase the potency of these systems and broaden the therapeutic applications. It will be interesting to see if the correlations uncovered in this thesis have a significant impact on how novel lipids or lipid formulations are identified as potent and efficient. In addition the ability to alter the trafficking of lipid formulations may allow for an alternative route to making poorly performing systems more potent as has been done for branched and linear PEI using Protein Kinase A inhibitors(ur Rehman et al., 2011). Lastly, the ability to target subcellular compartments, by distilling the complex architecture of viruses into simpler lipid-only systems with small molecule conjugates will be an interesting avenue for future development.

5.3 Long Term Outlook of siRNA Therapeutics

Macromolecular drug delivery is a challenging topic of research. We have attempted to engineer in the past 50 years what viruses have evolved to do over the course of billions of years. However, the latest systems for non-viral delivery of siRNA are effective in the clinic with an ED_{50} of 0.075 mg/kg at knocking down serum transthyretin and currently undergoing phase 2 trials by Alnylam. These systems have rapidly moved from the first published characterization of DLinDMA in 2005 (Heyes et al., 2005) to an optimized formulation that entered the clinic in 2010. Our understanding about how these lipid-based systems work is based upon the pH transitions during endocytosis and membrane biophysics. It was noted in the first study of these lipids that “events which have the greatest effect on the efficiency of gene-silencing occur once the siRNA has been internalized by the cell” (Heyes et al., 2005). Consequently, a through understanding of the cellular trafficking of nanoparticles is critical to developing better therapeutics.

There are several interesting siRNA delivery technologies that have been developed in the past decade including siRNA conjugates to cholesterol and GalNAc, the DLinDMA series of lipids, and more recently the use of exosomes to transfer siRNA (Alvarez-Erviti et al., 2011). As these technologies continue to be developed the most important hurdle to over come will be the ability to target tissues other than the liver. While the malignancies and disease affecting the liver amenable to RNAi therapeutics have not been exhausted, it will be important for expanding the biodistribution of RNAi therapeutics in the near future. Exosomes appear to be perfectly poised for the next phase of RNAi therapeutics delivery as they are an endogenous mechanism by which cells communicate and transfer nucleic acids among other macromolecules (Valadi et al., 2007). With new technologies that more completely integrate with and are routed in endogenous biological processes RNAi therapeutics will continue to be developed into a potent modality to treat and cure disease.

5.4 References

Alvarez-Erviti, L., Seow, Y., Yin, H., Betts, C., Lakhal, S., and Wood, M.J.A. (2011). Delivery of siRNA to the mouse brain by systemic injection of targeted exosomes. Nat Biotechnol.

Heyes, J., Palmer, L.R., Bremner, K., and Maclachlan, I. (2005). Cationic lipid saturation influences intracellular delivery of encapsulated nucleic acids. Journal of Controlled Release *107*, 276–287.

ur Rehman, Z., Hoekstra, D., and Zuhorn, I.S. (2011). Protein kinase A inhibition modulates the intracellular routing of gene delivery vehicles in HeLa cells, leading to productive transfection. Journal of Controlled Release *156*, 76–84.

Valadi, H., Ekström, K., Bossios, A., Sjöstrand, M., Lee, J.J., and Lötvall, J.O. (2007). Exosome-mediated transfer of mRNAs and microRNAs is a novel mechanism of genetic exchange between cells. Nat Cell Biol *9*, 654–659.

Appendix : Humanizing Cytosine Deaminase

A.1 Introduction

Prodrug therapy is a targeted technique to treat cancer whereby a targeted therapy converts a non-toxic prodrug into a cytotoxic drug. As a result, the toxic side effects are minimized by producing the cytotoxicity at the site needed rather than systemically. In addition, there is often an enhancement to the therapy caused of the "bystander effect", which involves an immune response to the primary tumor initiated by cytotoxic drugs (Gagandeep et al., 1996). 5-fluorocytosine (5-FC) combined with cytosine deaminase (CD) is one prodrug therapy that has shown promise. A gene encoding CD or the protein is delivered to cancer cells where it locally produces the cytotoxic drug 5-fluorouracil (5-FU) (Cunningham and Nemunaitis, 2001; Erbs et al., 2000; Ohwada et al., 1996; Park et al., 2009; Zhang et al., 2003).

Cytosine deaminase catalyzes the deamination of cytosine into uracil and ammonia and is involved in the pyrimidine salvage pathway in microbes (Figure A.1). The enzymatic activity is found in bacteria and fungi, but is believed to have evolved separately because of the significant structural differences between the two proteins. *E. coli* (bCD) and *S. cerevisiase* (yCD) have significant differences in their primary amino acid sequences, and quaternary structure with bCD being a hexamer and yCD a dimer (Ireton et al., 2002; 2003). In addition, the active sites of the two proteins are significantly different with more similarity observed between yCD and cytidine deaminases (CDA) from bacteria or humans (Costanzi et al., 2006; Ireton et al., 2003; Johansson et al., 2002). Despite the structural differences, both yCD and bCD are used in prodrug therapy with 5-FC, with yCD showing better efficacy because of its increased catalytic efficiency towards 5-FC (Kievit et al., 1999).

The main problem with using cytosine deaminase in prodrug therapy is that 5-FC is a poor substrate for CD and both the bacterial and fungal proteins are immunogenic. Despite yCD being more enzymatically efficient that bCD at producing 5-FU (Kievit et al., 1999), yCD still has a relatively poor catalytic efficiency of ~10^5 (M^{-1} s^{-1}) (Yao et al., 2005) that is four logs below the maximum for a diffusion limited enzyme. The ideal protein would have an increased catalytic efficiency towards 5-FC and come from a human origin. The closely related human cytidine deaminase (hCDA) is a good candidate for re-engineering to use 5-FC as a substrate, as the crystal structure has been solved and the active site has significant similarity to yCD (Figure A.2C)(Chung et al., 2005). Unfortunately, the protein is a tetramer and the active site is made from residues in three of the four monomers (Figure A.2). Thus, the re-engineering process is made extremely complex by the hCDA quaternary structure even though there is an abundance of structural data to rely upon when designing structural changes. In addition, a powerful mutagenesis technique, called recombineering, has been developed in *E. coli* that makes screening large libraries possible (Costantino and Court, 2003; Ellis et al., 2001), and has been successfully applied to large protein screens (Diner and Hayes, 2009; Valledor et al., 2012). Lastly, both yCD and bCD have been mutagenized and selected for increased catalytic efficiency for 5-FC and thermal stability (Fuchita et al., 2009; Mahan et al., 2004; Stolworthy et al., 2008) and similar selection conditions can be adopted for a screen for converting hCDA into hCD.

In this chapter, I first engineered a strain of *E. coli* that allowed for stringent selection conditions dependent upon CD activity and exhibited a high rate of recombination. Human cytidine deaminase was then moved onto the *E. coli* chromosome under the control of the *lacZ* promoter

and mutagenized with a randomizing oligo nucleotide. hCDA was mutated by insertion of two amino acids with concomitant randomization of four adjacent amino acids that are within a loop contacting the nucleoside binding site (Figure A.2B, arrow 2). This comprised a library size of 10^9 DNA molecules and $6.4*10^7$ mutant proteins. The aim was for the loop to extend into the nucleoside binding pocket and stabilize cytosine within the binding pocket. Unfortunately, no hCD activity was selected despite high levels of randomization at the target site. The inability to uncover hCD activity is likely due to high levels of suppresser mutants uncovered in the screen.

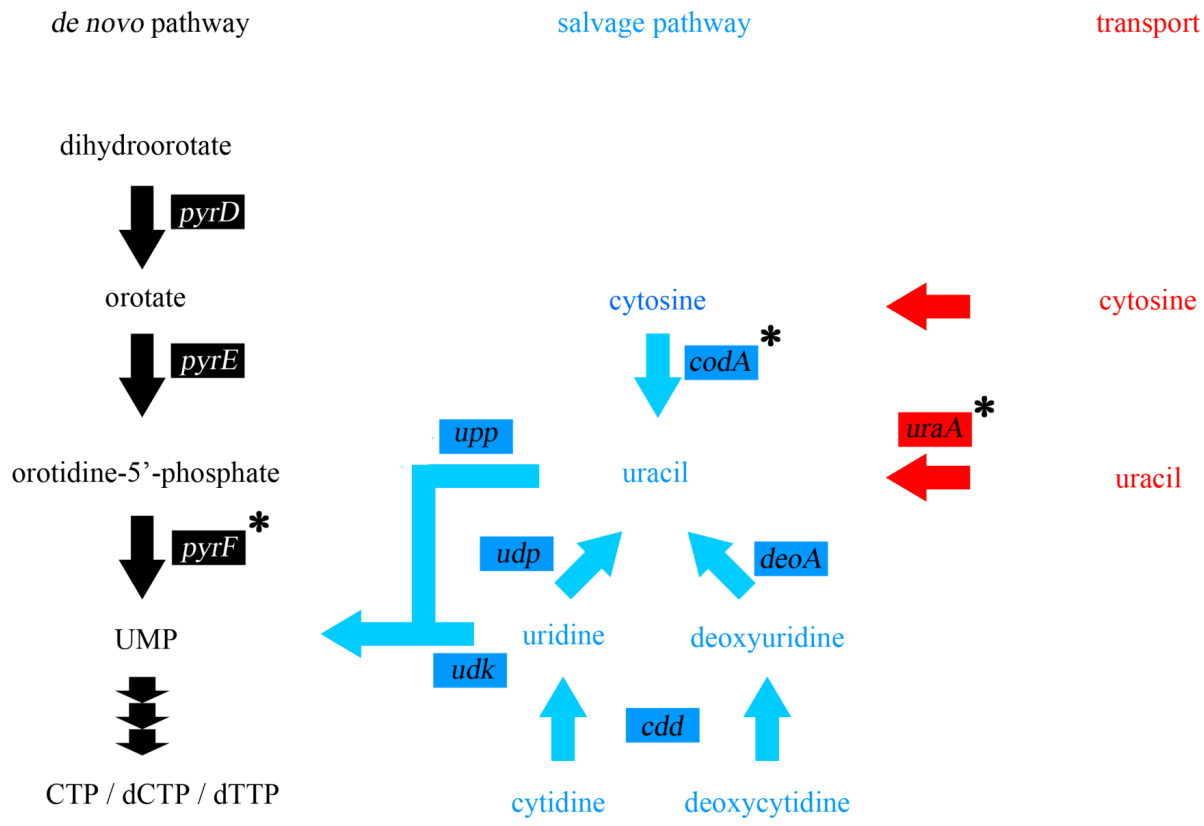

Figure A.1. Pyrimidine pathways in *E. coli*.
The *de novo* pathway, in black, is involved in synthesis of uridine monophosphate (UMP) and subsequent conversion into cytosine triphosphate (CTP) and thymidine triphosphate (TTP) and the deoxy- versions for DNA. The conversion of orotidine-5'-phosphate into UMP by *pyrF* is the ultimate step in the *de novo* pathway, prior to convergence with the salvage pathway. The salvage pathway, in blue, centers around uracil which is made from cytosine by the bacterial cytosine deaminase, *codA*. Lastly, transporters are involved in uptake of both cytosine and uracil from the surrounding media in red. The uracil transporter, *uraA* is indicated. A combined knockout of the three genes indicated by an asterisk are used in the selection strain.

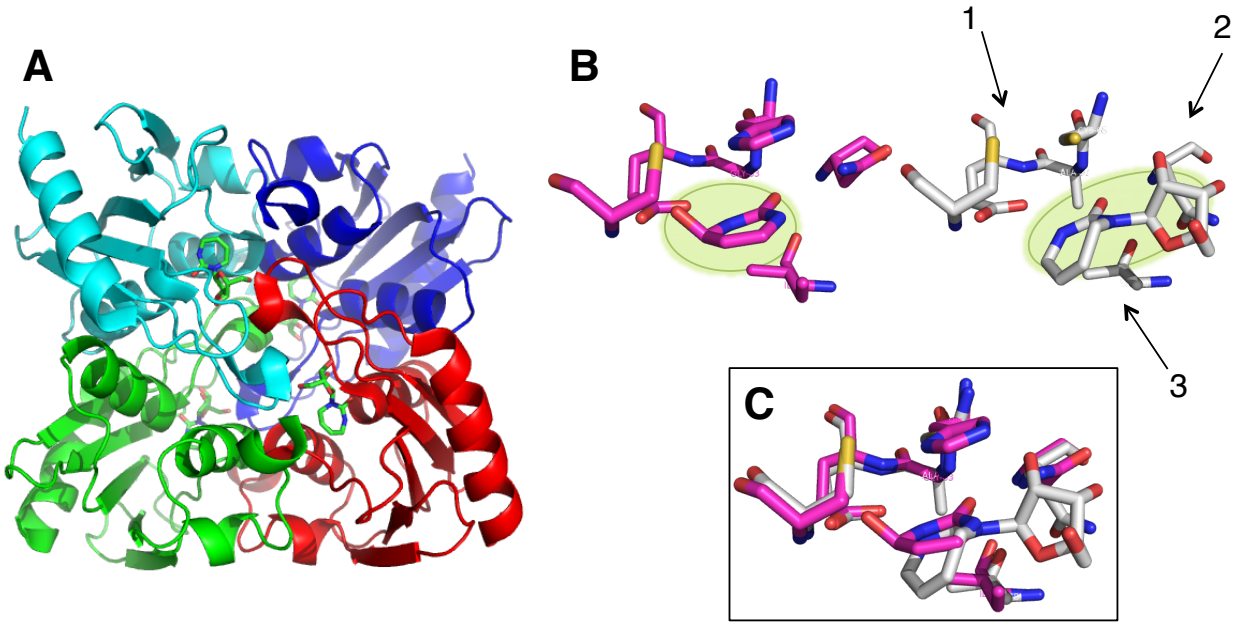

Figure A.2. Structure of human cytidine deaminase.
A) crystal structure of the hCDA tetramer with each monomer colored separately. B) Active site of yCD in purple and hCDA in white. yCD is bound to the active site inhibitor 4-[R]- hydroxyl-3,4-dihydropyrimidine (DHP), and hCDA is bound to the active site inhibitor diazeopinone riboside, both are outlined in green. For hCDA the residues that contribute to the active site are are from three different monomers indicated by the arrowed numbers. C) Overlap of the yCD and hCDA active sites. The structures are from PDB files 1P6O (yCD), and 1MQ0 (hCDA).

A.2 Methods

A.2.1 *E. coli* Strain Construction

Significant modifications to the *E. coli* chromosome were done in these studies based upon the Wanner method (Datsenko and Wanner, 2000). Briefly, a chloramphenicol or kanamycin resistance marker, flanked by Flp recombinase sites, Frt, is amplified by PCR from a set of plasmids (pKD3 and pKD4) using primers with ≥33 nucleotides of homology to the site of integration on the *E. coli* chromosome. The PCR product is then transformed into a strain such as BW25113 ($lacI^q$ $rrnB_{T14}$ $\Delta lacZ_{WJ16}$ *hsdR514* $\Delta araBAD_{AH33}$ $\Delta rhaBAD_{LD78}$) expressing the lambda red recombinase genes from plasmid pKD20. The resistance marker is used for selection and PCR, with a separate set of primers, can be used to ensure correct clones. The gene disruption can then be moved into other strains via P1 transduction and the resistance marker can

be removed by expressing Flp recombinase from plasmid pCP20. The following alleles were created using the primers listed in Table A.1: *lacZ*::hCDA, *lacZ*::yCD, and *hsdR*::cm. The *codA*::kan, *pyrF*::kan, *uraA*::kan, *galE::kan* and *mutS*::kan alleles were obtained from the Coli Genetic Stock Center (CGSC) with the strain numbers listed in Table A.2 (Baba et al., 2006). Mutations at *lacZ*, *hsdR*, and *codA* were confirmed by PCR with primers listed in Table A.3. The final strain used in the study is MT238 (MG1655 *hsdR pyrF uraA mutS codA*::kan *lacZ*::hCDA *nadA*::Tn10 λcI857 Δ(*cro-bioA*)), which was constructed by successively moving the *hsdR*::kan, *pyrF*::kan, *uraA*::kan, and *mutS*::cm alleles into MG1655 and removing the kanamycin or chloramphenicol resistance markers by Flp recombination. The lambda red recombinase genes linked to *nadA*::Tn10 were moved into the strain by P1 transduction from DY329 (Yu et al., 2000). Finally, the *lacZ*::hCDA allele was moved into the strain by P1 transduction using the linked *codA*::kan allele from strain MT184 (BW25113 *galE codA*::kan *lacZ*::hCDA).

A positive control strain was created that carried the *lacZ*::yCD allele, which was created by P1 transduction using the linked *codA*::kan allele from strain MT211 (BW25113 *galE codA*::kan *lacZ*::yCD). All strains constructed in this study are listed in Table A.4. When appropriate, the following antibiotics were used kanamycin (25 μg/mL), chloramphenicol (10 μg/mL), and tetracycline (10 μg/mL). All oligos were purchased from Integrated DNA Technologies (Coralville, IA), and all sequencing was done by McLab (South San Francisco, CA).

A.2.2 P1 Transductions

P1 lysates were created by growing the donor strain in Luria Broth (LB) media at 37 ^{o}C until OD_{600} of 0.2 was obtained. 5 mM $CaCl_2$ and 20 μL of a 10^9 plaque forming units (pfu) phage stock were added to the culture. The culture was grown at 37 ^{o}C until lysis occurred. Lysis was

completed by adding 100 µL of $CHCl_3$ with vigorous vortexing. The cell debris was removed by centrifugation for 10 minutes at 14,000 xg, and the supernatant was removed to a new tube containing 20 µL of $CHCl_3$ and stored at 4 °C.

P1 transductions were done by growing an overnight culture of the recipient strain in LB media at 37 ^{o}C. The cells were collected by centrifugation at concentrated 2-fold in MC buffer (10 mM $CaCl_2$ and 5 mM $MgSO_4$). 100 µL of cells and 100 µL of P1 lysate were combined (MOI of ~ 10 cells per phage), and incubated at 30 °C for 20 minutes. 1 mL of LB with 0.1 M Na-citrate was added to the culture followed by a 1 hour incubation at 37 °C. Transductants were selected by plating on LB agar plates with antibiotics and incubated overnight at 37 °C. Colonies were purified by re-streaking on selective LB agar plates.

A.2.3 *lacZ* Locus Selection

Strains wildtype for *lacZ* in a *galE* mutant background are unable to grow in the presence of 0.4% lactose or 0.1% phenylgalactoside as cells accumulate toxic levels of UDP-galactose (Gossen et al., 1992; Mientjes et al., 1994). However, mutation of the *lacZ* locus minimizes the cellular levels of galactose and cells can grow. Thus mutations at the *lacZ* locus can be selected for using M9 minimal media agar plates supplemented with 0.2% glycerol, 1 mM $MgSO_4$, 1 µg/mL thiamine, 0.5% case amino acids, 0.4% lactose and 1 mM isopropyl β-D-1-thiogalactopyranoside (IPTG). Strains MT184 and MT211 (Table A.4) were created by amplification of hCDA or yCD with the primers listed in Table A.1. The PCR products were then transformed into MT180 containing pKD20 and subjected to the selection conditions listed above. Correct clones were verified by using the *lacZ* locus primers listed in Table A.3.

A.2.4 CD Activity Selection

The selection for CD activity was performed in M9 minimal media agar plates supplemented with 0.2% maltose, 1 mM $MgSO_4$, 1 µg/mL thiamine, 20 µg/mL cytosine, 0.1 µg/mL biotin, 10 µg/mL nicotinic acid, and 0.1 mM IPTG. Selections were also performed in the same M9 liquid media recipe lacking agar and supplemented with 200 ng/mL uracil. The counter screen for enzymatic activity on 5-FC was performed in the same M9 agar media used for the selection except that cytosine was replaced with 10 µg/mL uracil to make it non-selective and 10 µg/mL of 5-FC was added. Selections and screens were performed at 30 °C.

For the randomization, MT238 was grown overnight in LB media at 30 °C. The culture was diluted 100-fold into fresh LB media and grown at 30 °C until OD_{600} of 0.6 was reached. The culture was then induced for recombination functions at 42 °C for 15 minutes in a water bath. The culture was collected by centrifugation at 10,000 xg at 4 °C and resuspended in half the original culture volume with 10% glycerol at 4 °C. The centrifugation and wash steps were repeated twice more and finally the cells were resuspended in 1/10th the original culture volume with 10% glycerol at 4 °C. 50 µL of cells were transformed with 1 pmole of randomization oligo (5'-
GCTCACCCAGGAGGGGAGAATCTTCAAAGGGTGCAACATAGAAAATNNKNNKNNK
NNKNNKNNKCTGGGCATCTGTGCTGAACGGACCGCTATCCAGAAG, where n is any nucleotide and k is either g or t). The cells were incubated with shaking at 30 °C in SOC media for 1 hour. At this point the cells were either collected by centrifugation at 10,000 xg, re-suspended in M9 liquid selective media and subjected to selection or were grown overnight in LB media to repeat the transformation step the following day.

A.2.5 PCR Genotyping of the Selection Strain

A method to determine the extent of randomization of the target sequence was developed using PCR. Four separate primers: 5'-GGTGCAACATAGAAAATG, 5'-GGTGCAACATAGAAAATA, 5'-GGTGCAACATAGAAAATT, and 5'-GGTGCAACATAGAAAATC were used with *lacZ* locus reverse primer (Table A.3) to determine the sequence of first nucleotide in the target sequence. A single mismatch at the 3' end of the forward primer is sufficient inhibit PCR product formation, otherwise a 488 bp product is produced. For colony PCR, a single colony was placed into 10 µL of water and then heated at 95 °C for 10 minutes. For PCR from a culture, 100 µL of a saturated culture grown in LB media was pelleted by centrifugation at 10,000 xg and resuspended in an equal volume of water and then heated at 95 °C for 10 minutes. 10 µL of the *E. coli* lysates were combined with *Taq* DNA polymerase from New England Biolabs (Ipswich, MA) in ThermoPol buffer following the manufacturers protocol. The conditions for PCR were an initial denaturation for 2 minutes at 95 °C, followed by 25 cycles of 95 °C for 30 seconds, 55 °C for 30 seconds, and 72 °C for 30 seconds.

Allele	**Forward (5' to 3')**	**Reverse (5' to 3')**
hsdR::cm	GTGGTCATTGCCCGGAAAG GTACAGAAAGCTAAGATGA GGTGTAGGCTGGAGCTGCTT C	CCAACGCAGAGGCAGCCTGAA GGATGAAGTGTATACGTGATG GGAATTAGCCATGGTCC
lacZ::hCDA	TATGTTGTGTGGAATTGTGA GCGGATAACAATTTCACACA GGAAACAGCTATGGGCAGC AGCCATCATCA	ATGGATTTCCTTACGCGAAAT ACGGGCAGACATGGCCTGCCC GGTTATTATCACTGGGTCTTCT GCAGGT
lacZ::yCD	TATGTTGTGTGGAATTGTGA GCGGATAACAATTTCACACA GGAAACAGCTATGGGCAGC AGCCATCATCA	ATGGATTTCCTTACGCGAAAT ACGGGCAGACATGGCCTGCCC GGTTATTATTATTCACCGATGT CTTC

Table A.1 Primers used for allele knockouts.

Allele	CGSC Number
galE::kan	8297
codA::kan	8524
pyrF::kan	9145
uraA::kan	9981
mutS::kan	10126

Table A.2 Alleles obtained from the Coli Genetic Stock Center (CGSC).

Locus	Forward	Reverse
hsdR	CTTCCGGTTTTGTTGCCAGA	TCAGGCCAGCTCGTCCCA
lacZ	ACCGCCTCTCCCCGCGCG	CCCGTATCACTTTTGCTG
codA	TGAGCACTTTGCGACCACGC	GAAGGCATTTTTGCACATGG

Table A.3 Primers used for confirmation of locus disruption.

Strain Designation	Genotype
MT125	MG1655 *codA*::kan
MT178	BW25113 *galE*
MT180	BW25113 *galE codA*::kan *lacZ*$^{+}$
MT184	BW25113 *galE codA*::kan *lacZ*::hCDA
MT211	BW25113 *galE codA*::kan *lacZ*::yCD
MT147	BW25113 *hsdR*::cm
MT149	MG1655 *hsdR*::cm
MT153	MG1655 *hsdR*
MT160	MG1655 *hsdR pyrF*::kan
MT161	MG1655 hsdR pyrF
MT162	MG1655 *hsdR pyrF uraA*::kan
MT163	MG1655 hsdR pyrF uraA
MT216	MG1655 hsdR pyrF uraA mutS::kan
MT221	MG1655 hsdR pyrF uraA mutS
MT234	MG1655 *hsdR pyrF uraA mutS nadA*::Tn10 λcI857 Δ(*cro-bioA*)
MT238	MG1655 *hsdR pyrF uraA mutS codA*::kan lacZ::hCDA *nadA*::Tn10 λcI857 Δ(*cro-bioA*)
MT245	MG1655 *hsdR pyrF uraA codA*::kan *lacZ*::hCDA *nadA*::Tn10 λcI857 Δ(*cro-bioA*)
MT246	MG1655 *hsdR pyrF uraA codA*::kan *lacZ*::yCD *nadA*::Tn10 λcI857 Δ(*cro-bioA*)
MT249	MG1655 *hsdR pyrF uraA codA*::kan *nadA*::Tn10 λcI857 Δ(*cro-bioA*)
MT283	MG1655 *hsdR pyrF uraA codA*::kan *lacZ*::hCDA (I_{78}SNLYY)

Table A.4 Strains constructed in this study.

A.3 Results

A.3.1 Characterization of the Selection Strain

Previous studies have utilized the *E. coli* strain GIA39 (*thr*¯ *dadB*3 *leuB*6 *fhuA*21 *codA*1 *lacY*1 *tsx*-95 *glnV*44(AS) λ¯ *pyrF*101 *his*-108 *argG*6 *ilvA*634 *thi*-1 *deoC*1 *glt*-15), which in our hands did not provide for a robust selection as it grew well in the selective conditions previously used (Fuchita et al., 2009; Mahan et al., 2004; Stolworthy et al., 2008). GIA39 contains 15 mutations, only two of which (*codA* and *pyrF*) are required for selection, and it is able to grow in the presence of minimal amounts of uracil because it is wildtype for the uracil transporter, *uraA*. This necessitates the use of a poorly defined yeast synthetic dropout additive lacking uracil. The result is a strain that has a minor growth defect that is alleviated when complemented with CD activity.

We re-engineered a selection strain that was much more stringent and placed hCDA on the chromosome where it could be mutagenized by recombineering. Figure A.3 shows the roadmap of strain construction on the *E. coli* chromosome. In the selective media only the strain harboring yCD was able to grow (Figure A.4A). In addition, when grown in the presence of 5-FC the strain containing yCD was unable to grow unlike the strain containing hCDA or wiltype *lacZ* (Figure A.4B). This strain and the conditions developed allowed for a very robust selection for live versus dead cells. In fact, the selection conditions were so robust that uracil was added back to the liquid selection conditions to allow for weak hCD activity to be detected, if present (Figure A.5). The optimal concentration for weak complementation of the growth defect was found to be 0.2 μg/mL uracil and was used during the selection. Interestingly, despite the *uraA,* uracil transporter mutation, uracil was still able to complement the growth defect. The reason for this is not understood, but it could be because of passive diffusion of uracil or another compensating

transporter mediating uptake.

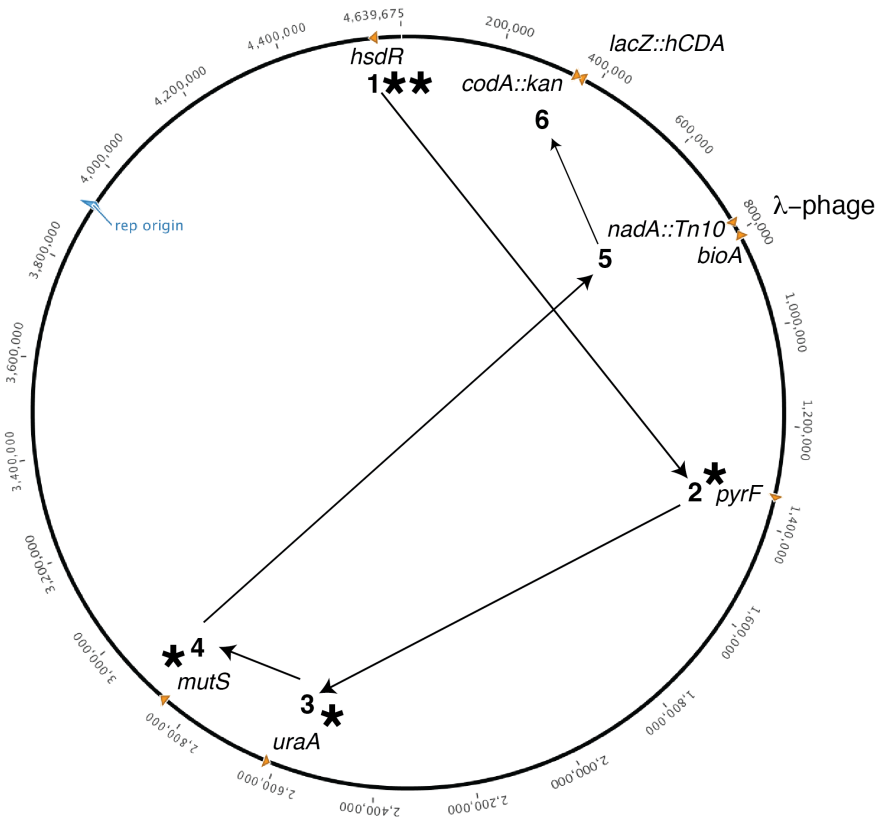

Figure A.3 Strain construction road map.
The mutations that were introduced into the strain are indicated on the chromosome starting with *hsdR* (1) and ending with *codA::kan* linked to *lacZ::hCDA* (6). * represents markers that had kanamycin resistance removed, and ** represents removal of chloramphenicol resistance marker.

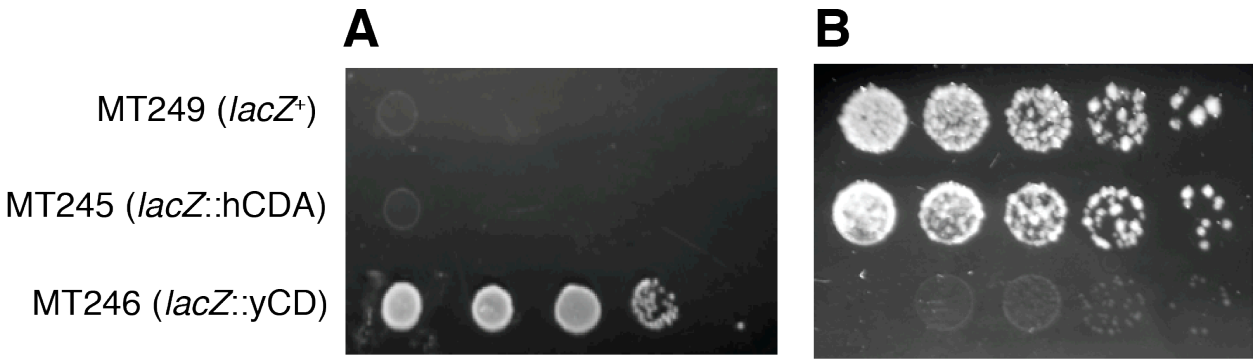

Figure A.4. Selection conditions.
10-fold serial dilutions of an overnight culture of the strains indicated on the left were spotted on selective media (A) or non-selective media supplemented with 5-FC (B).

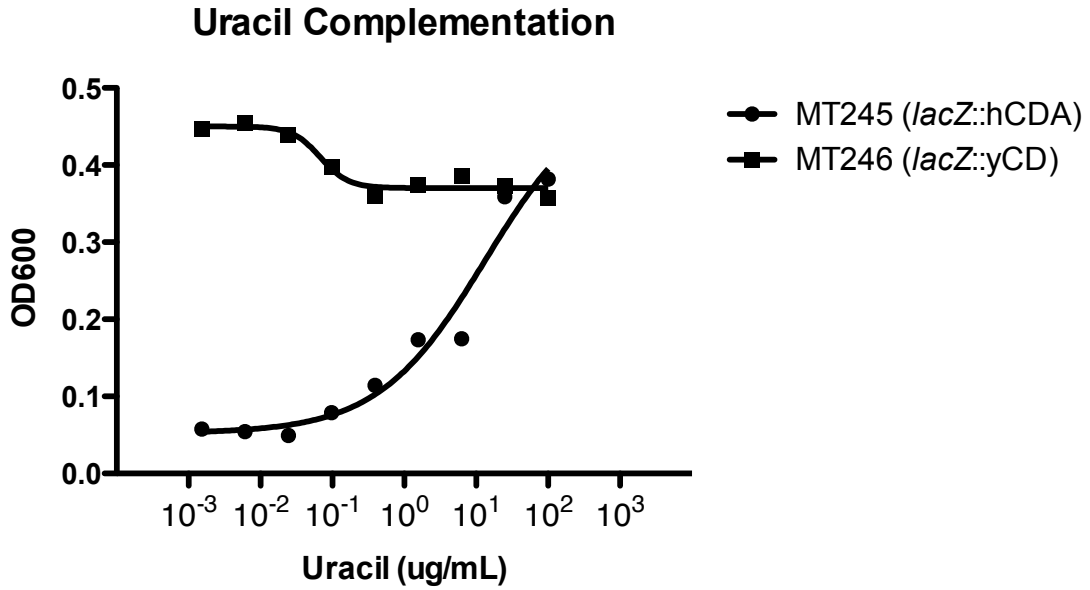

Figure A.5. Uracil complementation of liquid selection conditions.
Strains MT245 and MT246 were grown in M9 liquid selection media supplemented with 1 ng/mL to 10 µg/mL uracil. 200 ng/mL was chosen as the minimum concentration to alleviate the stringent selective pressure.

A.3.2 Target Randomization and Selection

A method to determine how well the target site within the chromosomal hCDA was mutated was developed. Using four different oligonucleotide primers that differed in the 3' nucleotide, the 5' nucleotide (N1) of the target site could be genotyped. This served as proxy for the mutations that were occurring 3' to that site. Strain MT238 contains the wildtype hCDA integrated at *lacZ*, which has a guanine at the N1 position, while strain MT283 contains a mutated hCDA at the target site that encodes for an adenine at the N1 position. As shown in Figure A.6A, strains MT238 and MT283 were correctly sequenced at the N1 position. It is noteworthy to mention that despite using identical conditions for genotyping the N1 position there is a significant difference between the intensity of the resulting PCR band. This is most likely due to the lower annealing temperature for the primers containing either adenine or thymine at the N1 position. Thus this method cannot be used to quantify the total diversity rather it is a binary measure of whether the

N1 position is mutated.

Using the PCR based genotyping method, MT238 was successively transformed with the randomizing oligo to create a population of cells that had been randomized at the target site within hCDA. Figure A.6B shows the PCR sequencing of the N1 position following five successive rounds of electroporating the randomization oligo into strain MT238. By the fifth round of transformation a positive PCR product was obtained using all four sequencing primers indicating that the target site had been heavily modified. A PCR product using the *lacZ* primers in Table A.3 was made from this population of randomized cells and sent for sequencing. Figure A.6C shows the results of the sequencing and indicates that the target site was mutated to the NNK_6 sequence expected. Using this batch of randomized cells, they were subjected to the liquid selection conditions by growing at 30 °C for two days until visible turbidity in the media was observed. At this point the selected population of cells was again PCR sequenced and displayed a different genotype lacking detectable levels of thymine at the N1 position (Figure A.6D). These data suggest that the selection conditions altered the genotype of the randomized population.

The cells were then plated on selective agar media to isolate clones. Individual clones were then selected and grown up in selective media to determine the ability of clonal isolates to grow under selection. A total of 12 clones were selected for sequence analysis, by PCR amplification of the *lacZ*::hCDA locus. The results of the sequence analysis showed either wildtype hCDA or a Q92L mutation. The Q92L mutation is located at the 3' junction of where the randomizing oligo hybridizes and not within the target randomization site. These data suggest that an alternative suppresser mutation arose in the population or the cultures became contaminated. Contamination was deemed unlikely as a similar suppresser mutation was uncovered in a previous strain of

MT238 that was wildtype for *mutS* (MT245). In this selection, a clone was isolated with a mutation in the target site A_{78}CYP to I_{78}SNLYY. Unfortunately, when this mutation was backcrossed into MT163 to generate MT283 the ability to grow in selective media was lost, strongly suggesting a suppresser mutation arose at another genomic locus unlinked to *codA*::kan.

A P1 lysate was created on the pool of selected cells and backcrossed into MT163 and subjected to the hCD activity selection conditions in the presence of kanamycin to uncover hCD activity linked to *codA*::kan, but no colonies were obtained. These data further support that a high level of suppresser mutations were obtained in the selection using MT238 that completely masked our ability to detect hCD activity.

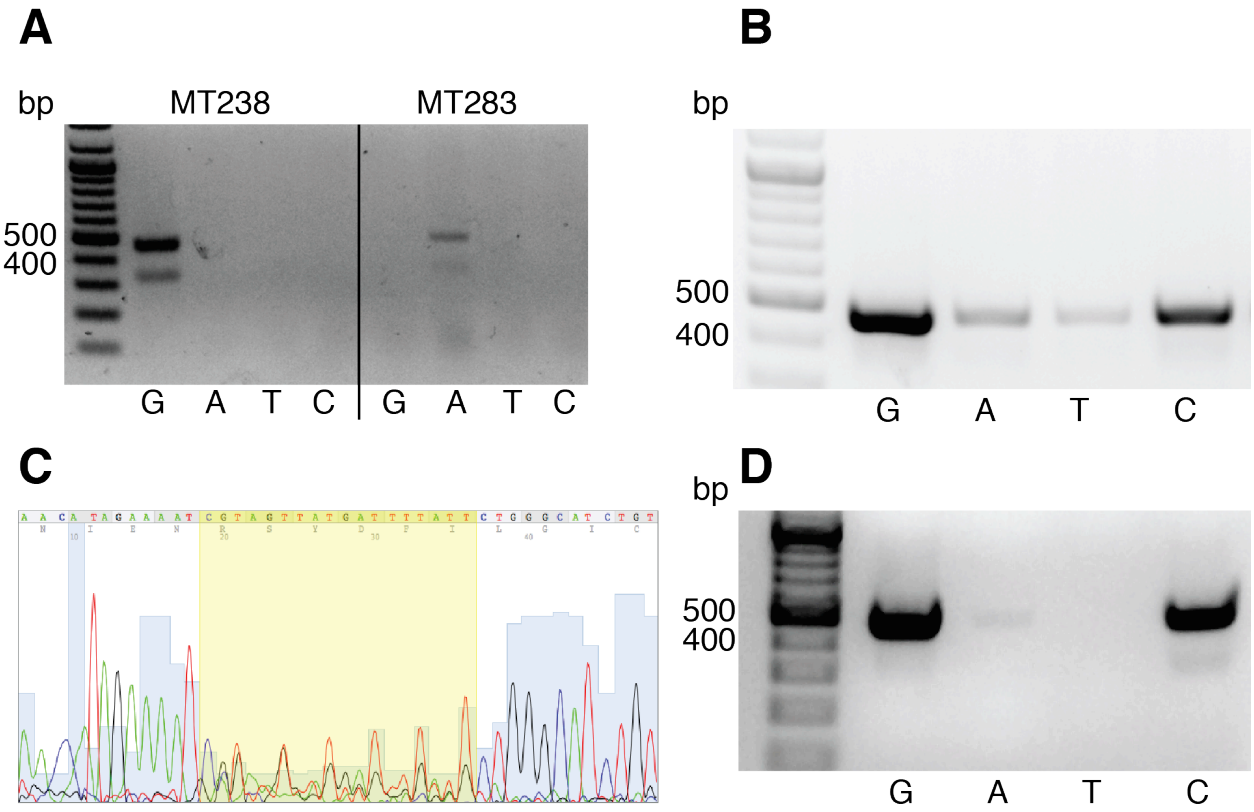

Figure A.6 Determination of target sequence randomization.
A) PCR based genotyping of the 5' nucleotide of the hCDA randomization target site (N1). Strain MT238 contains the wildtype hCDA that codes for a guanine at N1, while strain MT283 contains a mutant hCDA that codes for an adenine at N1. B) Following five rounds of transforming the randomizing oligo into strain MT238, all 4 nucleotides at the N1 position were observed in the strain suggesting saturating randomization. C) A PCR product of the *lacZ* locus in the randomized MT238 population was sent for sequence analysis. The target site highlighted in yellow was randomized to the expected NNK_6 sequence. D) Following selection of the randomized MT238 population for hCD activity the N1 position was again sequenced and found to have an altered mixture of genotype than the unselected population in 3B.

Clone	OD600	Ratio to MT238	Mutation
MT238	0.0297	1	Wildtype
E7	0.0407	1.4	ND
E6	0.0512	1.7	Q92L
E9	0.0722	2.4	Q92L
E8	0.0733	2.5	ND
C9	0.0796	2.7	Q92L
A9	0.101	3.4	Q92L
E10	0.109	3.7	Q92L
A10	0.1101	3.7	Wildtype
G7	0.1105	3.7	Q92L
A3	0.1134	3.8	Wildtype
A8	0.1252	4.2	Wildtype
A11	0.151	5.1	Q92L

Table A.5 Growth of clonal isolates in selective media.
Following clonal selection for hCD activity, the hCDA at the *lacZ* locus was amplified and sent for sequence analysis. The clones contained either a wildtype sequence or a Q92L mutation at the 3' randomizing oligo homology site, but no mutations in the target randomization site.

A.4 Conclusion

The apparent high rate of suppresser mutations that arose during the selection abrogated any selection for true hCD activity. The *mutS* mutation causes a mutator phenotype (Kunkel and Erie, 2005), which likely lead to the high rate of suppresser mutations uncovered using strain MT238. The *mutS* mutation was added because its allows for high levels of lambda red mediated recombination (Costantino and Court, 2003), and in a prior selection with strain MT245, complete mutagenesis of the target randomization site at N1 was not observed.

In the selection using strain MT245, a mutant hCDA with a target site randomization was selected, but it failed to have hCD activity when backcrossed suggesting that the mutation that was selected for was a suppresser. The high level of suppresser mutations in either MT245 or MT238 limited the ability to find true hCD activity. While it is possible that hCD activity could

have been uncovered, extensive work to identify the suppressor loci and subsequent engineering to limit its generation would have been required. In addition to the selection performed in these studies, a separate plasmid based selection system was also developed and screened without any hCD activity. It is also possible that the alteration of nucleotide pools inherent in the selection strain developed causes a mutator phenotype as well (Nordman, 2008).

The complex quaternary structure of hCDA, combined with the lack of positive results using two distinct randomization and selection approaches ultimately made us abandon this project. An alternative enzyme, adenosine deaminase, was discussed as a potential substrate for mutagenesis but was not pursued. In addition, since yCD and bCD had already been subjected to enzymatic enhancement efforts these targets were not pursued either (Fuchita et al., 2009; Mahan et al., 2004; Stolworthy et al., 2008). Nevertheless, a powerful selection system was developed along with a mutagenesis technique that allowed a library of $>10^7$ proteins to be screened for activity. While the strains developed here are specific to the selection of cytosine deaminse activity, the lambda red mutagenesis technique employed can be applied to many other types of large protein screens. It is possible that in another type of selection or screen that the technique could result in high probabilities of success.

A.5 References

Baba, T., Ara, T., Hasegawa, M., Takai, Y., Okumura, Y., Baba, M., Datsenko, K.A., Tomita, M., Wanner, B.L., and Mori, H. (2006). Construction of Escherichia coli K-12 in-frame, single-gene knockout mutants: the Keio collection. Mol Syst Biol *2*, 2006.0008.

Chung, S.J., Fromme, J.C., and Verdine, G.L. (2005). Structure of human cytidine deaminase bound to a potent inhibitor. J Med Chem *48*, 658–660.

Costantino, N., and Court, D.L. (2003). Enhanced levels of lambda Red-mediated recombinants in mismatch repair mutants. Proc Natl Acad Sci USA *100*, 15748–15753.

Costanzi, S., Vincenzetti, S., Cristalli, G., and Vita, A. (2006). Human cytidine deaminase: a three-dimensional homology model of a tetrameric metallo-enzyme inferred from the crystal structure of a distantly related dimeric homologue. J. Mol. Graph. Model. *25*, 10–16.

Cunningham, C., and Nemunaitis, J. (2001). A phase I trial of genetically modified Salmonella typhimurium expressing cytosine deaminase (TAPET-CD, VNP20029) administered by intratumoral injection in combination with 5-fluorocytosine for patients with advanced or metastatic cancer. Protocol no: CL-017. Version: April 9, 2001. Human Gene Therapy *12*, 1594–1596.

Datsenko, K.A., and Wanner, B.L. (2000). One-step inactivation of chromosomal genes in Escherichia coli K-12 using PCR products. Proc Natl Acad Sci USA *97*, 6640–6645.

Diner, E.J., and Hayes, C.S. (2009). Recombineering reveals a diverse collection of ribosomal proteins L4 and L22 that confer resistance to macrolide antibiotics. J Mol Biol *386*, 300–315.

Ellis, H.M., Yu, D., DiTizio, T., and Court, D.L. (2001). High efficiency mutagenesis, repair, and engineering of chromosomal DNA using single-stranded oligonucleotides. Proc Natl Acad Sci USA *98*, 6742–6746.

Erbs, P., Regulier, E., Kintz, J., Leroy, P., Poitevin, Y., Exinger, F., Jund, R., and Mehtali, M. (2000). In vivo cancer gene therapy by adenovirus-mediated transfer of a bifunctional yeast cytosine deaminase/uracil phosphoribosyltransferase fusion gene. Cancer Res *60*, 3813–3822.

Fuchita, M., Ardiani, A., Zhao, L., Serve, K., Stoddard, B.L., and Black, M.E. (2009). Bacterial cytosine deaminase mutants created by molecular engineering show improved 5-fluorocytosine-mediated cell killing in vitro and in vivo. Cancer Res *69*, 4791–4799.

Gagandeep, S., Brew, R., Green, B., Christmas, S.E., Klatzmann, D., Poston, G.J., and Kinsella, A.R. (1996). Prodrug-activated gene therapy: involvement of an immunological component in the "bystander effect". Cancer Gene Ther *3*, 83–88.

Gossen, J.A., Molijn, A.C., Douglas, G.R., and Vijg, J. (1992). Application of galactose-sensitive E. coli strains as selective hosts for LacZ- plasmids. Nuc Acid Res *20*, 3254.

Ireton, G.C.G., McDermott, G.G., Black, M.E.M., and Stoddard, B.L.B. (2002). The structure of Escherichia coli cytosine deaminase. J Mol Biol *315*, 11–11.

Ireton, G.C., Black, M.E., and Stoddard, B.L. (2003). The 1.14 A crystal structure of yeast cytosine deaminase: evolution of nucleotide salvage enzymes and implications for genetic chemotherapy. Structure *11*, 961–972.

Johansson, E., Mejlhede, N., Neuhard, J., and Larsen, S. (2002). Crystal structure of the tetrameric cytidine deaminase from Bacillus subtilis at 2.0 A resolution. Biochemistry *41*, 2563–2570.

Kievit, E., Bershad, E., Ng, E., Sethna, P., Dev, I., Lawrence, T.S., and Rehemtulla, A. (1999). Superiority of yeast over bacterial cytosine deaminase for enzyme/prodrug gene therapy in colon cancer xenografts. Cancer Res *59*, 1417–1421.

Kunkel, T.A., and Erie, D.A. (2005). DNA mismatch repair. Annu. Rev. Biochem. *74*, 681–710.

Mahan, S.D., Ireton, G.C., Knoeber, C., Stoddard, B.L., and Black, M.E. (2004). Random mutagenesis and selection of Escherichia coli cytosine deaminase for cancer gene therapy. Protein Eng Des Sel *17*, 625–633.

Mientjes, E., van Delft, J.H., op't Hof, B., and Gossen, J.A. (1994). An improved selection method for λlacZ− phages based on galactose sensitivity. Transgenic Research.

Nordman, J., and Wright, A. (2008). The relationship between dNTP pool levels and mutagenesis in an Escherichia coli NDP kinase mutant. Proc Natl Acad Sci USA *105*, 10197–10202.

Ohwada, A., Hirschowitz, E.A., and Crystal, R.G. (1996). Regional delivery of an adenovirus vector containing the Escherichia coli cytosine deaminase gene to provide local activation of 5-fluorocytosine to suppress the growth of colon carcinoma metastatic to liver. Human Gene Therapy *7*, 1567–1576.

Park, J.I., Cao, L., Platt, V.M., Huang, Z., Stull, R.A., Dy, E.E., Sperinde, J.J., Yokoyama, J.S., and Szoka, F.C., Jr (2009). Antitumor therapy mediated by 5-fluorocytosine and a recombinant fusion protein containing TSG-6 hyaluronan binding domain and yeast cytosine deaminase. Mol Pharm *6*, 801–812.

Stolworthy, T.S.T., Korkegian, A.M.A., Willmon, C.L.C., Ardiani, A.A., Cundiff, J.J., Stoddard, B.L.B., and Black, M.E.M. (2008). Yeast cytosine deaminase mutants with increased thermostability impart sensitivity to 5-fluorocytosine. J Mol Biol *377*, 854–869.

Valledor, M., Hu, Q., Schiller, P., and Myers, R.S. (2012). Fluorescent protein engineering by in vivo site-directed mutagenesis. IUBMB Life *64*, 684–689.

Yao, L., Li, Y., Wu, Y., Liu, A., and Yan, H. (2005). Product release is rate-limiting in the activation of the prodrug 5-fluorocytosine by yeast cytosine deaminase. Biochemistry *44*, 5940–5947.

Yu, D., Ellis, H.M., Lee, E.C., Jenkins, N.A., Copeland, N.G., and Court, D.L. (2000). An efficient recombination system for chromosome engineering in Escherichia coli. Proc Natl Acad Sci USA *97*, 5978–5983.

Zhang, M.M., Li, S.S., Nyati, M.K.M., DeRemer, S.S., Parsels, J.J., Rehemtulla, A.A., Ensminger, W.D.W., and Lawrence, T.S.T. (2003). Regional delivery and selective expression of a high-activity yeast cytosine deaminase in an intrahepatic colon cancer model. Cancer Res *63*, 658–663.

Publishing Agreement

It is the policy of the University to encourage the distribution of all theses, dissertations, and manuscripts. Copies of all UCSF theses, dissertations, and manuscripts will be routed to the library via the Graduate Division. The library will make all theses, dissertations, and manuscripts accessible to the public and will preserve these to the best of their abilities, in perpetuity.

Please sign the following statement:

I hereby grant permission to the Graduate Division of the University of California, San Francisco to release copies of my thesis, dissertation, or manuscript to the Campus Library to provide access and preservation, in whole or in part, in perpetuity.

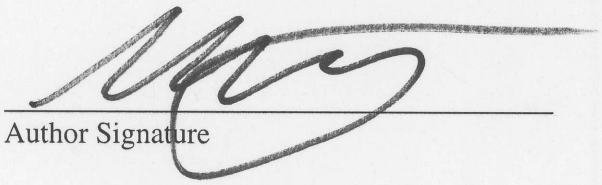

Author Signature

10/18/2013

Date